

**Journal of  
Mechanics of  
Materials and Structures**

**Volume 9, No. 3**

**May 2014**



# JOURNAL OF MECHANICS OF MATERIALS AND STRUCTURES

[msp.org/jomms](http://msp.org/jomms)

Founded by Charles R. Steele and Marie-Louise Steele

## EDITORIAL BOARD

ADAIR R. AGUIAR	University of São Paulo at São Carlos, Brazil
KATIA BERTOLDI	Harvard University, USA
DAVIDE BIGONI	University of Trento, Italy
IWONA JASIUK	University of Illinois at Urbana-Champaign, USA
THOMAS J. PENCE	Michigan State University, USA
YASUhide SHINDO	Tohoku University, Japan
DAVID STEIGMANN	University of California at Berkeley

## ADVISORY BOARD

J. P. CARTER	University of Sydney, Australia
D. H. HODGES	Georgia Institute of Technology, USA
J. HUTCHINSON	Harvard University, USA
D. PAMPLONA	Universidade Católica do Rio de Janeiro, Brazil
M. B. RUBIN	Technion, Haifa, Israel

**PRODUCTION** [production@msp.org](mailto:production@msp.org)

SILVIO LEVY Scientific Editor

---

See [msp.org/jomms](http://msp.org/jomms) for submission guidelines.


---

JoMMS (ISSN 1559-3959) at Mathematical Sciences Publishers, 798 Evans Hall #6840, c/o University of California, Berkeley, CA 94720-3840, is published in 10 issues a year. The subscription price for 2014 is US \$555/year for the electronic version, and \$710/year (+\$60, if shipping outside the US) for print and electronic. Subscriptions, requests for back issues, and changes of address should be sent to MSP.

---

JoMMS peer-review and production is managed by EditFLOW<sup>®</sup> from Mathematical Sciences Publishers.

PUBLISHED BY

 **mathematical sciences publishers**  
nonprofit scientific publishing  
<http://msp.org/>

© 2014 Mathematical Sciences Publishers

# B-SPLINES COLLOCATION EIGENANALYSIS OF 2D ACOUSTIC PROBLEMS

CHRISTOPHER G. PROVATIDIS

We continue our research on the performance of CAD-based global approximation to the analysis of 2D acoustic problems. In addition to previous “boundary-only” Coons and transfinite Gordon–Coons interpolations, we now investigate the quality of the solution when utilizing “tensor product B-splines” interpolation. For the latter, we propose a global collocation method that is successfully compared with the well known Galerkin–Ritz formulation. Particular attention is paid to the handling of Neumann boundary conditions as well as to the role of multiplicity of internal knots. The theory is supported by two numerical examples, one for a rectangular and the other for a circular acoustic cavity in which the approximate solution rapidly converges towards the exact solution.

## 1. Introduction

The tendency in contemporary computer methods in applied mechanics and engineering is to integrate solid modeling (computer-aided-design or CAD) with analysis (computer-aided-engineering or CAE) using NURBS interpolation, in such a way that both the geometry and the mechanical variables (displacement, temperature, etc.) are mathematically expressed in a similar manner (global approximation) [Cottrell et al. 2009]. In fact, though the nonuniform B-splines (NURBS) of today is, chronologically speaking, the fifth important formulation applied to the mathematical description of CAD models, the same integration can be achieved with using any of the previous formulations. The first bivariate formula was proposed in 1964–1967 by Coons [1967], the second by Gordon [1971] and the third in 1966–1971 by Bézier [1971]. Furthermore, B-splines are chronologically the fourth formula in CAD practice. Although older mathematical formulations of splines were first published by Schoenberg [1946], they became very popular only after 1972 when de Boor [1972] proposed his computationally efficient algorithms. Finally, B-splines were later modified on the basis of weighting coefficients, thus producing the popular NURBS of today, which are fully controlled sculptured surfaces [Piegl 1991; Piegl and Tiller 1995]. For a detailed review we refer to [Farin et al. 2002].

Concerning mechanical analysis in problems of solids and structures including acoustics, it is well known that there are three main methodologies: the popular finite element method (FEM), the boundary element method (BEM), and the promising global collocation method ([Provatidis 2008b; 2009b; Provatidis and Ioannou 2010] and about 300 references therein). For the sake of brevity, finite volume, finite difference, mesh-less and mesh-free methodologies are not commented on. So far, FEM [Höllig 2003] and BEM [Cabral et al. 1990; 1991] have been applied in conjunction with tensor product B-splines in several engineering problems. Also, Coons–Gordon transfinite interpolation has been extensively used in conjunction with the Galerkin–Ritz formulation; for an overview we refer to [Provatidis 2012] and

---

*Keywords:* B-splines, Galerkin–Ritz, global collocation, eigenvalues, CAD/CAE.



literature therein. Our conclusion in that article is that rapid CAD-based global collocation methods have to be applied instead of time-consuming domain Galerkin–Ritz methods.

For the first time, in 2005 the author expressed the above general idea of implementing a *global collocation* scheme in conjunction with CAD-based approximation [Provatis 2006, p. 6704], while he continued with numerical applications in potential problems under Dirichlet [Provatis 2008b] and Neumann [Provatis 2009b] boundary conditions, as well as in plane stress elastostatics [Provatis and Ioannou 2010]. Concerning eigenvalue and time response structural analysis, in 2008 he published a couple of papers [Provatis 2008a; 2008c] (1D problems), and also he supervised a thesis concerning 2D acoustics and 2D elastodynamics in conjunction with Lagrange polynomials [Filippatos 2010]. It is worth mentioning that isogeometric collocation methods were recently presented by others [Auricchio et al. 2010].

It is well known that B-splines collocation methods were initially developed by mathematicians, well before engineers understood that CAD-based Galerkin–Ritz methods require high computing effort, a fact that motivated them to investigate their replacement by isogeometric collocation schemes [Hughes et al. 2010]. For a detailed review of 273 papers covering the period 1934–1989 we refer to [Fairweather and Meade 1989], whereas recent works are cited in a survey [Bialecki et al. 2011]. A fair comparison between B-spline collocation and Galerkin methods on the basis of the same bandwidth (and not the same degree of shape functions) in one spatial dimension is [Kwok et al. 2001]. However, most works are limited to one-dimensional problems [de Boor 2001, Chapter XV], where, for cubic B-splines, the key point is to use two collocation points between any two breakpoints, thus resulting in as many equations as the number of unknowns; this is strictly related to using double knots (de Boor, personal communication, 2007). On the other hand, excellent results have been obtained in some particular examples using for collocation the images of either Greville or Demko abscissae [Auricchio et al. 2010].

It is remarkable that de Boor’s software, aiming at the solution of one-dimensional (1D) elliptic nonlinear problems, although incorporated in Matlab (Spline Toolkit) long ago, is not still applicable to the solution of eigenvalue and time-marching problems “as is”. As confirmed by the absence of relevant publications, the need of a computational environment to solve 2D and 3D problems is of great engineering interest.

Within this context, this paper reports on the performance of the B-splines-based global collocation method for the eigenvalue analysis of two-dimensional acoustic cavities under arbitrary, Dirichlet or Neumann boundary conditions. Particular attention is paid to the treatment of the free-free problem in order to bypass the singularities that sometimes may appear at the four corner points of the reference square. Moreover, the role of the multiplicity of internal knots is thoroughly investigated, and particularly the performance of the proposed least-squares scheme in conjunction with single knots is studied. The theory is sustained by two numerical examples, one for a rectangular and the other for a circular acoustic cavity, in which the proposed collocation method is successfully compared with its competitive Galerkin–Ritz scheme, using either tensor product B-splines or/and conventional finite elements, for the same mesh density.

## 2. B-splines as a global 2D functional set

**2.1. General.** Let us consider a rectangular domain  $\Omega = (ABCD) = [0, a] \times [0, b]$  in  $\mathbb{R}^2$ . The axis origin is chosen at the corner  $A$ , whereas the Cartesian axes  $x$  and  $y$  lie on the sides  $AB$  and  $AD$ , respectively.

Sides  $AB$  and  $CD$  are uniformly divided into  $n_x$  segments, while  $BC$  and  $DA$  are uniformly divided into  $n_y$  segments. This leads to  $n_x + 1$  breakpoints along  $AB$  and  $CD$ , and  $n_y + 1$  breakpoints along  $BC$  and  $DA$ . Although it is possible to use different degrees for the spline polynomials in the  $x$ - and  $y$ -directions, we will use a single degree  $p_x = p_y = p$ , with  $p \geq 3$ , since we are dealing with a second order PDE (acoustics). As a result, the univariate function  $u(x, 0)$  along the side  $AB$  can be interpolated via a piecewise polynomial B-spline of  $p$ -th degree in  $x$ , and the function  $u(0, y)$  along the side  $DA$  via a piecewise polynomial B-spline of  $p$ -th degree in  $y$ .

**2.2. One-dimensional shape functions.** This section refers to either the  $x$ - or  $y$ -directions (along the sides  $AB$  and  $DA$ , respectively). Below,  $n$  corresponds to either subdivision  $n_x$  or  $n_y$ , whereas the domain  $[0, L]$  corresponds to either of the intervals  $[0, a]$  or  $[0, b]$ .

Let us assume a given number of  $n$  subdivisions of the interval  $[0, L]$ , with breakpoints  $x_0, \dots, x_n$ , and a given polynomial degree  $p$ . In its original form [Schoenberg 1946; Schoenberg and Whitney 1953], the B-splines formula includes a complete polynomial of  $p$ -th degree for the entire domain  $[0, a]$ , plus  $(n - 1)$  truncated monomials  $\langle x - x_i \rangle_+^p$ ,  $i = 1, \dots, n$ . In this way, the total number of coefficients becomes  $(n + p)$ , and we refer to a multiplicity of internal knots equal to one, which ensures  $C^{p-1}$ -continuity. Therefore, in the particular case of a cubic approximation ( $p = 3$ ), the total number of coefficients becomes  $(n + 3)$ , which ensures  $C^2$ -continuity.

In contrast, if we alternatively consider the above complete polynomial of  $p$ -th degree for the entire domain  $[0, L]$  plus the aforementioned  $(n - 1)$  truncated monomials  $\langle x - x_i \rangle_+^p$ , and additionally  $(n - 1)$  truncated monomials  $\langle x - x_i \rangle_+^{p-1}$ ,  $i = 1, \dots, n$ , the total number of coefficients becomes  $(2n + p - 1)$ , and then we refer to internal multiplicity equal to two, which ensures  $C^{p-2}$ -continuity; for example,  $C^1$ -continuity and  $2(n + 1)$  coefficients, when  $p = 3$ .

In the modern approach [Piegl and Tiller 1995; de Boor 2001], these coefficients are associated with what's called *control points*. In more detail, we start with the above-mentioned breakpoints

$$\{\mathbf{x}_b\} = [x_0, \dots, x_n], \tag{1}$$

and then we introduce the *knot vector*  $\{\mathbf{V}\}$ ,

$$\{\mathbf{V}\} = [v_0, \dots, v_m], \tag{2}$$

which highly depends on the chosen *multiplicity*  $\lambda$  of internal knots (usually single or double):

- multiplicity  $\lambda = 1$ :  $\{\mathbf{V}\}_{\lambda=1} = [\underbrace{x_0, \dots, x_0}_{p+1}, x_1, x_2, \dots, x_{n-1}, \underbrace{x_n, \dots, x_n}_{p+1}]$ , (3)

- multiplicity  $\lambda = 2$ :  $\{\mathbf{V}\}_{\lambda=2} = [\underbrace{x_0, \dots, x_0}_{p+1}, \underbrace{x_1, x_1}_2, \underbrace{x_2, x_2}_2, \dots, \underbrace{x_{n-1}, x_{n-1}}_2, \underbrace{x_n, \dots, x_n}_{p+1}]$ . (4)

Therefore, Equations (3) and (4) lead to the unified relationship

$$m = 2(p + 1) + \lambda(n - 1) - 1, \quad \lambda = 1, 2. \tag{5}$$

Based on the above-mentioned computed knot vector  $\{\mathbf{V}\}$ , the vector of control points is denoted by

$$\{\mathbf{P}\} = [\mathbf{P}_0, \dots, \mathbf{P}_{n_c}], \tag{6}$$

where the number of control points ( $n_c + 1$ ) is related to the number of elements in the knot vector ( $m + 1$ ) as

$$m = n_c + p + 1. \tag{7}$$

Then, for every position  $x \in [0, L]$ , with normalized coordinate  $\xi = x/L \in [0, 1]$ , we can determine the values of  $n_c + 1$  basis functions,  $N_{i,p}(x)$  or  $N_{i,p}(\xi)$ ,  $i = 0, \dots, n_c$ :

(1) The Cartesian coordinate is approximated as

$$x(\xi) = \sum_{i=0}^n N_i(\xi) \cdot x_i. \tag{8}$$

(2) The variable is approximated as

$$u(\xi) = \sum_{i=0}^n N_i(\xi) \cdot a_i. \tag{9}$$

It is worth mentioning that the coefficients  $a_i$  in (9) are generally different from the nodal values  $u_i$  associated to the breakpoints, except at the ends where  $a_0 = u_0$  and  $a_n = u_n$ .

**Remark.** In the particular case in which there are no internal breakpoints (i.e.,  $n = 1$ ), (5) implies that the knot vector consists of  $m + 1 = 2(p + 1)$  elements, whence (7) implies that the number of control points becomes  $n_c = p$ . In other words, in case of Bézier (Bernstein polynomial) representation, the number of coefficients is identical with those involved in a Taylor series, that is, a full polynomial of degree  $p$ .

**2.3. Two-dimensional global shape functions.** Given the uniform subdivisions  $n_x$  and  $n_y$  of the intervals  $[0, a]$  and  $[0, b]$ , respectively, the breakpoints along each of the four sides ( $AB$ ,  $BC$ ,  $CD$ , and  $DA$ ) are determined. Moreover, given the multiplicity of internal knots, as well as the polynomial degrees  $p_x$  and  $p_y$ , the control points in the  $x$ - and  $y$ -direction are also determined. If the patch is curvilinear, then  $x$ - and  $y$ -coordinates have to be replaced by the  $\xi$ - and  $\eta$ -normalized coordinates, respectively.

While in the older B-splines formulation [Schoenberg 1946; Schoenberg and Whitney 1953] the degrees of freedom are associated to the  $(n_x + 1) \times (n_y + 1)$  nodal points  $x_{ij}$  lying at the intersections of  $i$ -th and  $j$ -th lines perpendicular to the axes and passing through the breakpoints  $(x_i, y_j)$ , in this “modern” formulation we have to deal only with the tensor product of  $q$  control points. Therefore, in the case of cubic approximation ( $p_x = p_y = p = 3$ ), we distinguish two cases. In the first case, the multiplicity of internal knots is  $\lambda = 1$ , so the tensor product consists of  $q = (n_x + 3) \times (n_y + 3)$  coefficients  $a_{ij}$ . In the second case, the multiplicity of internal knots is  $\lambda = 2$ , so the tensor product consists of  $q = 4(n_x + 1)(n_y + 1)$  coefficients  $a_{ij}$ .

Therefore, according to the selected value of multiplicity  $\lambda$  (1 or 2), the two-dimensional global shape functions are given by

$$\lambda = 1: \quad \phi_{ij}(x, y) = N_i(x) \cdot N_j(y), \quad i = 0, \dots, (n_x + 3) \wedge j = 0, \dots, (n_y + 3), \tag{10}$$

$$\lambda = 2: \quad \phi_{ij}(x, y) = N_i(x) \cdot N_j(y), \quad i = 0, \dots, 2(n_x + 1) \wedge j = 0, \dots, 2(n_y + 1) \tag{11}$$

(the double subscript is to emphasize the two directions).

The continuity of the approximation is prescribed by both the polynomial degree and the multiplicity. For cubic splines, if the multiplicity is one, then the univariate approximation is  $C^2$ -continuous (whereas for 2D,  $u \in C^{2,2}(\Omega_{st})$ ). In contrast, if the multiplicity is two, then the univariate approximation is  $C^1$ -continuous (whereas for 2D,  $u \in C^{1,1}(\Omega_{st})$ );  $\Omega_{st} = [0, 1] \times [0, 1]$  is the *standard* reference square.

In the general case of higher polynomial degrees,  $p > 3$ , the B-splines approximation ensures  $C^{p-\lambda}$ -continuity when the multiplicity of inner knots is  $\lambda$  ( $1 \leq \lambda \leq p - 1$ ). The most usual case for the numerical solution of an ordinary differential equation by collocation is to require  $C^1$ -continuity (multiplicity  $\lambda = p - 1$ ) and take  $\lambda$  collocation points between any two successive breakpoints. Under these circumstances, after encountering the two boundary conditions we obtain as many equations as the number of unknowns (this observation is useful to static problems, for which the reader is referred to [Appendix A](#), and dynamic ones). Therefore, the minimum value of multiplicity  $\lambda$  is 1 ( $C^{p-1}$ -continuity), whereas the maximum one is  $p - 1$  ( $C^1$ -continuity).

In general, the  $q$  control points are divided into two categories, that is,  $n_{c,in}$  in the interior of the domain  $\Omega$  and  $n_{c,b}$  near the boundary ( $q = n_{c,in} + n_{c,b}$ ). In more detail, if a side of the quadrilateral  $ABCD$  (e.g.,  $AB$ ) is straight, the corresponding control points lie on this side ( $AB$ ). In contrast, if the side is curved, then only the extreme control points ( $P_0$  and  $P_n$ ) will belong to the boundary, and even they coincide with the corners (e.g.,  $A, B$ ), whereas the rest will be either inside or outside the domain  $\Omega$  in accordance to the curvature of the curve  $AB$ .

### 3. The proposed global collocation procedure

**3.1. General.** For the given partial differential equation (PDE)

$$\frac{1}{c^2} \frac{\partial^2 u}{\partial t^2} - \nabla^2 u = 0 \quad \text{in } \Omega, \tag{12}$$

we seek an approximate solution to (12) which is a linear combination of the bivariate global *basis* functions  $\{\phi_i(x, y)\}$ ,  $i = 1, 2, \dots, q$ :

$$\tilde{u}(x, y; t) = \sum_{j=1}^q \alpha_j(t) \cdot \phi_j(x, y). \tag{13}$$

Based on the global shape functions  $\phi_j$  in (13), which are applied for the entire domain, we can apply either the proposed global collocation or the well-known Galerkin–Ritz method.

Without loss of generality, the boundary consists of  $\tilde{n}_1$  breakpoints (which correspond to  $n_1$  control points) under Dirichlet and  $\tilde{n}_2$  ones (which correspond to  $n_2$  control points) under Neumann boundary conditions. Although many acoustical cavities have absorbing boundaries (e.g., mufflers) with mixed boundary conditions (Robin-type) due to the acoustic impedance, for the sake of brevity below we limit the discussion in the two typical cases of boundary conditions, that is, open boundary (Dirichlet-type) and hard walls (Neumann-type).

**3.2. The proposed global collocation approach.** Fulfilling the PDE (12) at  $n_{col}$  collocation points, one obtains the matrix formulation (the index “c” stands for collocation)

$$[M_c]\{\ddot{\mathbf{a}}(t)\} + [K_c]\{\mathbf{a}(t)\} = \{\mathbf{0}\}, \tag{14}$$

where

$$m_{ij}^c = \left(\frac{1}{c^2}\right)\phi_j(x_i), \quad k_{ij}^c = -\nabla^2\phi_j(x_i). \quad (15)$$

In (15), “ $i$ ” corresponds to the collocation points and “ $j$ ” to the control points. It can be noticed that in this formulation *no domain integral appears*. This advantage comes at the cost of having to calculate the stiffness elements  $k_{ij}$  through the two components of the Laplace operator in (15), which are given by

$$\begin{aligned} \frac{\partial^2\phi_j}{\partial x^2} &= \left(\frac{\partial\xi}{\partial x}\right)^2 \frac{\partial^2\phi_j}{\partial\xi^2} + 2\frac{\partial\xi}{\partial x} \frac{\partial\eta}{\partial x} \frac{\partial^2\phi_j}{\partial\xi\partial\eta} + \left(\frac{\partial\eta}{\partial x}\right)^2 \frac{\partial^2\phi_j}{\partial\eta^2} + \frac{\partial^2\xi}{\partial x^2} \frac{\partial\phi_j}{\partial\xi} + \frac{\partial^2\eta}{\partial x^2} \frac{\partial\phi_j}{\partial\eta}, \\ \frac{\partial^2\phi_j}{\partial y^2} &= \left(\frac{\partial\xi}{\partial y}\right)^2 \frac{\partial^2\phi_j}{\partial\xi^2} + 2\frac{\partial\xi}{\partial y} \frac{\partial\eta}{\partial y} \frac{\partial^2\phi_j}{\partial\xi\partial\eta} + \left(\frac{\partial\eta}{\partial y}\right)^2 \frac{\partial^2\phi_j}{\partial\eta^2} + \frac{\partial^2\xi}{\partial y^2} \frac{\partial\phi_j}{\partial\xi} + \frac{\partial^2\eta}{\partial y^2} \frac{\partial\phi_j}{\partial\eta}. \end{aligned} \quad (16)$$

The terms  $\frac{\partial\xi}{\partial x}$ ,  $\frac{\partial^2\xi}{\partial x^2}$ ,  $\frac{\partial\xi}{\partial y}$  and  $\frac{\partial^2\xi}{\partial y^2}$ , as well as  $\frac{\partial\eta}{\partial x}$ ,  $\frac{\partial^2\eta}{\partial x^2}$ ,  $\frac{\partial\eta}{\partial y}$  and  $\frac{\partial^2\eta}{\partial y^2}$  in (16), are calculated as usual, starting from the inverse of the Jacobian matrix [Provatidis and Ioannou 2010, p. 400].

**3.3. The well known Galerkin–Ritz approach.** Applying the Galerkin method to (12), for the free vibration problem, one obtains the well known matrix formulation [Höllig 2003]

$$[\mathbf{M}]\{\ddot{\mathbf{a}}(t)\} + [\mathbf{K}]\{\mathbf{a}(t)\} = \{\mathbf{0}\}, \quad (17)$$

where  $[\mathbf{M}]$  and  $[\mathbf{K}]$  are the mass and stiffness matrices, respectively, which are given by

$$m_{ij} = \frac{1}{c^2} \int_{\Omega} \phi_i\phi_j d\Omega, \quad k_{ij} = \int_{\Omega} \nabla\phi_i\nabla\phi_j d\Omega. \quad (18)$$

A B-splines implementation in conjunction with Equations (17) and (18) is not a novel task, as the general procedure has been previously presented in a textbook ([Höllig 2003] and papers therein). For the completeness of our description, we should mention that

- (1) *Dirichlet* boundary conditions (near to  $n_1 \leq n_{c,b}$  control points) are easily implemented eliminating both the  $n_1$  rows and columns which correspond to the restrained coefficients;
- (2) *Neumann* boundary conditions (near to  $n_2 \leq n_{c,b}$  control points) make the “near-boundary” (outer) control points be treated equally with the  $n_{c,in}$  unrestrained internal ones. In the particular case of a *free-free* problem, *no* matrix elimination is required.

**3.4. Implementation of boundary conditions in global collocation.** In general, we fulfill the PDE applying (15) at  $n_{col}$  collocation points in the interior of the domain.

In free acoustic excitation, the collocation leads to the following general matrix equations system

$$[\mathbf{M}_{col,1} \quad \mathbf{M}_{col,2} \quad \mathbf{M}_{col,I}] \cdot \begin{bmatrix} \ddot{\mathbf{a}}_1 \\ \ddot{\mathbf{a}}_2 \\ \ddot{\mathbf{a}}_I \end{bmatrix} + [\mathbf{K}_{col,1} \quad \mathbf{K}_{col,2} \quad \mathbf{K}_{col,I}] \cdot \begin{bmatrix} \mathbf{a}_1 \\ \mathbf{a}_2 \\ \mathbf{a}_I \end{bmatrix} = \begin{bmatrix} \mathbf{F}_1 \\ \mathbf{0} \\ \mathbf{0} \end{bmatrix}, \quad (19)$$

where  $\mathbf{a}_1$  and  $\mathbf{a}_2$  are vectors of coefficients that refer to the above-mentioned  $n_1$  and  $n_2$  control points related to the boundary, respectively, while  $\mathbf{a}_I$  refers to the associated  $n_I$  “internal” (with respect to the reference square) control points.



**3.4.1. Dirichlet boundary conditions.** Dirichlet boundary conditions ( $u = 0$ ) are easily applied. These conditions are readily implemented by eliminating the columns that correspond to the restricted nodes, that is, the matrices  $\mathbf{M}_{\text{col},1}$  and  $\mathbf{K}_{\text{col},1}$  in (19). In most cases this task is trivial, particularly when one or more entire sides, for example  $AB$  out of the whole boundary ( $= AB \cup BC \cup CD \cup DA$ ), is restricted ( $u = 0$ ). Obviously this happens because the boundary condition  $u = 0$  along the side  $AB$  implies that all coefficients that correspond to it vanish ( $a_i \equiv 0$ ). If the entire boundary is under Dirichlet conditions, then all relevant coefficients vanish (i.e.,  $\mathbf{a}_1 = \mathbf{0}$ ).

Therefore, eliminating the vectors  $\mathbf{a}_1 = \ddot{\mathbf{a}}_1 = \mathbf{0}$ , and assuming that no other part of the boundary is under Neumann conditions ( $\mathbf{a}_2$  is absent), (19) becomes

$$\mathbf{M}_{\text{col},I} \cdot \ddot{\mathbf{a}}_I + \mathbf{K}_{\text{col},I} \cdot \mathbf{a}_I = \mathbf{0}. \tag{20}$$

Equation (20) depicts that the resulting matrices  $\mathbf{M}_{\text{col},I}$  and  $\mathbf{K}_{\text{col},I}$  will be square (of order  $n_{c,\text{in}} \times n_{c,\text{in}}$ ) only when the number of collocation points equals the number of control points  $n_{c,\text{in}}$  in the interior. Obviously, this condition is valid regardless of the multiplicity  $\lambda$  ( $= 1$  or  $2$ ) of internal knots.

**3.4.2. Neumann boundary conditions.** Neumann boundary conditions ( $\partial u / \partial \mathbf{n} = 0$ ,  $\mathbf{n} =$  unit normal vector) impose a linear dependency between the coefficients associated to the control points in the neighborhood of the boundary. A similar dependency had been previously found, however in conjunction with Lagrange polynomials [Provatidis 2008a, p. 245]. In this way, the matrix elements in those columns related to the free boundary are first reorganized and then condensed; details will be given below.

Taking the first derivative of (13) with respect to the unit normal vector  $\mathbf{n}$  (at a boundary point), we obtain

$$\frac{\partial u}{\partial \mathbf{n}} = \sum_{k=1}^q \frac{\partial \phi_k(\xi, \eta)}{\partial \mathbf{n}} \cdot a_k. \tag{21}$$

In the sum that appears in (21),  $n_{c,\text{in}}$  out of the total number of  $q$  control points belong to the interior, while  $n_2$  belong to the boundary (actually they are outside or inside the domain in accordance to the curvature). For a smooth boundary, applying (21) to  $n_2$  boundary points (in the neighborhood of the “close-to-the-boundary” control points), we derive the matrix equation

$$\begin{bmatrix} \mathbf{B}_{22} \\ \mathbf{B}_{2I} \end{bmatrix}_{\substack{n_2 \times n_2 \\ n_2 \times n_I}} \cdot \begin{bmatrix} \mathbf{a}_2 \\ \mathbf{a}_I \end{bmatrix} = \begin{bmatrix} \mathbf{0} \\ \mathbf{0} \end{bmatrix}. \tag{22}$$

Eliminating  $\mathbf{a}_2$  from (22) and substituting into (19) in which the vector  $\mathbf{a}_1$  is absent, we obtain

$$\mathbf{M}^* \ddot{\mathbf{a}}_I + \mathbf{K}^* \mathbf{a}_I = \mathbf{0}, \tag{23}$$

where

$$\mathbf{M}^* = \mathbf{M}_{\text{col},I} - \mathbf{M}_{\text{col},2} \mathbf{B}_{22}^{-1} \mathbf{B}_{2I}, \quad \mathbf{K}^* = \mathbf{K}_{\text{col},I} - \mathbf{K}_{\text{col},2} \mathbf{K}_{22}^{-1} \mathbf{K}_{2I}. \tag{24}$$

The imposition of Neumann boundary conditions in the case of nonsmooth boundary (e.g., corners appearing in a rectangular  $ABCD$  like that of Example 1, free-free boundary conditions) is performed as follows. We select two opposite sides, for example  $AD$  and  $BC$  and impose the Neumann boundary conditions at so many points along each of them as the number of the corresponding control points (the end points ( $A, D$ ) of the side  $AD$ , and ( $B, C$ ) of  $BC$  are included). For the remaining two sides,  $AB$

and  $CD$ , the corner points are excluded, therefore for each of them Neumann boundary conditions are applied to as many boundary points as the corresponding number of control points minus two. This is the minimum number of Neumann boundary conditions that can be applied in a straightforward manner. However, if one wishes to apply Neumann boundary conditions at the ends of the sides  $AB$  and  $CD$  as well, then the number of rows in (22) will increase by four, thus a least-squares procedure should be applied to it in order to make possible the inversion of matrix  $\mathbf{B}_{22}$ .

**3.4.3. Implementation to static problems.** At this point, it is instructive to refresh those basics of the collocation method related to nonhomogeneous boundary conditions for solving boundary value problems. Details for the one-dimensional problem defined in the interval  $[0, L]$  are given in [Appendix A](#).

**3.4.4. Multiplicity of internal knots.** As mentioned in [Section 2.3](#), after the breakpoints along the boundary are given, the next decisive step is to assign the multiplicity of internal knots.

In the case of  $\lambda = 2$ , in conjunction with  $p = 3$ , the golden rule is to take the collocation points at the  $2 \times 2$  Gauss points in the  $(n_x \times n_y)$  cells formed by the breakpoints, so that the number of equations equals the number of unknowns, always related to the internal control points. For  $p > 3$ , the same occurs when  $\lambda = p - 1$ , whereas the aforementioned  $2 \times 2$  is replaced by a  $(p - 1) \times (p - 1)$  Gaussian quadrature.

In contrast, when  $\lambda = 1$ , in conjunction with  $p = 3$ , we can use more collocation points, for example, the same as those for  $\lambda = 2$ . In such case the matrices  $\mathbf{M}_{\text{col},I}$  and  $\mathbf{K}_{\text{col},I}$  are nonsquare. For  $p > 3$ , we can use the same as those for  $\lambda = p - 1$  or smaller. This shortcoming is easily resolved applying the least-squares technique, of which the academic implementation is to left-multiply (20) by the transpose of the matrix  $\mathbf{M}_{\text{col},I}$ , thus leading to

$$\underbrace{\bar{\mathbf{M}}}_{n_I \times n_I} \ddot{\mathbf{a}}_I + \underbrace{\bar{\mathbf{K}}}_{n_I \times n_I} \mathbf{a}_I = \mathbf{0}, \quad (25)$$

where

$$\bar{\mathbf{M}} = (\mathbf{M}_{\text{col},I})^T \cdot (\mathbf{M}_{\text{col},I}), \quad \bar{\mathbf{K}} = (\mathbf{M}_{\text{col},I})^T \cdot (\mathbf{K}_{\text{col},I}). \quad (26)$$

In the case of adopting  $\lambda = 1$  ( $C^{p-\lambda}$ -continuity), another possibility is to collocate at the images of the Demko's or Greville's abscissae [[Auricchio et al. 2010](#); [de Boor 2001](#), p. 192], thus skipping the above-mentioned least-squares procedure. For the sake of brevity, in this paper a relevant choice is characterized by the term "isogeometric" collocation.

**3.4.5. Eigenvalues extraction.** It can be noticed that (20) and (23) have the form of a standard problem in dynamics and therefore can be calculated either taking the roots of the characteristic polynomial produced by demanding that  $\det(\|\mathbf{K} - \lambda\mathbf{M}\|) = 0$ , or by any established algorithm for nonsymmetric matrices such as  $QR$ .

## 4. Numerical implementation

**4.1. Global collocation method.** The proposed global collocation method was implemented using  $(p - 1)$  Gauss points per direction, between any two successive breakpoints. In the tensor product, the breakpoints create  $n_x \times n_y$  cells. Using  $(p - 1)^2$  collocation points per cell, the total number of collocation points becomes  $n_{\text{col}} = (p - 1)^2 n_x n_y$ , which equals to the number of unknown coefficients.

Clearly, in the case of multiple double knots (e.g.,  $\lambda = 2$  for  $p = 3$ ) the total number of control points (coefficients) in the tensor product is  $q = 4(n_x + 1) \times (n_y + 1)$ , of which  $n_b = 4(n_x + n_y + 1)$  control points (coefficients) lie on the boundary.

- For a *Dirichlet* problem (e.g., with  $p = 3$ ), the aforementioned  $n_b$  columns are eliminated, thus  $n_{\text{int}} = q - n_b = 4n_x n_y$  coefficients remain (they correspond to the control points in the interior). Therefore, the number of the collocation points  $n_{\text{col}}$  equals to the number of unknown coefficients, a fact that leads to a square matrix of unknowns which can be easily solved.
- For a *free-free* problem, all coefficients that correspond to the boundary control points are again eliminated, thus resulting in  $n_{\text{int}} = q - n_b = 4n_x n_y$ , exactly the same number as in the above-mentioned Dirichlet problem.

Also, in case of simple knots ( $\lambda = 1$ ), in conjunction with  $p = 3$ , the total number of control points (coefficients) in the tensor product is  $q = (n_x + 3) \times (n_y + 3)$ , of which  $n_b = 2(n_x + n_y + 4)$  control points (coefficients) lie on the boundary. As previously, in both Dirichlet and Neumann problems all the coefficients associated to the  $n_b$  close-to-boundary control points are eliminated thus  $n_{\text{int}} = q - n_b = 4n_x n_y$  coefficients remain and constitute the order of the final matrices.

Moreover, for any chosen multiplicity  $\lambda$ , in conjunction with a chosen number of breakpoint subdivisions, the number  $q$  of control points is determined according to (7). In addition to the above schemes, instead of using only Gaussian points this study reports about numerical experience using the images of Demko's and Greville's abscissae for collocating points, previously applied in isogeometric analysis [Auricchio et al. 2010].

**4.2. Galerkin–Ritz global method.** The elements  $m_{ij}$  of the mass matrix are products of two basis functions, each of piecewise  $p$ -th (i.e., third) degree. In the particular case of a rectangular domain, the integrand becomes of piecewise sixth degree, thus it requires four-point Gauss quadrature per direction, that is, sixteen Gauss points per integration cell. For  $p > 3$ , we use  $(p + 1) \times (p + 1)$  Gauss points per integration cell.

A Dirichlet problem, for  $p = 3$ , leads to mass and stiffness matrices of order  $n_{\text{int}} = q - n_b = 4n_x n_y$ , while a Neumann problem leads to matrices of order  $n_{\text{eq}} = 4(n_x + 1) \times (n_y + 1)$ , a fact that is entirely different from the above-mentioned collocation technique.

## 5. Numerical examples

A Matlab code was developed on a standard PC Pentium IV. The basis functions  $N_{i,p}$  and their derivatives were created using the “spscol” function, which exists in the Spline Toolkit. Demko's abscissae were determined using the “chbpnt” function. The eigenvalues were calculated using the standard “eig” function.

The theory is now elucidated by two examples taken from the literature [Provatidis 2004; 2009a], in which the exact analytical solution is known. The quality of the numerical solution  $\tilde{u}$  is evaluated in terms of the relative error, which was calculated as

$$e_r = \frac{\tilde{u} - u_{\text{exact}}}{u_{\text{exact}}} \times 100\%. \quad (27)$$

Mode $(m, n)$ Exact $\omega^2$			Error (in %) of calculated eigenvalues											
			Collocation								Galerkin–Ritz			
			(a) $\lambda = 2$ $(n_x \times n_y)$				(b) $\lambda = 1$ $(n_x \times n_y)$				(c) $\lambda = 1$ $(n_x \times n_y)$			
			2 × 1	4 × 2	6 × 3	8 × 4	2 × 1	4 × 2	6 × 3	8 × 4	2 × 1	4 × 2	6 × 3	8 × 4
1	(0, 0)	0	—	—	—	—	—	—	—	—	—	—	—	—
2	(1, 0)	1.5791	0.23	0.02	0.00	0.00	0.26	0.02	0.00	0.00	0.06	0.00	0.00	0.00
3	(2, 0)	6.3165	−8.81	0.23	0.05	0.02	−8.81	0.26	0.05	0.02	0.10	0.09	0.01	0.00
4	(0, 1)	8.1567	−8.81	0.23	0.05	0.02	−8.81	0.26	0.05	0.02	0.06	0.06	0.00	0.00
5	(1, 1)	9.7358	−7.35	0.19	0.04	0.01	−7.34	0.22	0.04	0.01	0.06	0.05	0.00	0.00
6	(3, 0)	14.2122	−7.14	0.67	0.23	0.08	−7.14	1.83	0.26	0.08	1.91	1.91	0.10	0.01
7	(2, 1)	14.4732	10.35	0.23	0.05	0.02	—	0.26	0.05	0.02	88.07	0.65	0.00	0.00
8	(3, 1)	22.3689	4.65	0.51	0.16	0.06	—	1.26	0.19	0.06	58.17	1.61	0.07	0.01
9	(4, 0)	25.2662	—	−8.81	0.55	0.23	—	−8.81	1.01	0.26	93.83	0.12	1.01	0.11
10	(0, 2)	32.6268	—	−8.81	0.55	0.23	—	−8.81	1.01	0.26	51.98	0.10	0.84	0.09
Number of equations			8	32	72	128	6	15	28	45	20	35	54	77

**Table 1.** Example 1: calculated eigenvalues of a rectangular acoustic cavity ( $a = 2.5$  m,  $b = 1.1$  m) under *Neumann* (free-free:  $\partial u/\partial n = 0$ ) boundary conditions, using various  $n_x \times n_y$  uniform subdivisions in conjunction with cubic B-splines ( $p = 3$ ). Results are shown as percentage errors for an approximation involving “tensor product B-splines” using three alternative formulations: (a) *collocation* (with multiplicity  $\lambda = 2$ ), (b) *collocation* (with multiplicity  $\lambda = 1$ ), and (c) *Galerkin–Ritz* (with multiplicity  $\lambda = 1$ ).

**Example 1: eigenvalues of rectangular acoustical cavity.** We consider a rectangular acoustical cavity of dimensions  $a = 2.5$  m,  $b = 1.1$  m with sound velocity  $c = 1$  m/s. Two types of boundary conditions are considered: (a) *Neumann* (free-free), and (b) *Dirichlet* boundary conditions, for which the exact analytical eigenvalues are given by

$$\text{Free-free: } \omega_{mn}^2 = \pi^2 c^2 \left( \frac{m^2}{a^2} + \frac{n^2}{b^2} \right), \quad m, n = 0, 1, 2, \dots, \tag{28}$$

$$\text{Dirichlet: } \omega_{mn}^2 = \pi^2 c^2 \left( \frac{m^2}{a^2} + \frac{n^2}{b^2} \right), \quad m, n = 1, 2, \dots \tag{29}$$

In all cases a uniform mesh of  $(n_x \times n_y)$  subdivisions of breakpoints along  $x$ - and  $y$ -directions, respectively, has been used. The obtained results for  $p = 3$  are shown in Tables 1–3. In more detail:

- (1) Table 1 shows the results for *Neumann* boundary conditions, for three different formulations, that is, B-splines collocation in conjunction with the usual multiplicity  $\lambda = 2$  and the novel  $\lambda = 1$ , as well as B-splines Galerkin–Ritz with the usual multiplicity  $\lambda = 1$ . It can be noticed that both formulations are of similar quality. The proposed collocation method requires the most degrees of freedom when  $\lambda = 2$  and the least when  $\lambda = 1$ .
- (2) Table 2 shows the results for *Dirichlet* boundary conditions, again for previous three different formulations. It can be noticed that again the proposed collocation and the Galerkin–Ritz are of the same quality. It can be also noticed that the alternative least-squares collocation ( $\lambda = 1$ ) is almost

Mode (m, n)      Exact $\omega^2$			Error (in %) of calculated eigenvalues											
			Collocation								Galerkin-Ritz			
			(a) $\lambda = 2$ ( $n_x \times n_y$ )				(b) $\lambda = 1$ ( $n_x \times n_y$ )				(c) $\lambda = 1$ ( $n_x \times n_y$ )			
			2 × 1	4 × 2	6 × 3	8 × 4	2 × 1	4 × 2	6 × 3	8 × 4	2 × 1	4 × 2	6 × 3	8 × 4
1	(1, 1)	9.7358	18.12	0.19	0.04	0.01	18.12	0.19	0.04	0.01	1.11	0.02	0.01	0.00
2	(2, 1)	14.4732	21.59	0.23	0.05	0.02	25.38	0.24	0.05	0.02	3.53	0.06	0.01	0.00
3	(3, 1)	22.3689	15.74	0.51	0.16	0.06	15.74	0.67	0.18	0.06	4.36	0.45	0.07	0.01
4	(4, 1)	33.4229	-6.25	16.37	0.43	0.17	-6.25	31.89	0.64	0.20	8.58	8.58	0.57	0.09
5	(1, 2)	34.2059	-3.65	20.59	0.52	0.22	11.04	36.69	0.58	0.24	21.12	15.69	0.20	0.09
6	(2, 2)	38.9433	-3.88	18.12	0.47	0.19	17.41	25.40	0.52	0.21	27.85	5.37	0.18	0.08
7	(3, 2)	46.8390	-2.38	11.03	0.45	0.18	—	20.44	0.50	0.20	—	4.66	0.18	0.07
8	(5, 1)	47.6351	10.83	13.31	0.42	0.39	—	19.34	1.13	0.55	—	9.00	1.95	0.46
9	(4, 2)	57.8930	—	21.59	0.55	0.23	—	40.06	0.70	0.25	—	14.22	0.45	0.11
10	(6, 1)	65.0056	—	10.85	11.50	0.59	—	29.34	12.05	1.21	—	20.72	12.46	1.59
Number of equations			8	32	72	128	6	15	28	45	6	15	28	45

**Table 2.** Example 1: calculated eigenvalues of a rectangular acoustic cavity ( $a = 2.5$  m,  $b = 1.1$  m) under *Dirichlet* ( $u = 0$ ) boundary conditions, using various  $n_x \times n_y$  uniform subdivisions in conjunction with cubic B-splines ( $p = 3$ ). Results are shown as percentage errors for an approximation involving “tensor product B-splines” using three alternative formulations: (a) *collocation* (with multiplicity  $\lambda = 2$ ), (b) *collocation* (with multiplicity  $\lambda = 1$ ), and (c) *Galerkin-Ritz* (with multiplicity  $\lambda = 1$ ).

Mode		Error (in %) of calculated eigenvalues							
		Conventional finite elements (FEM)							
		(a) Free-free ( $n_x \times n_y$ )				(b) Dirichlet ( $n_x \times n_y$ )			
		2 × 1	4 × 2	6 × 3	8 × 4	2 × 1	4 × 2	6 × 3	8 × 4
1		—	—	—	—	—	18.93	8.27	4.60
2		21.59	5.24	2.30	1.29	—	21.59	9.43	5.24
3		21.59	21.59	9.43	5.24	—	35.00	17.15	9.54
4		21.59	21.59	9.43	5.24	—	—	30.11	17.60
5		21.59	18.93	8.27	4.60	—	—	35.19	20.65
6		23.82	23.82	11.44	7.17	—	—	32.35	18.93
7		—	40.13	19.39	9.98	—	—	32.17	18.68
8		—	35.00	17.15	9.54	—	—	38.13	28.29
9		—	21.59	36.78	21.59	—	—	36.78	21.59
10		—	21.59	33.28	20.47	—	—	56.14	38.00
Number of equations		6	15	28	45	0	3	10	21

**Table 3.** Example 1: calculated eigenvalues of a rectangular acoustic cavity ( $a = 2.5$  m,  $b = 1.1$  m) using various  $n_x \times n_y$  uniform subdivisions. Results are shown as percentage errors for conventional bilinear (four-node) finite elements under (a) free-free and (b) Dirichlet boundary conditions.



identical with the orthogonal collocation ( $\lambda = 2$ ) and even it has the same (small) number of control points as the Galerkin–Ritz formulation.

- (3) For comparison, Table 3 shows the results obtained using conventional finite elements—for the same mesh density, of course. It can be noticed that the minor differences appearing in Table 1 and Table 2 are negligible, that is, of the same order of accuracy when compared with the conventional finite element solution in Table 3. However, for the same number of breakpoints, the number of DOFs in the conventional FEM is minimal.

In the sequence, the results of Tables 1–3 are enhanced as follows. First, the discretization of breakpoints is extended from  $8 \times 4$  to  $12 \times 6$ ,  $16 \times 8$  and  $32 \times 16$  at maximum. Second, three additional collocation schemes from recent literature were tested, involving, in order, Demko’s, Greville’s  $T_n$ - and Greville’s  $S_{n+2}$  abscissae (for definitions see [Auricchio et al. 2010]).

Comparative results for  $p = 3$  and Neumann boundary conditions are shown in Figure 1, where one can

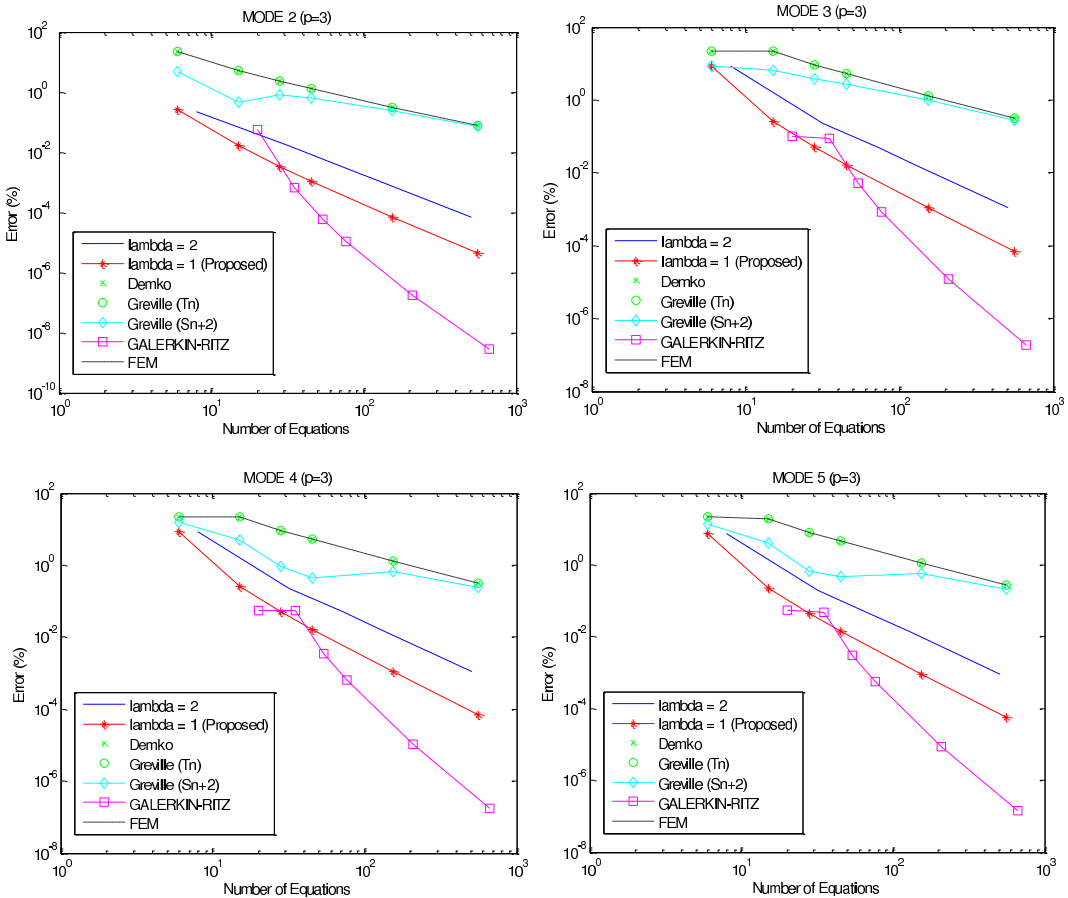


**Figure 1.** Rectangular under Neumann boundary conditions: Convergence of the first four nonzero eigenvalues,  $\omega_i^2$ ,  $i = 2, 3, 4, 5$ , in terms of number of equations using cubic B-splines,  $p = 3$  (the first eigenvalue, not shown, equals to zero:  $\omega_1^2 = 0$ ).

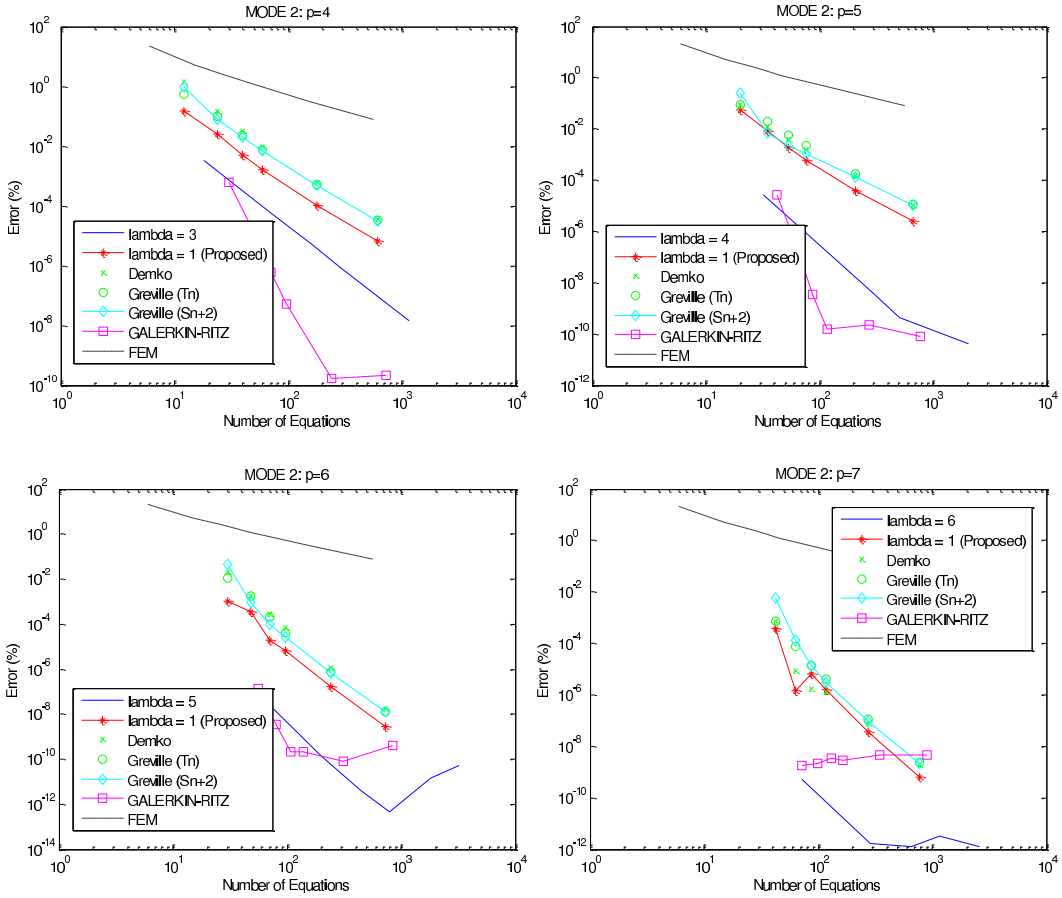


**Figure 2.** Rectangular under *Neumann* boundary conditions: convergence of the second eigenvalue,  $\omega_2^2$ , in terms of number of equations, for higher polynomial degrees ( $p = 4, 5, 6$  and  $7$ ).

notice the overall superiority of the Galerkin–Ritz B-splines method, in terms of accuracy. The proposed single knot based ( $\lambda = 1$ ) least-squares collocation closely follows the accuracy of Galerkin–Ritz method, whereas the usual double knot based ( $\lambda = 2$ ) collocation method is of adequate accuracy. Moreover, the images of Demko’s and Greville’s abscissae as collocation points lead to rather poor results. Surprisingly, Demko’s solution coincides with the conventional FEM solution (based on 4-node bilinear elements) up to the twelfth decimal point at least.

For the same (Neumann) boundary conditions, the superiority of the proposed method ( $\lambda = 1$ ) does not continue when dealing with higher polynomial degrees ( $p = 4, 5, 6$  and  $7$ ), where the choice of multiplicity  $\lambda = p - 1$  outperforms between all collocation methods tested in this study (Figure 2).

Comparative results for  $p = 3$  and *Dirichlet* boundary conditions are shown in Figure 3, where one can again notice the overall superiority of the Galerkin–Ritz B-splines method, in terms of accuracy. The proposed single knot based ( $\lambda = 1$ ) least-squares collocation is again the best accurate scheme between all tested collocation methods. Moreover, the images of Demko’s and Greville’s ( $T_n$ -based) abscissae as

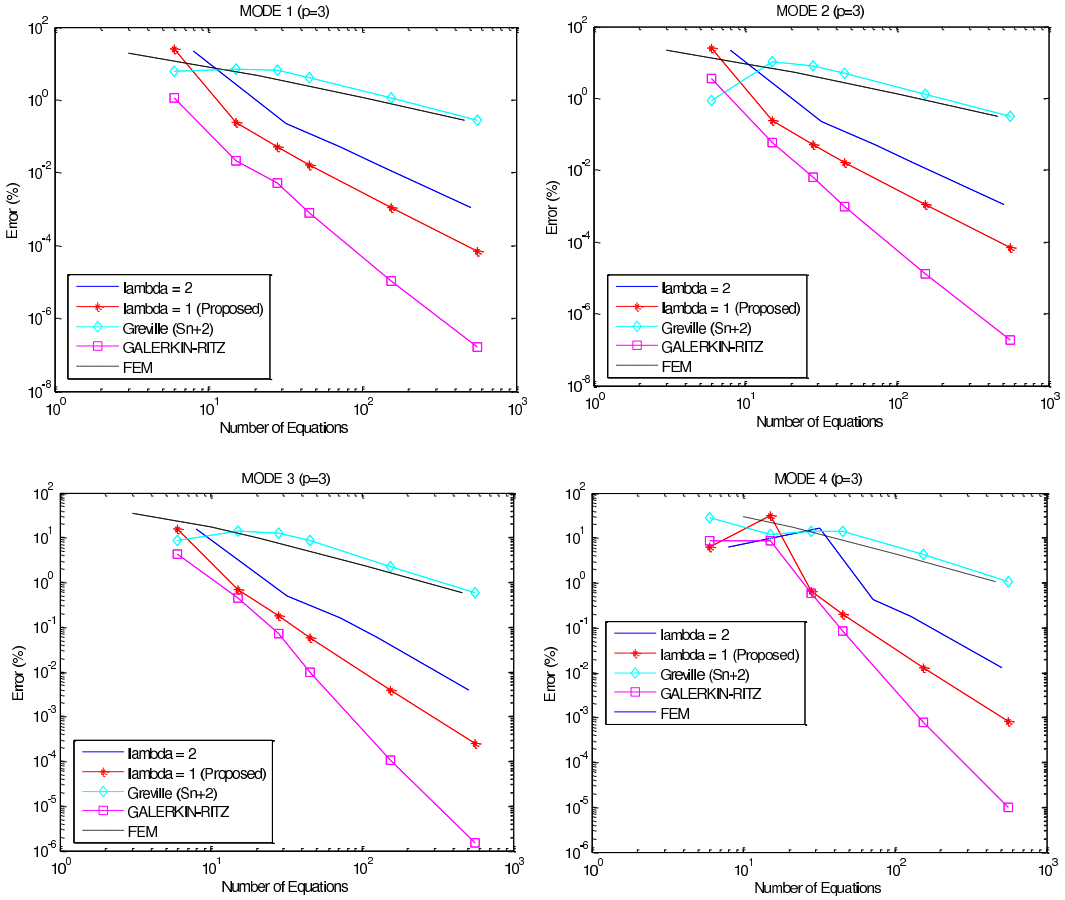


**Figure 3.** Rectangular under *Dirichlet* boundary conditions: convergence of the first four eigenvalues,  $\omega_i^2$ ,  $i = 1, 2, 3, 4$ , in terms of number of equations using cubic B-splines ( $p = 3$ ).

collocation points are not applicable as they lead to singular dynamic matrices. This finding is justified by the fact that the *extreme* collocation points of these two sets *belong* to the boundary and therefore Dirichlet boundary conditions erase the dominating diagonal terms appearing in series expansion given by (13). Only the Greville’s ( $S_{n+2}$ -based) abscissae are applicable but the quality of results is slightly lower compared even with the conventional FEM solution (4-node bilinear elements).

For the same (Dirichlet) boundary conditions, the superiority of the proposed method ( $\lambda = 1$ ) does not continue when dealing with higher polynomial degrees ( $p = 4, 5, 6$  and  $7$ ), where the choice of multiplicity  $\lambda = p - 1$  outperforms between all collocation methods tested in this study (Figure 4). Concerning the other (isogeometric) sets of global collocation, only the images of Greville’s ( $S_{n+2}$ -based) abscissae are applicable and of similar quality with the proposed least-squares scheme.

**Example 2: eigenvalues of circular acoustical cavity.** A circular cavity of radius  $a = 1$  m under Dirichlet or Neumann (free-free) conditions is considered. For the purposes of this study, a unit reference sound

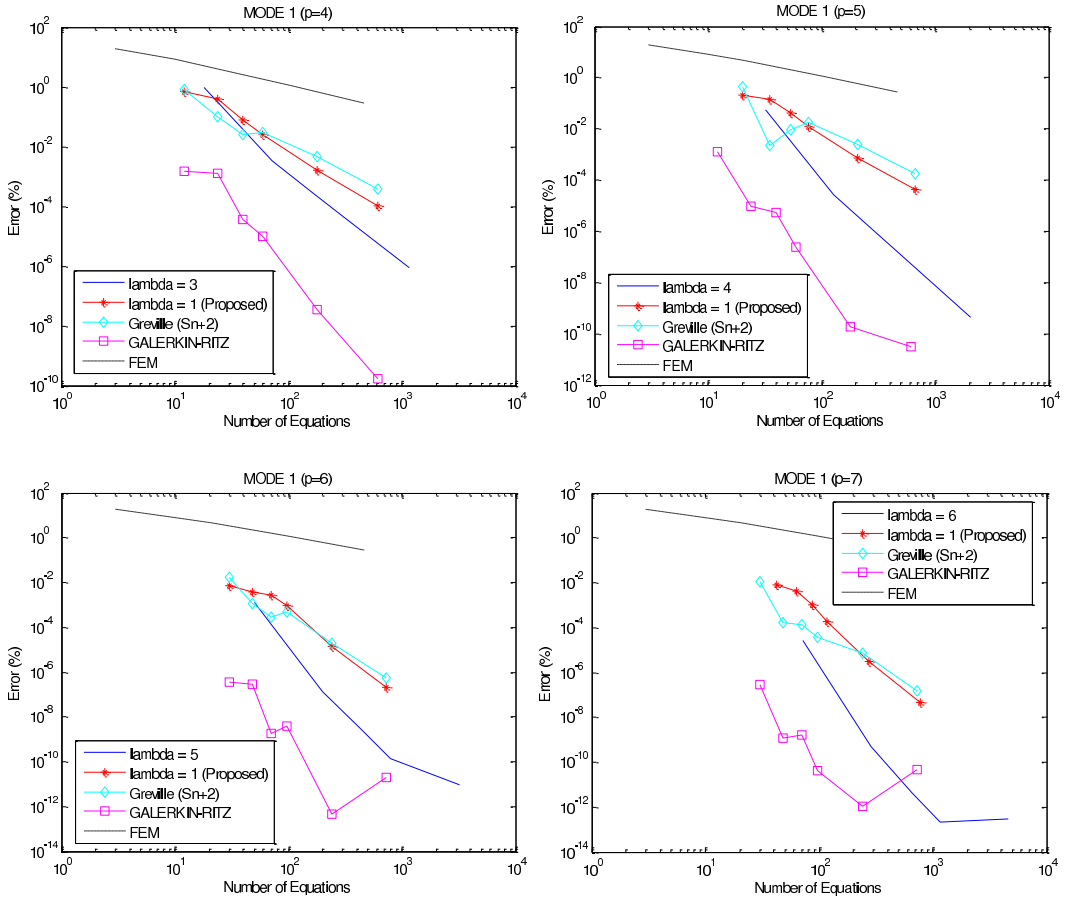


**Figure 4.** Rectangular under *Dirichlet* boundary conditions: convergence of the first eigenvalue,  $\omega_1^2$ , in terms of number of equations, for higher polynomial degrees ( $p = 4, 5, 6$  and  $7$ ).

velocity,  $c = 1$  m/s, is considered. The theoretical eigenvalues are given by the formula

$$\text{Dirichlet: } J_m(ka) = 0, \quad m = 0, 1, 2, \dots, \tag{30}$$

$$\text{Free-free (Neumann): } J'_m(ka) = 0, \quad m = 0, 1, 2, \dots, \tag{31}$$

where  $J'_m(ka)$  is the first derivative of the Bessel function  $J_m(ka)$  of the first kind and order  $m$  and  $k = \omega/c$  the wavenumber.

Now the discretization consists of 4, 8, 16, and 32 breakpoints uniformly distributed along the entire circumference. This corresponds to  $n_x = n_y = n = 1, 2, 4$  and  $8$ , subdivisions of every side in the reference square  $ABCD$ , respectively. As previously, the control points for  $p = 3$  were derived for multiplicity  $\lambda = 1$  and  $2$ .

Tables 4 and 5 show the results for the Dirichlet and Neumann problems, respectively. It can be noticed that for medium and fine meshes the results are of similar quality, especially when they are compared with conventional finite elements. The latter elements have been previously studied in [Provatisidis 2004,

Mode $m$ Exact $\omega^2$			Error (in %) of calculated eigenvalues											
			Collocation								Galerkin-Ritz			
			(a) $\lambda = 2$				(b) $\lambda = 1$				(c) $\lambda = 1$			
			Number of subdivisions ( $4n$ )				Number of subdivisions ( $4n$ )				Number of subdivisions ( $4n$ )			
			4	8	16	32	4	8	16	32	4	8	16	32
1	0	5.7832	97.14	-3.48	0.00	0.00	98.68	-3.70	0.02	0.00	8.94	-0.01	0.01	0.00
2	1	14.6820	39.25	16.63	0.13	0.01	38.98	47.78	0.68	0.01	16.72	11.55	0.46	0.00
3	1	14.6820	39.25	16.63	0.13	0.01	38.98	47.78	0.68	0.01	16.72	11.55	0.46	0.00
4	2	26.3746	-1.59	21.84	-2.23	0.03	-2.54	34.75	-2.20	0.03	29.88	11.97	0.30	0.01
5	2	26.3746	—	33.12	0.88	0.07	—	49.23	3.38	0.09	—	30.32	2.02	0.02
6	0	30.4713	—	27.51	-3.31	0.05	—	195.80	-3.35	0.07	—	26.45	0.16	0.03
7	3	40.7065	—	9.04	-0.20	0.14	—	246.60	2.66	0.19	—	65.18	4.81	0.07
8	3	40.7065	—	9.04	-0.20	0.14	—	246.60	2.66	0.19	—	65.18	4.81	0.07
9	1	49.2185	—	23.30	11.63	0.14	—	327.16	13.92	0.23	—	121.01	20.60	0.17
10	1	49.2185	—	23.30	15.74	0.14	—	—	80.75	0.23	—	—	32.95	0.17
No. of equations			4	16	64	256	4	9	25	81	4	9	25	81

**Table 4.** Example 2: calculated eigenvalues of a circular acoustic cavity of radius 1.0 m under *Dirichlet* ( $u = 0$ ) boundary conditions, using various uniform subdivisions in conjunction with cubic B-splines ( $p = 3$ ). Results are shown as percentage errors for “tensor product B-splines” approximation using three alternative formulations: (a) *collocation* (with multiplicity  $\lambda = 2$ ), (b) *collocation* (with multiplicity  $\lambda = 1$ ), and (c) *Galerkin-Ritz* (with multiplicity  $\lambda = 1$ ).

Mode $m$ Exact $\omega^2$			Error (in %) of calculated eigenvalues											
			Collocation								Galerkin-Ritz			
			(a) $\lambda = 2$				(b) $\lambda = 1$				(c) $\lambda = 1$			
			Number of subdivisions ( $4n$ )				Number of subdivisions ( $4n$ )				Number of subdivisions ( $4n$ )			
			4	8	16	32	4	8	16	32	4	8	16	32
1	0	0.00	—	—	—	—	—	—	—	—	—	—	—	—
2	1	3.3900	-15.28	1.89	0.05	0.00	-15.04	4.27	-0.06	-0.01	0.09	0.29	0.00	0.00
3	1	3.3900	-15.28	1.89	0.05	0.00	-15.04	4.27	-0.06	-0.01	0.09	0.29	0.00	0.00
4	2	9.3284	-43.16	-9.76	-0.17	-0.06	-43.64	-9.77	-0.58	-0.10	-1.13	0.18	0.06	0.00
5	2	9.3284	—	8.61	0.18	0.00	—	23.17	0.42	0.01	50.37	2.71	0.09	0.00
6	0	14.6820	—	-8.50	0.36	0.03	—	-8.81	0.57	0.03	68.85	0.50	0.15	0.00
7	3	17.6500	—	0.44	0.09	-0.08	—	13.95	1.06	-0.11	63.78	9.68	0.76	0.00
8	3	17.6500	—	0.44	0.09	-0.08	—	13.95	1.06	-0.11	63.78	9.68	0.76	0.00
9	4	28.2764	—	-9.27	-2.09	-0.27	—	-1.97	-1.66	-0.43	67.23	9.80	0.45	0.02
10	4	28.2764	—	1.29	2.83	-0.01	—	—	9.40	0.14	90.50	88.13	5.17	0.03
Number of equations			4	16	64	256	4	9	25	81	16	25	49	121

**Table 5.** Example 2: calculated eigenvalues of a circular acoustic cavity of radius 1.0 m under *Neumann* (free-free) boundary conditions, using various uniform subdivisions in conjunction with cubic B-splines ( $p = 3$ ). See caption of previous table for details.



p. 51]; briefly, for the Neumann problem in conjunction with 216 triangular elements and 127 nodes, the error in the first three nonrigid modes was:  $\cong 0.86\%$ ,  $1.36\%$ , and  $1.79\%$ , respectively.

Better insight is obtained when increasing mesh density into 40 breakpoints and again comparing all those methods tested in [Example 1](#). Concerning the FEM, the same mesh with that of breakpoints considered in collocation methods was used. The results are as follows.

For the *Dirichlet* problem, it is clearly shown in [Figure 5](#) that B-splines Galerkin–Ritz method outperforms and then the proposed collocation method ( $\lambda = 1$ ) follows. The images of Demko’s and Greville’s ( $T_n$ -based) abscissae lead to singular matrices, whereas Greville’s ( $S_{n+2}$  based) abscissae work well but perform slightly worse even than usual FEM.

For the *Neumann* problem, it is clearly shown in [Figure 6](#) that B-splines Galerkin–Ritz method again outperforms and then the proposed collocation method ( $\lambda = 1$ ) follows. The images of Demko’s and Greville’s ( $T_n$ -based) abscissae do not now lead to singular matrices but the errors are tremendously high (some eigenvalues are even negative), whereas Greville’s ( $S_{n+2}$ -based) abscissae again work well but in some cases hardly fight the FEM solution.

## 6. Discussion

The global B-spline collocation method has been previously applied in the 1960s mainly in 1D elliptic problems [[de Boor 2001](#)], whereas preliminary eigenvalue analysis has been discussed by Jerome and Varga [[1969](#)]. Collocation methods have been extensively used for 2D problems but they have been implemented mostly in conjunction with small size elements; for details we refer to [[Provatidis 2009b](#)] and papers therein. For cubic B-splines, the state-of-the-art is to use two collocation points between two successive breakpoints (per direction). The latter matter is closely related to double knots (multiplicity of internal knots equal to two:  $\lambda = 2$ ), so as to produce as many equations as the number of the unknown coefficients. In contrast, Galerkin–Ritz is usually applied on the basis of multiplicity of internal knots equal to one ( $\lambda = 1$ ) [[Höllig 2003](#)] (for the sake of brevity in this study the case of double knots was not tested).

In the part of this study concerning cubic piecewise polynomials ( $p = 3$ ), we found that the B-splines based global collocation method is applicable for any multiplicity of internal knots, that is, the usual ( $\lambda = 2$ ) and the new ( $\lambda = 1$ ). For the latter case ( $\lambda = 1$ ), in which  $n_x$  subdivisions of breakpoints per direction lead to  $n_x + 3$  control points, we have initially tested to collocate at the centroids of the  $n_x$  cells defined by the breakpoints plus the ends and the middle of the domain in the corresponding direction,  $\xi$  or  $\eta$ . Although in this way we derived as many equations as the number of the coefficients, the results were not satisfactory. In contrast, when the collocation was performed taking  $2 \times 2$  (Gauss) points per cell, that is exactly the same as those used in case ( $\lambda = 2$ ), the results became of equal quality as in case ( $\lambda = 2$ ). The increased number of equations, compared to the smaller number of control points (and associated coefficients), was easily resolved applying a *least-squares* reduction of them (left-multiplication by a transpose matrix) thus producing a matrix of order equal to the number of control points.

From the study of [Example 1](#) it is concluded that the use of images of Greville ( $S_{n+2}$ -based) abscissae is a good choice when applied in conjunction with polynomials of higher degree ( $p > 3$ ). The images of Demko and Greville ( $T_n$ -based) abscissae must never be applied to Dirichlet-type eigenvalue problems in acoustics.

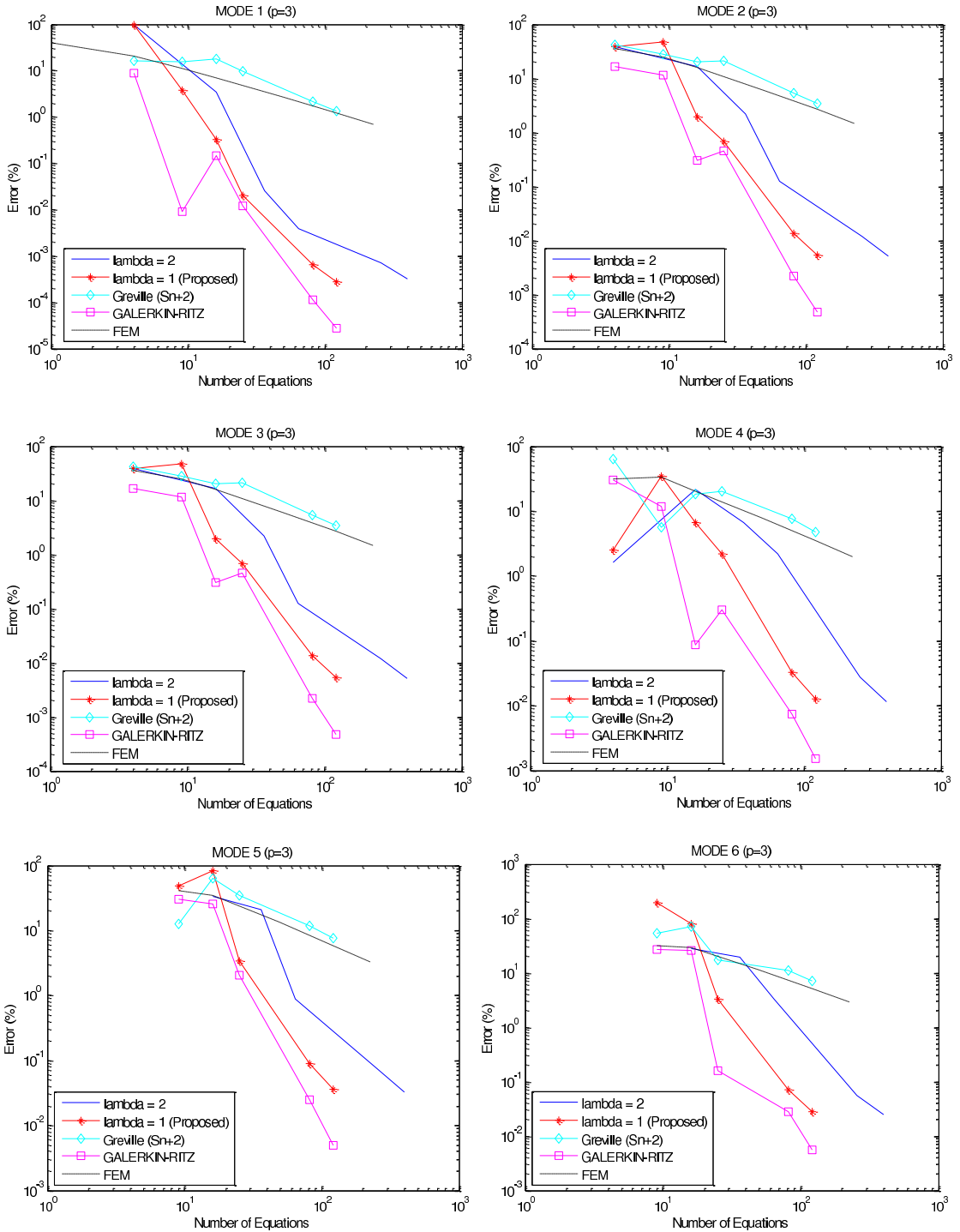


**Figure 5.** Circular cavity under *Dirichlet* boundary conditions: convergence of the first six eigenvalues in terms of number of equations, for cubic B-splines interpolation ( $p = 3$ ).

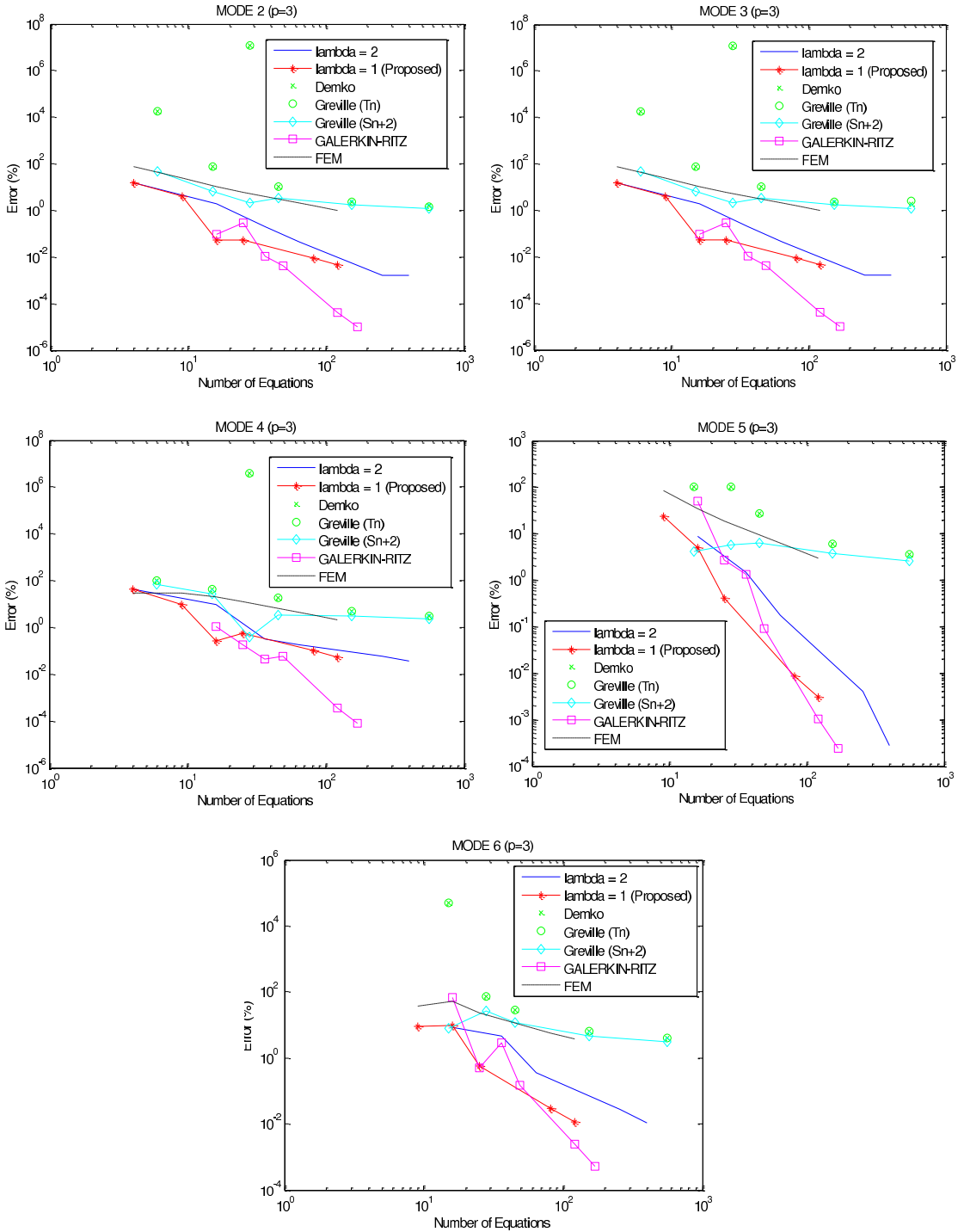


**Figure 6.** Circular cavity under *Neumann* boundary conditions: convergence of the first five nonzero eigenvalues in terms of number of equations, for cubic B-splines approximation ( $p = 3$ ).

It is worth repeating that the domain integration for calculating the matrices involved in B-splines Galerkin–Ritz method was performed in conjunction with  $4 \times 4$  (in general:  $(p + 1) \times (p + 1)$ ) Gauss points per cell of breakpoints; this is four times higher than the proposed global collocation method (independently of the multiplicity of internal knots).

Concerning the elimination of the coefficients that are associated to the boundary, in the proposed global collocation method they have to be eliminated *independently* on the type of boundary conditions. In more detail, in the case of Dirichlet boundary conditions they are simply erased whereas in the Neumann case they are properly incorporated into internal ones. In contrast, in the B-splines Galerkin–Ritz formulation, only Dirichlet-type boundary conditions require the elimination of those coefficients associated to the boundary, whereas in the free-free problem the mass and stiffness matrices remain as they are.

Concerning the two examples of this study, we make some remarks:

Example 1: Rectangular cavity. No difficulty appeared in the implementation of the proposed theory for both types of boundary conditions. Concerning the particular elimination required in the Neumann problem, the standard equation (24) is generally applicable. It was found that, for both multiplicities, it is sufficient to consider only one boundary equation at each of the four corners ( $A, B, C, D$ ), which is the derivative in either  $x$ - or  $y$ -direction. As previously mentioned at the end of Section 3.4.2, it is also possible to consider both directions but then it becomes necessary to apply a least-squares procedure so as to derive a square matrix  $\mathbf{B}_{22}$ ; in this case the results did not change at all. Moreover, for the particular case of a cubic polynomial ( $p = 3$ ) and double knots ( $\lambda = 2$ ), we can alternatively apply a more schematic procedure as shown in Appendix B.

Example 2: Circular cavity. This study reduces to cubic B-splines ( $p = 3$ ) only. Unlike the rectangular cavity, this example requires a careful programming. First of all, the determination of the circle is not a unique procedure. In all cases we have to divide the circumference into four equal parts:  $AB, BC, CD$  and  $DA$ . Then, for a given number of  $n_x$  uniform subdivisions per side using  $(n_x + 1)$  breakpoints along (e.g.,  $AB$ ), and for a given multiplicity ( $\lambda = 1$  or  $2$ ), there are either  $(n_x + 3)$  or  $2(n_x + 1)$  control points, respectively, to be determined. In all cases, the extreme control points coincide with the ends of the corresponding side (e.g.,  $AB$ ). The internal control points were determined using boundary-only Coons interpolation.

- ▷ In the case of double knots ( $\lambda = 2$ ), it was found reasonable at every breakpoint to consider the values of both the coordinates ( $x = r \cos \phi, y = r \sin \phi$ ) and the slopes ( $dx/d\phi = -r \sin \phi, dy/d\phi = r \cos \phi$ ), with  $\phi = (\pi/2)\xi, 0 \leq \xi \leq 1$ .
- ▷ In the case of single knots ( $\lambda = 1$ ), it was found sufficient to consider  $n_x + 1$  uniformly arranged internal breakpoints, that is,  $n_x + 2$  uniform segments.

Under these conditions, the following findings were noticed:

- For double knots ( $\lambda = 2$ ), the derivative at the corners becomes singular due to the vanishing Jacobian determinant. In more details, at the corner “A” it holds:  $(\partial x/\partial \xi = \partial x/\partial \eta = 0)$ . This shortcoming was resolved considering one point before and one after the corner  $A$  (for example, in the midpoints of the adjacent control points) and then taking the mean average of the normal derivatives.
- For single knots ( $\lambda = 1$ ), no difficulty was observed.

- When the internal control points were determined by smoothing the initial positions derived by boundary-only Coons interpolation, the accuracy of the numerical solution decreased.

In summary, for both examples of this study, the quality of the B-splines Galerkin–Ritz solution was the highest compared to that of the collocation schemes. Having said this, we must mention that the same quality of results had been previously received when using the well known tensor product Lagrange polynomials or Coons–Gordon transfinite interpolation (see [Provatidis 2006, p. 6702; Provatidis 2004, p. 49; Provatidis 2009a, pp. 486–492], among others). In other words, the high quality of the numerical solution is *due more to the global character* of any CAD-based interpolation (global approximation of the acoustic pressure) and less on the individual methodology (Galerkin–Ritz or collocation).

Although it was a study in depth, this article has some weaknesses that must be cured in our ongoing future research. One weak point is that the study does not focus on the bandwidth of the produced matrices (or better on the required CPU-time) but only on the number of equations per numerical scheme, a fact that may somehow influence the conclusions. A second point is that the second example (circular cavity) has to be studied again using NURBS in conjunction with higher polynomial degrees. A third point is that this paper refers only to cases where the basis functions have either maximum continuity (multiplicity of 1) or continuity reduced by one (multiplicity of  $p - 1$ ) at all internal knot lines. In the future, cases where continuity is different at different knot lines should be tested.

## 7. Conclusions

The proposed global collocation method was based on tensor product B-splines, which are also used in the Galerkin–Ritz formulation. Unlike the latter, the estimation of mass and stiffness matrices does not need any domain integral to be computed, thus reducing the computer effort. The proposed method is applicable using either single or multiple internal knots, where the maximum allowed multiplicity equals the polynomial degree minus one. In general, multiple knots are preferred as they do not require any least-squares scheme and they lead to a rather better quality. Alternatively, isogeometric collocation should be carefully applied in conjunction with single knots, particularly in problems of Dirichlet-type boundary conditions. Obviously, the extension of the proposed approach from acoustics to elastodynamics and other types of partial differential operators as well as to three-dimensional problems is straightforward.

### Appendix A: Solving boundary-value problems

The solution of the ordinary differential equation (ODE)

$$D(u(x)) = f, \quad x \in [0, L], \quad (\text{A.1})$$

by collocation is conducted as follows.

The variable is written as a B-splines series expansion

$$u(x) = \sum_{i=1}^q N_{i,p}(x) \cdot a_i, \quad (\text{A.2})$$

where  $q$  is the number of control points,  $N_{i,p}$  the basis functions, and  $a_i$  the unknown coefficients. Between alternatives, it is proposed to start with a mesh of  $(n + 1)$  discrete breakpoints (i.e.,  $n$  segments,



uniform or not). For a given polynomial degree  $p$ , considering a given standard multiplicity  $\lambda$  of all inner points (see [Piegl and Tiller 1995; de Boor 2001]), we have that

$$q = p + 1 + \lambda(n - 1). \quad (\text{A.3})$$

For reasons that will be explained below, we use  $\lambda$  collocation points per cell, that is, between any two successive breakpoints. Then the total number of collocation points becomes

$$n_{\text{col}} = \lambda n. \quad (\text{A.4})$$

The overall computational procedure is as follows:

- (1) First the ODE is fulfilled at the above-mentioned  $n_{\text{col}}$  collocation points (this procedure is identical with that used in the eigenvalue problem), which leads to the matrix equation

$$[\mathbf{A}_{\text{col}}]_{n_{\text{col}} \times q} \cdot \begin{bmatrix} a_1 \\ \vdots \\ a_q \end{bmatrix} = \begin{bmatrix} f_1 \\ \vdots \\ f_{n_{\text{col}}} \end{bmatrix}. \quad (\text{A.5})$$

- (2) Then the boundary conditions are imposed. We distinguish two cases:

- (a) Two Dirichlet-type boundary conditions:

$$x = 0 \Rightarrow a_1 = \bar{U}_0 \quad \text{and} \quad x = L \Rightarrow a_q = \bar{U}_L. \quad (\text{A.6})$$

In this case, (A.6) are substituted into (A.5), the first (with elements  $a_{i1}$ ,  $i = 1, \dots, n_{\text{col}}$ ) and last (with elements  $a_{iq}$ ,  $i = 1, \dots, n_{\text{col}}$ ) columns of matrix  $[\mathbf{A}_{\text{col}}]$  are multiplied by the known quantities  $\bar{U}_0$  and  $\bar{U}_L$  and then these terms are transferred to the right-hand-side. In this way, the dimensions of matrix  $[\mathbf{A}_{\text{col}}]$  reduce from  $n_{\text{col}} \times q$  to  $n_{\text{col}} \times (q - 2)$  and the equations system to be solved becomes

$$[\bar{\mathbf{A}}_{\text{col}}]_{n_{\text{col}} \times (q-2)} \cdot \begin{bmatrix} a_2 \\ \vdots \\ a_{q-1} \end{bmatrix} = \begin{bmatrix} f_1 - a_{11}\bar{U}_0 - a_{1q}\bar{U}_L \\ \vdots \\ f_{n_{\text{col}}} - a_{n_{\text{col},1}}\bar{U}_0 - a_{n_{\text{col},q}}\bar{U}_L \end{bmatrix}. \quad (\text{A.7})$$

In the sequence we shall seek for the conditions for which the aforementioned reduced matrix  $[\bar{\mathbf{A}}_{\text{col}}]$  becomes *square* (with equal number of rows and columns). Actually, the combination of (A.3) and (A.4) gives

$$q - 2 = \lambda n + (p - 1 - \lambda). \quad (\text{A.8})$$

Therefore, if one selects that

$$\lambda = p - 1, \quad (\text{A.9})$$

the parenthesis in (A.8) vanishes and gives that  $q - 2 = \lambda n$ , which in turn, by virtue of (A.4), gives the desired relationship  $n_{\text{col}} = (q - 2)$ , ensuring that matrix  $[\bar{\mathbf{A}}_{\text{col}}]$  is square.

- (b) One Dirichlet- and one Neumann-type boundary condition:

$$a_1 = \bar{U}_0 \quad (\text{A.10})$$

and

$$\left(\frac{\partial u}{\partial x}\right)_{x=L} = \bar{q}_L. \tag{A.11}$$

In this case, we take the first derivative of (A.2) over  $x$  and equate it with  $\bar{q}_L$  according to (A.11). Thus the number of equations is increased by one and becomes equal to  $(n_{\text{col}} + 1)$  while the first column is erased (as previously), since all relevant elements are multiplied by the known value  $\bar{U}_0$ , and is then transferred to the right hand side. Again the equations matrix is square, but in this case it is of dimensions  $(n_{\text{col}} + 1) \times (n_{\text{col}} + 1)$ .

**Remark.** Another alternative is to consider a greater number of collocation points than previously, that is  $n_{\text{col}} > \lambda n$ . In this case, after the boundary conditions are imposed the obtained matrix  $[\bar{A}_{\text{col}}]$  is *nonsquare*, of dimensions  $n_{\text{col}} \times (q - 2)$ , that is with more equations than the unknowns. The remedy to obtain a numerical solution is to apply a least-squares scheme, for example multiplying both parts of (A.7) by the transpose of matrix  $[\bar{A}_{\text{col}}]$ . However, the time-consuming transpose-matrix concept is always solved by a QR-decomposition least-squares solver (which can be found in LINPACK, LAPACK, etc.). In this way, the solution time increment is almost negligible when compared to a regular QR-decomposition for a square matrix. Nevertheless, the built up of more rows (collocation points) than necessary is the main source of increased computer time.

**Appendix B: Elimination of boundary coefficients for the free-free problem in a rectangular**

We deal with the particular case in which the polynomial degree is  $p = 3$  whereas the multiplicity of internal knots equals to *two* ( $\lambda = 2$ ). In other words, we consider *double* knots.

Let us consider a rectangle  $ABCD$  as shown in Figure 7. The opposite sides  $AB$  and  $CD$  are divided into  $n_x$  uniform subdivisions, whereas the other opposite sides ( $BC$  and  $DA$ ) are divided into  $n_y$  uniform ones. The axis origin is taken at the corner  $A$ .

In case of piecewise cubic polynomials ( $p = 3$ ) the first control point  $P_0$  coincides with the corner  $A$ , whereas  $P_{2n_x+1}$  coincides with the corner  $B$ . The second layer consists of the control points ( $P_{2(n_x+1)}$  up to  $P_{4(n_x+1)-1}$ ), and so on. Obviously, the last control point is  $P_{4(n_x+1) \times (n_y+1)-1}$ , and it coincides with

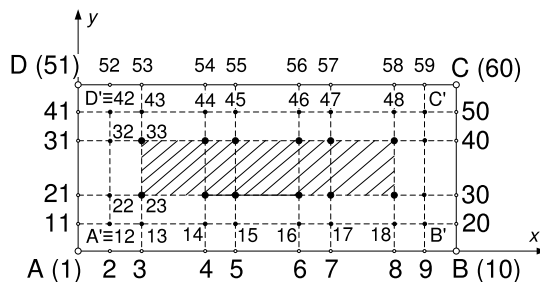


**Figure 7.** A sketch, for  $n_x \times n_y = 4 \times 2$  subdivisions and double knots ( $\lambda = 2$ ) for cubic B-splines ( $p = 3$ ), aiming at describing the procedure of eliminating the coefficients associated to the boundary control points in a rectangular  $ABCD$ . The hatched area indicates those internal control points that are not influenced by the aforementioned elimination.

the upper right corner  $C$  (Figure 7). Henceforth, for the sake of simplicity we limit the discussion for the particular case of  $n_x \times n_y = 4 \times 2$  subdivisions, where we change the numbering of the control points, starting from “1” (corner  $A$ ) and ending at “60” (corner  $C$ ).

Taking the first derivative of (13) with respect to the unit normal vector  $\mathbf{n}$  (at a point along the side  $DA$ ), we obtain

$$\frac{\partial u}{\partial \mathbf{n}} \Big|_{DA} = \sum_{k=1}^q \frac{\partial \phi_k(0, \eta)}{\partial \mathbf{n}} \cdot a_k, \quad (\text{B.1})$$

where, as already explained, it holds that

$$q = 4(n_x + 1) \times (n_y + 1). \quad (\text{B.2})$$

First, (B.1) is applied at the control point  $\mathbf{P}_0 \equiv A$ , and due to the free-free boundary conditions we obtain

$$\sum_{k=1}^q \frac{\partial \phi_k(0, 0)}{\partial x} \cdot a_k = 0. \quad (\text{B.3})$$

Due to the compact support of the basis functions  $N_{i,p}(\xi)$  and  $N_{j,p}(\eta)$ , (B.3) is written as

$$\sum_{l=1}^{2(n_x+1)} b_{lx} \cdot a_l = 0, \quad (\text{B.4})$$

with

$$b_{lx} = \frac{\partial \phi_l}{\partial x}(0, 0), \quad l = 1, \dots, 2(n_x + 1). \quad (\text{B.5})$$

Applying (B.3) at all control points along the boundary, we can obtain several relationships:

$$\text{between “1” and “2”}: b_{1x}a_1 + b_{2x}a_2 = 0. \quad (\text{B.6})$$

Equation (B.6) induces a linear relationship between the coefficients  $a_1$  and  $a_2$  associated to control points “1” and “2”, respectively.

Moreover, we can write one identical relationship between the control points “11” and “12”:

$$\text{between “11” and “12”}: b_{1x}a_{11} + b_{2x}a_{12} = 0 \Rightarrow a_{11} = -\frac{b_{2x}}{b_{1x}}a_{12}. \quad (\text{B.7})$$

In an analogous way, taking the derivatives in the  $y$ -direction, we can write:

$$\text{between “1” and “11”}: b_{1y}a_1 + b_{2y}a_{11} = 0, \quad (\text{B.8})$$

$$\text{between “2” and “12”}: b_{1y}a_2 + b_{2y}a_{12} = 0 \Rightarrow a_2 = -\frac{b_{2y}}{b_{1y}}a_{12}. \quad (\text{B.9})$$

Equations (B.6)–(B.9) impose four equations for the four variables:  $a_1$ ,  $a_2$ ,  $a_{11}$  (to be eliminated) and the  $a_{12}$  (to be kept). Therefore, it is anticipated that one of them is redundant. In fact, substituting (B.6), which is related to the derivative in the  $x$ -direction, into (B.9) one obtains the relationship between the corner “1” and the close-to-corner “12” control point as

$$a_1 = \frac{b_{2x}}{b_{1x}} \cdot \frac{b_{2y}}{b_{1y}} \cdot a_{12}. \quad (\text{B.10})$$

Obviously, the same relationship is also derived starting from the derivative at the corner “1” in the  $y$ -direction, that is, substituting (B.8) into (B.7):

$$a_1 = -\frac{b_{2y}}{b_{1y}} a_{11} = -\frac{b_{2y}}{b_{1y}} \cdot \left( -\frac{b_{2x}}{b_{1x}} \cdot a_{12} \right) = \frac{b_{2y}}{b_{1y}} \cdot \frac{b_{2x}}{b_{1x}} \cdot a_{12}. \tag{B.11}$$

The above fact (identity between (B.10) and (B.11)) depicts that it is *not* necessary to consider *both* fluxes at the corner. Therefore, we can ignore, for example, (B.8) and derive unique expression between points 11 and 12 (B.7), as well as between “2” and “12” (B.9). Moreover, the relationship between the control points “3” with “13” is similar to that between “2” and “12”. Generally, all intermediate control points along  $AB$  are slaves of the master points along the internal boundary  $A'B'$  (Figure 7). In an analogous way, we can obtain master-to-slave relations for the control points along the remaining sides  $AB$ ,  $BC$ , and  $CD$ . In this way, all control points along the boundary are slaves and are substituted by the master control points along the line  $A'B'C'D'$  shown in Figure 7.

In order to analytically perform the elimination, let us now consider an arbitrary collocation point “ $i$ ” (not shown in Figure 7). The  $i$ -th row of the matrix equation is written as

$$\begin{aligned} &(m_{i,1}\ddot{a}_1 + m_{i,2}\ddot{a}_2 + \dots + m_{i,11}\ddot{a}_{11} + m_{i,12}\ddot{a}_{12} + \dots + m_{i,60}\ddot{a}_{60}) \\ &\quad + (k_{i,1}a_1 + k_{i,2}a_2 + \dots + k_{i,11}a_{11} + k_{i,12}a_{12} + \dots + k_{i,60}a_{60}) = 0. \end{aligned} \tag{B.12}$$

In (B.12) we substitute the boundary values such as  $a_1$  using (B.10),  $a_2$  using (B.9),  $a_{11}$  using (B.7) and so on. In this way, the coefficient  $a_{12}$  appears as a factor of four terms, the coefficients  $a_{13}$  to  $a_{18}$  appear as factors of two terms, the coefficient  $a_{19}$  appears as a factor again of four terms, and so on. In more detail, after the above-mentioned substitutions equation (B.12) is written as

$$\begin{aligned} \ddot{a}_{12} &\left[ m_{i,1} \left( \frac{b_{2y}}{b_{1y}} \cdot \frac{b_{2x}}{b_{1x}} \right) + m_{i,2} \left( -\frac{b_{2y}}{b_{1y}} \right) + m_{i,11} \left( -\frac{b_{2x}}{b_{1x}} \right) + m_{i,12} \right] \\ &\quad + \ddot{a}_{13} \left[ \left( -\frac{b_{2y}}{b_{1y}} \right) m_{i,3} + m_{i,13} \right] + \dots + \ddot{a}_{18} \left[ \left( -\frac{b_{2y}}{b_{1y}} \right) m_{i,8} + m_{i,18} \right] + \dots \\ &\quad + a_{12} \left[ k_{i,1} \left( \frac{b_{2y}}{b_{1y}} \cdot \frac{b_{2x}}{b_{1x}} \right) + k_{i,2} \left( -\frac{b_{2y}}{b_{1y}} \right) + k_{i,11} \left( -\frac{b_{2x}}{b_{1x}} \right) + k_{i,12} \right] \\ &\quad + a_{13} \left[ \left( -\frac{b_{2y}}{b_{1y}} \right) k_{i,3} + k_{i,13} \right] + \dots + a_{18} \left[ \left( -\frac{b_{2y}}{b_{1y}} \right) k_{i,8} + k_{i,18} \right] + \dots = 0. \end{aligned} \tag{B.13}$$

Obviously, the implementation of (B.13) and its analogue reduces the order of each matrix from  $4(n_x + 1)(n_y + 1)$  to  $4(n_x - 1)(n_y - 1)$ .

In summary, those control points deeply in the interior (large black circles) are not influenced by the Neumann conditions and keep their columns. The remaining internal control points (small black circles) that are in the first layer parallel to the boundary are divided into two categories. The first category consists of only the four control points  $A'$ ,  $B'$ ,  $C'$ , and  $D'$  that lie in the neighborhood of the four corners; the corresponding condensed matrix elements are composed of *four* values (cf.  $a_{12}$  in (B.13)). The second category consists of those intermediate control points along the internal boundary  $A'B'C'D'$  (Figure 7); the corresponding condensed matrix elements are composed of *two* values (cf.  $a_{13}$  in (B.13)).

## References

- [Auricchio et al. 2010] F. Auricchio, L. Beirão da Veiga, T. J. R. Hughes, A. Reali, and G. Sangalli, “Isogeometric collocation methods”, *Math. Models Methods Appl. Sci.* **20**:11 (2010), 2075–2107.
- [Bézier 1971] P. E. Bézier, “Example of an existing system in the motor industry: the Unisurf system”, *Proc. R. Soc. Lond. A* **321**:1545 (1971), 207–218.
- [Bialecki et al. 2011] B. Bialecki, G. Fairweather, and A. Karageorghis, “Matrix decomposition algorithms for elliptic boundary value problems: a survey”, *Numer. Algorithms* **56**:2 (2011), 253–295.
- [de Boor 1972] C. de Boor, “On calculating with B-splines”, *J. Approx. Theory* **6** (1972), 50–62.
- [de Boor 2001] C. de Boor, *A practical guide to splines*, Revised ed., Applied Mathematical Sciences **27**, Springer, New York, 2001.
- [Cabral et al. 1990] J. J. S. P. Cabral, L. C. Wrobel, and C. A. Brebbia, “A BEM formulation using B-splines, I: Uniform blending functions”, *Eng. Anal. Bound. Elem.* **7**:3 (1990), 136–144.
- [Cabral et al. 1991] J. J. S. P. Cabral, L. C. Wrobel, and C. A. Brebbia, “A BEM formulation using B-splines, II: Multiple knots and non-uniform blending functions”, *Eng. Anal. Bound. Elem.* **8**:1 (1991), 51–55.
- [Coons 1967] S. A. Coons, “Surfaces for computer-aided design of space forms”, Technical Report MIT/LCS/TR-41, Massachusetts Institute of Technology, Cambridge, MA, June 1967, Available at <http://publications.csail.mit.edu/lcs/pubs/pdf/MIT-LCS-TR-041.pdf>.
- [Cottrell et al. 2009] J. A. Cottrell, T. J. R. Hughes, and Y. Bazilevs, *Isogeometric analysis: toward integration of CAD and FEA*, Wiley, Chichester, 2009.
- [Fairweather and Meade 1989] G. Fairweather and D. Meade, “A survey of spline collocation methods for the numerical solution of differential equations”, pp. 297–341 in *Mathematics for large scale computing*, edited by J. C. Díaz, Lecture Notes in Pure and Appl. Math. **120**, Dekker, New York, 1989.
- [Farin et al. 2002] G. Farin, J. Hoschek, and M.-S. Kim (editors), *Handbook of computer aided geometric design*, North-Holland, Amsterdam, 2002.
- [Filippatos 2010] A. Filippatos, *Derivation of eigenfrequencies in acoustic cavities and elastic structures using the global collocation method*, thesis, National Technical University of Athens, October 2010.
- [Gordon 1971] W. J. Gordon, “Blending-function methods of bivariate and multivariate interpolation and approximation”, *SIAM J. Numer. Anal.* **8** (1971), 158–177.
- [Höllig 2003] K. Höllig, *Finite element methods with B-splines*, Frontiers in Applied Mathematics **26**, Society for Industrial and Applied Mathematics, Philadelphia, 2003.
- [Hughes et al. 2010] T. J. R. Hughes, A. Reali, and G. Sangalli, “Efficient quadrature for NURBS-based isogeometric analysis”, *Comput. Methods Appl. Mech. Eng.* **199**:5-8 (2010), 301–313.
- [Jerome and Varga 1969] J. W. Jerome and R. S. Varga, “Generalizations of spline functions and applications to nonlinear boundary value and eigenvalue problems”, pp. 103–155 in *Theory and applications of spline functions* (Madison, WI, 1968), edited by T. N. E. Greville, Academic Press, New York, 1969.
- [Kwok et al. 2001] W. Y. Kwok, R. D. Moser, and J. Jiménez, “A critical evaluation of the resolution properties of B-spline and compact finite difference methods”, *J. Comput. Phys.* **174**:2 (2001), 510–551.
- [Piegl 1991] L. Piegl, “On NURBS: a survey”, *IEEE Comput. Graph. Appl.* **11**:1 (1991), 55–71.
- [Piegl and Tiller 1995] L. Piegl and W. Tiller, *The NURBS Book*, Springer, London, 1995.
- [Provatidis 2004] C. G. Provatidis, “On DR/BEM for eigenvalue analysis of 2-D acoustics”, *Comput. Mech.* **35**:1 (2004), 41–53.
- [Provatidis 2006] C. G. Provatidis, “Transient elastodynamic analysis of two-dimensional structures using Coons-patch macroelements”, *Int. J. Solids Struct.* **43**:22–23 (2006), 6688–6706.
- [Provatidis 2008a] C. G. Provatidis, “Free vibration analysis of elastic rods using global collocation”, *Arch. Appl. Mech.* **78**:4 (2008), 241–250.



- [Provatidis 2008b] C. G. Provatidis, “A global collocation method for two-dimensional rectangular domains”, *J. Mech. Mater. Struct.* **3**:1 (2008), 185–193.
- [Provatidis 2008c] C. G. Provatidis, “Time- and frequency-domain analysis using lumped mass global collocation”, *Arch. Appl. Mech.* **78**:11 (2008), 909–920.
- [Provatidis 2009a] C. G. Provatidis, “Eigenanalysis of two-dimensional acoustic cavities using transfinite interpolation”, *J. Algorithms Comput. Technol.* **3**:4 (2009), 477–502.
- [Provatidis 2009b] C. G. Provatidis, “Integration-free Coons macroelements for the solution of 2D Poisson problems”, *Int. J. Numer. Methods Eng.* **77**:4 (2009), 536–557.
- [Provatidis 2012] C. G. Provatidis, “Two-dimensional elastostatic analysis using Coons–Gordon interpolation”, *Meccanica (Milano)* **47**:4 (2012), 951–967.
- [Provatidis and Ioannou 2010] C. G. Provatidis and K. S. Ioannou, “Static analysis of two-dimensional elastic structures using global collocation”, *Arch. Appl. Mech.* **80**:4 (2010), 389–400.
- [Schoenberg 1946] I. J. Schoenberg, “Contributions to the problem of approximation of equidistant data by analytic functions, A: On the problem of smoothing or graduation. A first class of analytic approximation formulae”, *Quart. Appl. Math.* **4** (1946), 45–99. Available in *I. J. Schoenberg: selected papers*, Vol. 2, pp. 3–57, edited by C. de Boor, Birkhäuser, Boston, 1988.
- [Schoenberg and Whitney 1953] I. J. Schoenberg and A. Whitney, “On Pólya frequency functions, III: The positivity of translation determinants with an application to the interpolation problem by spline curves”, *Trans. Amer. Math. Soc.* **74** (1953), 246–259.

Received 19 Oct 2011. Revised 10 Mar 2014. Accepted 21 Mar 2014.

CHRISTOPHER G. PROVATIDIS: [cprovat@central.ntua.gr](mailto:cprovat@central.ntua.gr)

School of Mechanical Engineering, Mechanical Design and Control Systems Department, National Technical University of Athens, Heroon Polytechniou 9, Zografou Campus, 157 80 Athens, Greece



# MULTI-REGION TREFFTZ COLLOCATION GRAINS (MTCGS) FOR MODELING PIEZOELECTRIC COMPOSITE AND POROUS MATERIALS IN DIRECT AND INVERSE PROBLEMS

PETER L. BISHAY, ABDULLAH ALOTAIBI AND SATYA N. ATLURI

A simple and efficient method for modeling piezoelectric composite and porous materials to solve direct and inverse 2D problems is presented in this paper. The method is based on discretizing the problem domain into arbitrary polygonal-shaped regions that resemble the physical shapes of grains in piezoelectric polycrystalline materials, and utilizing the Trefftz solution functions derived from the Lekhnitskii formulation for piezoelectric materials, or for elastic dielectric materials, to express the mechanical and electrical fields in the interior of each grain or region. A simple collocation method is used to enforce the continuity of the inter-region primary and secondary fields, as well as the essential and natural boundary conditions. Each region may contain a void, an elastic dielectric inclusion, or a piezoelectric inclusion. The void/inclusion interface conditions are enforced using the collocation method, or using the special solution set which is available only for the case of voids (traction-free, charge-free boundary conditions). The potential functions are written in terms of Laurent series which can describe interior or exterior domains, while the negative exponents are used only in the latter case. Because Lekhnitskii's solution for piezoelectric materials breaks down if there is no coupling between mechanical and electrical variables, the paper presents this solution in a general form that can be used for coupled (piezoelectric) as well as uncoupled (elastic dielectric) materials. Hence, the matrix or the inclusion can be piezoelectric or elastic dielectric to allow modeling of different types of piezoelectric composites. The present method can be used for determining the meso/macro physical properties of these materials as well as for studying the mechanics of damage initiation at the micro level in such materials. The inverse formulation can be used for determining the primary and secondary fields over some unreachable boundaries in piezoelectric composites and devices; this enables direct numerical simulation (DNS) and health monitoring of such composites and devices. Several examples are presented to show the efficiency of the method in modeling different piezoelectric composite and porous materials in different direct and inverse problems.

## 1. Introduction and literature review

Piezoelectric composites possess some enhanced properties over monolithic piezoelectric materials that enable them to be used in different industrial applications. Bigger range of coupled properties, better acoustic properties or figures of merit, and less brittleness are among these enhanced properties. Both “subtractive” and “additive” approaches were used to develop piezoelectric composites where, in the “subtractive” approach, controlled porosity is induced in piezoelectric materials to form porous piezoelectric materials with reduced density [Li et al. 2003]. These porous piezoelectric materials found

---

Bishay is the corresponding author.

*Keywords:* piezoelectric, composites, porous, Trefftz, Lekhnitskii, Voronoi cells, void, inclusion, collocation, inverse problems.

applications such as miniature accelerometers, vibration sensors, contact microphones and hydrophones. Porous piezoelectric materials have several advantages such as lack of possibility of destructive chemical reactions between the piezoelectric ceramic and the second phase (the air) during production, ability to control pore size, shape and distribution, light weight compared to monolithic piezoelectric materials and other piezoelectric composites, reduced price of production compared to other piezoelectric composites, and low acoustic impedances compared to dense ceramics, hence they could be used to improve the mismatch of acoustic impedances at the interfaces of medical ultrasonic imaging devices or underwater sonar detectors [Kumar et al. 2006]. Porous ceramics are classified by the International Union of Pure and Applied Chemistry (IUPAC) according to their pore size (or diameter  $d$ ) as follows: macroporous ( $d > 50$  nm), meso-porous ( $2$  nm  $< d < 50$  nm), and microporous ( $d < 2$  nm). Also, they are classified according to the pore geometry [Araki and Halloran 2005] as: foam, interconnected, pore spaces between particles, plates and fibers, and large or small pore networks.

On the other hand, in the “additive” approach, the effective properties of the composite are optimized by combining two or more constituents. The second phase is used to modulate the overall properties of piezoelectric composites and could be dielectric ceramic [Jin et al. 2003], metal [Li et al. 2001], polymer [Klicker et al. 1981], or another piezoelectric material. Piezoelectric ceramics are also used in smart composite materials where piezoelectric rods (fibers) or particles are embedded in an elastic matrix.

Analytical models for porous piezoelectric materials are only available for simple geometries such as an infinite plate with circular or elliptical hole as presented in [Sosa 1991; Xu and Rajapakse 1999; Chung and Ting 1996; Lu and Williams 1998] using either the Lekhnitskii formalism [Lekhnitskii 1957] or the extended Stroh formalism [Stroh 1958]. However for more complicated geometries and practical problems, numerical methods such as finite elements, boundary elements, meshless or Trefftz methods should be used.

Modeling domains with defects (holes, inclusions or cracks) using the ordinary finite element method needs mesh refinement around defects in order to achieve acceptable results for the gradients of fields; hence it is very complex, time-consuming, and costly. Thus, special methods should be used to model defects. Special methods for direct numerical simulation (DNS) of micro/mesostructures were developed by Bishay and Atluri [2014] for porous piezoelectric materials; by Bishay et al. [2014] for piezoelectric composites; and by Dong and Atluri as 2D and 3D Trefftz cells [Dong and Atluri 2012b; 2012c; 2012d] and SGBEM cells [Dong and Atluri 2012e; 2013] for heterogeneous and functionally graded isotropic elastic materials, where each cell models an entire grain of the material, with elastic/rigid inclusions or voids, for direct numerical micromechanical analysis of composite and porous materials. Also 2D and 3D radial basis functions (RBF) grains were successfully used to model functionally graded materials (FGM) and the switching phenomena in ferroelectric materials by Bishay and Atluri [2012; 2013]. Finite elements with elliptical holes, inclusions or cracks in elastic materials were also developed by Zhang and Katsube [1995; 1997], Piltner [1985; 2008], and Wang and Qin [2012]. Hybrid-stress elements were developed by Ghosh and his coworkers (see [Moorthy and Ghosh 1996] for instance). Readers are referred to [Dong and Atluri 2012b] for a critical comparison between Ghosh’s hybrid-stress elements and the hybrid-displacement and Trefftz elements presented in the aforementioned papers. For piezoelectric materials, Wang et al. [2004] developed a hybrid finite element with a hole based on the Lekhnitskii formalism, while Cao et al. [2013] developed a hybrid finite element with defects based on the extended Stroh formalism. The boundary element method was also used by Xu and Rajapakse

[1998] to analyze piezoelectric materials with elliptical holes. In addition, Trefftz methods were used to model microstructures with defects, using multi-source-point Trefftz method in [Dong and Atluri 2012a] for plane elasticity, and Trefftz boundary collocation method for plane piezoelectricity macromechanics developed by Sheng et al. [2006] based on the Lekhnitskii formalism.

The basic idea of the various Trefftz methods is to use the so-called Trefftz functions which satisfy the homogenous governing equations of the relevant physical phenomenon as the trial and/or weight functions. A complete set of Trefftz functions that satisfy only the homogenous governing equations is termed as a *basic solution set*. A complete set of Trefftz functions that satisfy both the homogenous governing equations and the homogenous boundary conditions is termed as a *special solution set*. To formulate any Trefftz method, Trefftz functions must be available. For the case of impermeable voids, the *special solution set* that satisfies the traction-free, charge-free conditions can be used. Hence there is no need to enforce the void boundary conditions by collocation or any other method. Using the special solution set is more efficient. However, for the case of grains with pressurized voids or inclusions, the special solution set does not exist and collocation/least squares method should be used instead to enforce the void/inclusion boundary conditions.

In this paper, multi-region Trefftz collocation grains (MTCGs) are developed for modeling porous piezoelectric materials as well as piezoelectric composites where the materials of the matrix and the inclusion could be piezoelectric or elastic dielectric (anisotropic in general). The formulation is very simple and efficient since there are no simple polynomial-based elements in the finite element sense. Each grain has an arbitrarily polygonal shape to mimic the physical shape of grains in the microscale. Each grain may contain a circular or an arbitrarily oriented elliptical void or inclusion and has its own crystallographic orientation (poling direction). Each grain may be surrounded by an arbitrary number of neighboring grains; hence MTCGs are expected to show field distributions that cannot be obtained using regular triangular and four-sided polynomial-based finite elements. Dirichlet tessellation is used to construct the mesh or the geometric shapes of the grains. The formulation is also very effective in inverse problems where the boundary conditions over some portions of the problem boundary are completely unknown while on other portions extra conditions are known or measured. The Lekhnitskii formalism is employed here due to the relatively explicit nature of the derived Trefftz functions.

The paper is organized as follows: Section 2 introduces all governing equations and boundary conditions. Lekhnitskii's solution for coupled/uncoupled plane electroelastic problem is presented in Section 3 while the multi-region Trefftz collocation grains (MTCGs) formulation for piezoelectric composites with and without voids/inclusions is introduced in Section 4 for direct problems and in Section 5 for inverse problems. The advantage of using MTCGs to model representative volume element (RVE) for obtaining the overall material properties of piezoelectric composites is discussed in Section 6. Numerical examples are provided in Section 7 and conclusions are summarized in Section 8.

## 2. Governing equations and boundary conditions

Consider a domain  $\Omega$  filled with a piezoelectric composite. On the boundary of the domain, denoted  $\partial\Omega$ , we can specify displacements on  $S_u$  or tractions on  $S_t$  (not both at any point, i.e.,  $S_u \cap S_t = \emptyset$ ). Similarly we can specify electric potential on  $S_\varphi$  or electric charge per unit area (electric displacement) on  $S_Q$  (where again  $S_\varphi \cap S_Q = \emptyset$ ). So  $\partial\Omega = S_u \cup S_t = S_\varphi \cup S_Q$ . The whole domain  $\Omega$  can be divided into  $N$

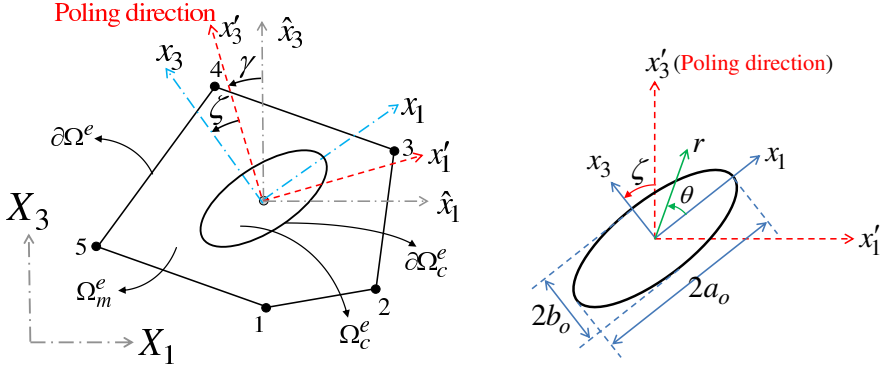


**Figure 1.** Left: 2D irregular polygon (grain) with an elliptical void/inclusion and its local coordinates ( $x_1$ - $x_3$ ) as well as the global ( $X_1$ - $X_3$ ), grain local ( $\hat{x}_1$ - $\hat{x}_3$ ) and crystallographic ( $x'_1$ - $x'_3$ ) Cartesian coordinate systems. Right: elliptical void/inclusion with the local coordinate system as well as the poling direction of the piezoelectric material.

regions  $\Omega = \sum_{e=1}^N \Omega^e$  (where each region may represent a grain in the material). The intersection of the boundary of region  $e$ , denoted  $\partial\Omega^e$ , with  $S_u$ ,  $S_t$ ,  $S_\varphi$  and  $S_Q$  is  $S_u^e$ ,  $S_t^e$ ,  $S_\varphi^e$  and  $S_Q^e$ , while the intersection with the boundaries of the neighboring regions is denoted  $S_g^e$ . Hence  $\partial\Omega^e = S_u^e \cup S_t^e \cup S_g^e = S_\varphi^e \cup S_Q^e \cup S_g^e$ .

The domain of each region,  $\Omega^e$ , may contain a void or an inclusion filling the domain  $\Omega_c^e$  and has a boundary  $\partial\Omega_c^e$  such that  $\Omega_c^e \subset \Omega^e$  and  $\partial\Omega_c^e \cap \partial\Omega^e = \emptyset$ . In this case, the region outside the void/inclusion domain in region  $e$  is called the matrix domain  $\Omega_m^e = \Omega^e - \Omega_c^e$ . Figure 1 (left) shows one grain (irregular polygonal region for the 2D case) with an arbitrarily-oriented elliptical void/inclusion. The figure also shows the crystallographic coordinates and the poling direction.

Adopting matrix and vector notation and denoting  $\mathbf{u}^\alpha$  (2 components),  $\boldsymbol{\epsilon}^\alpha$  (3 components) and  $\boldsymbol{\sigma}^\alpha$  (3 components) as the mechanical displacement vector, strain and stress tensors written in vector form respectively, and  $\varphi^\alpha$  (scalar),  $\mathbf{E}^\alpha$  (2 components) and  $\mathbf{D}^\alpha$  (2 components) as the electric potential, electric field and electric displacement vectors respectively, where the superscript  $\alpha = m$  or  $c$  (for matrix or inclusion), the following equations should be satisfied in the matrix and inclusion domains ( $\Omega_m^e$  and  $\Omega_c^e$ ):

(1) Stress equilibrium and charge conservation (Gauss's) equations:

$$\partial_u^T \boldsymbol{\sigma}^\alpha + \bar{\mathbf{b}}^\alpha = \mathbf{0}; \quad \boldsymbol{\sigma}^\alpha = (\boldsymbol{\sigma}^\alpha)^T, \quad \partial_e^T \mathbf{D}^\alpha - \bar{\rho}_f^\alpha = 0, \tag{1}$$

where  $\bar{\mathbf{b}}^\alpha$  is the body force vector, and  $\bar{\rho}_f^\alpha$  is the electric free charge density (which is approximately zero for dielectric and piezoelectric materials).

(2) Strain-displacement (for infinitesimal deformations) and electric field-electric potential relations:

$$\boldsymbol{\epsilon}^\alpha = \partial_u \mathbf{u}^\alpha, \quad \mathbf{E}^\alpha = -\partial_e \varphi^\alpha, \tag{2}$$

where

$$\partial_u = \begin{bmatrix} \partial/\partial x_1 & 0 & \partial/\partial x_3 \\ 0 & \partial/\partial x_3 & \partial/\partial x_1 \end{bmatrix}^T, \quad \partial_e = [\partial/\partial x_1 \quad \partial/\partial x_3]^T.$$

The representation of the electric field in (2), as gradients of an electric potential, includes the assumption that Faraday's equation ( $\nabla \times \mathbf{E}^\alpha = -\partial \mathbf{B}^\alpha / \partial t = \mathbf{0}$ , where  $\mathbf{B}$  is the magnetic flux density) is satisfied



for electrostatics. Note that we consider only two equations (Gauss's and Faraday's equations) from the four Maxwell's equations. The remaining two equations (Gauss's law for magnetism and Ampere's law with Maxwell's correction) are not considered in the electrostatic analysis of piezoelectric materials.

(3) Piezoelectric material constitutive laws:

$$\begin{aligned} \boldsymbol{\sigma}^\alpha &= \mathbf{C}_E^\alpha \boldsymbol{\epsilon}^\alpha - \mathbf{e}^{\alpha T} \mathbf{E}^\alpha, & \boldsymbol{\epsilon}^\alpha &= \mathbf{S}_D^\alpha \boldsymbol{\sigma}^\alpha + \mathbf{g}^{\alpha T} \mathbf{D}^\alpha, \\ \mathbf{D}^\alpha &= \mathbf{e}^\alpha \boldsymbol{\epsilon}^\alpha + \mathbf{h}_\epsilon^\alpha \mathbf{E}^\alpha, & \text{or} & \quad \mathbf{E}^\alpha &= -\mathbf{g}^\alpha \boldsymbol{\sigma}^\alpha + \boldsymbol{\beta}_\sigma^\alpha \mathbf{D}^\alpha, \end{aligned} \quad (3)$$

where  $\mathbf{C}_E^\alpha$ ,  $\mathbf{h}_\epsilon^\alpha$ ,  $\mathbf{S}_D^\alpha$ ,  $\boldsymbol{\beta}_\sigma^\alpha$  are, respectively, the elastic stiffness tensor measured under constant electric field, dielectric permittivity tensor measured under constant strain, elastic compliance tensor measured under constant electric displacement, and inverse of the dielectric permittivity tensor measured under constant stress.  $\mathbf{e}^\alpha$  and  $\mathbf{g}^\alpha$  are piezoelectric tensors measured under constant strain and stress respectively.

The SI units of the mentioned fields are as follows: stress  $\boldsymbol{\sigma}^\alpha$  (Pa or N/m<sup>2</sup>), strain  $\boldsymbol{\epsilon}^\alpha$  (m/m), electric displacement  $\mathbf{D}^\alpha$  (C/m<sup>2</sup>), electric field  $\mathbf{E}^\alpha$  (V/m or N/C), and the SI units of the material matrices are:  $\mathbf{C}_E^\alpha$  (Pa or N/m<sup>2</sup>),  $\mathbf{S}_D^\alpha$  (m<sup>2</sup>/N),  $\mathbf{h}_\epsilon^\alpha$  (C/Vm),  $\boldsymbol{\beta}_\sigma^\alpha$  (Vm/C),  $\mathbf{e}^\alpha$  (C/m<sup>2</sup>), and  $\mathbf{g}^\alpha$  (m<sup>2</sup>/C). Note that  $\mathbf{S}_D^\alpha \neq (\mathbf{C}_E^\alpha)^{-1}$  and  $\boldsymbol{\beta}_\sigma^\alpha \neq (\mathbf{h}_\epsilon^\alpha)^{-1}$ .

If the matrix or the inclusion material is elastic (not piezoelectric), then Equations (1) and (2) should be satisfied in the corresponding domains, and the coupling piezoelectric matrices  $\mathbf{e}^\alpha = \mathbf{g}^\alpha = \mathbf{0}$  in (3).

## 2.1. Matrix boundary conditions.

(1) Mechanical natural (traction) and essential (displacement) boundary conditions:

$$\begin{aligned} \mathbf{n}_\sigma \boldsymbol{\sigma}^m &= \bar{\mathbf{t}} & \text{at } S_t \text{ or } S_t^e, \\ \mathbf{u}^m &= \bar{\mathbf{u}} & \text{at } S_u \text{ or } S_u^e, \end{aligned} \quad (4)$$

(2) Electric natural and essential boundary conditions:

$$\begin{aligned} \mathbf{n}_e \mathbf{D}^m &= \bar{Q} & \text{at } S_Q \text{ or } S_Q^e, \\ \varphi^m &= \bar{\varphi} & \text{at } S_\varphi \text{ or } S_\varphi^e. \end{aligned} \quad (5)$$

where

$$\mathbf{n}_\sigma = \begin{bmatrix} n_1 & 0 & n_3 \\ 0 & n_3 & n_1 \end{bmatrix}, \quad \mathbf{n}_e = [n_1 \quad n_3], \quad (6)$$

$\bar{\mathbf{t}}$  is the specified boundary traction vector,  $\bar{Q}$  is the specified surface density of free charge.  $n_1$  and  $n_3$ , the two components present in  $\mathbf{n}_\sigma$  and  $\mathbf{n}_e$  are the components of the unit outward normal to the grain boundary  $\partial\Omega^e$ . We designate  $\bar{\mathbf{u}}$  as the specified mechanical displacement vector at the boundary  $S_u$  (or  $S_u^e$ ), and  $\bar{\varphi}$  as the specified electric potential at the boundary  $S_\varphi$  (or  $S_\varphi^e$ ).

The following conditions should also be satisfied at each (inter-region) boundary  $S_g^e$ :

(1) Mechanical displacement and electric potential compatibility conditions:

$$\begin{aligned} \mathbf{u}^{m+} &= \mathbf{u}^{m-}, \\ \varphi^{m+} &= \varphi^{m-}. \end{aligned} \quad (7)$$

(2) Mechanical traction and electric charge reciprocity conditions:

$$\begin{aligned} (\mathbf{n}_\sigma \boldsymbol{\sigma}^m)^+ + (\mathbf{n}_\sigma \boldsymbol{\sigma}^m)^- &= 0, \\ (\mathbf{n}_e \mathbf{D}^m)^+ + (\mathbf{n}_e \mathbf{D}^m)^- &= 0. \end{aligned} \tag{8}$$

**2.2. Impermeable void boundary conditions.** The dielectric constants of piezoelectric materials are three orders of magnitude higher than that of air or vacuum inside the void. This means that charges do not accumulate on the void boundary and the impermeable assumption can be adopted. We then have *traction-free, charge-free* conditions along the void boundary  $\partial\Omega_c^e$ :

$$\begin{aligned} \mathbf{t}^m &= \mathbf{n}_\sigma \boldsymbol{\sigma}^m = \mathbf{0}, \\ Q^m &= \mathbf{n}_e \mathbf{D}^m = 0. \end{aligned} \tag{9}$$

**2.3. Inclusion boundary conditions.** If the matrix and inclusion materials are elastic and nonconducting (dielectric or piezoelectric), we have the following conditions along the inclusion boundary  $\partial\Omega_c^e$ :

(1) Mechanical displacement and electric potential continuity conditions:

$$\mathbf{u}^m = \mathbf{u}^c, \quad \varphi^m = \varphi^c. \tag{10}$$

(2) Traction reciprocity and charge continuity conditions:

$$-\mathbf{n}_\sigma \boldsymbol{\sigma}^m + \mathbf{n}_\sigma \boldsymbol{\sigma}^c = 0, \quad \mathbf{n}_e \mathbf{D}^m = \mathbf{n}_e \mathbf{D}^c, \tag{11}$$

where the normal unit vector whose components,  $n_1$  and  $n_3$ , appear in  $\mathbf{n}_e$  and  $\mathbf{n}_\sigma$  (see Equation (6)) along the inclusion boundary is directed away from the inclusion domain.

These inclusion boundary conditions can be used for the case of piezoelectric particles or fibers in a nonpiezoelectric matrix (polymer, say) or in a piezoelectric matrix made up of different material. They can also be used to model elastic particles or fibers in a piezoelectric matrix.

### 3. General solution of coupled/uncoupled plane electroelasticity using Lekhnitskii’s formulation

Let  $(x'_1, x'_3)$  be the principal material (crystallographic) coordinates,  $x'_3$  be the poling direction (for piezoelectric materials) and  $(x_1, x_3)$  be the set of coordinates obtained by rotating  $(x'_1, x'_3)$  through an anti-clockwise rotation  $\zeta$  (see Figure 1, right). Using the Lekhnitskii formalism [Lekhnitskii 1977], Xu and Rajapakse [1999] derived the general solution of plane piezoelectricity with respect to  $(x_1, x_3)$  coordinate system. This formulation is generalized here to be applicable to uncoupled electromechanical problems as for the case of isotropic or transversely-isotropic elastic dielectric materials (in the isotropic case, there is no unique crystallographic coordinate system; any coordinate system can be considered as such).

The constitutive equations with respect to the crystallographic axes  $x'_1 - x'_3$  for plane stress and plane strain problems, with stress and electric displacement as objectives of the equations, can be written in compact form as:

$$\begin{Bmatrix} \boldsymbol{\epsilon}' \\ \mathbf{E}' \end{Bmatrix} = \begin{bmatrix} \mathbf{S}' & \mathbf{g}'^T \\ -\mathbf{g}' & \boldsymbol{\beta}' \end{bmatrix} \begin{Bmatrix} \boldsymbol{\sigma}' \\ \mathbf{D}' \end{Bmatrix}, \tag{12}$$

where superscripts,  $\alpha$ , in (3) that indicate whether we are talking about the matrix or the inclusion, as well as the subscripts of  $\mathbf{S}'$  and  $\boldsymbol{\beta}'$ , are omitted for simplicity.

By invoking tensor transformation rule, the constitutive relations can be written with respect to  $(x_1, x_3)$  coordinate system as:

$$\begin{Bmatrix} \epsilon_1 \\ \epsilon_3 \\ \epsilon_5 \\ E_1 \\ E_3 \end{Bmatrix} = \begin{bmatrix} S_{11} & S_{13} & S_{15} & g_{11} & g_{31} \\ S_{13} & S_{33} & S_{35} & g_{13} & g_{33} \\ S_{15} & S_{35} & S_{55} & g_{15} & g_{35} \\ -g_{11} & -g_{13} & -g_{15} & \beta_{11} & \beta_{13} \\ -g_{31} & -g_{33} & -g_{35} & \beta_{13} & \beta_{33} \end{bmatrix} \begin{Bmatrix} \sigma_1 \\ \sigma_3 \\ \sigma_5 \\ D_1 \\ D_3 \end{Bmatrix} \quad \text{or} \quad \begin{Bmatrix} \boldsymbol{\epsilon} \\ \boldsymbol{E} \end{Bmatrix} = \begin{bmatrix} \boldsymbol{S} & \boldsymbol{g}^T \\ -\boldsymbol{g} & \boldsymbol{\beta} \end{bmatrix} \begin{Bmatrix} \boldsymbol{\sigma} \\ \boldsymbol{D} \end{Bmatrix}, \quad (13)$$

in which

$$\boldsymbol{S} = \boldsymbol{T}_2^T \boldsymbol{S}' \boldsymbol{T}_2, \quad \boldsymbol{g} = \boldsymbol{T}_1^T \boldsymbol{g}' \boldsymbol{T}_2, \quad \boldsymbol{\beta} = \boldsymbol{T}_1^T \boldsymbol{\beta}' \boldsymbol{T}_1, \quad (14)$$

and in the above equations,

$$\boldsymbol{T}_1 = \begin{bmatrix} \cos \zeta & -\sin \zeta \\ \sin \zeta & \cos \zeta \end{bmatrix} \quad \text{and} \quad \boldsymbol{T}_2 = \begin{bmatrix} \cos^2 \zeta & \sin^2 \zeta & -2 \sin \zeta \cos \zeta \\ \sin^2 \zeta & \cos^2 \zeta & 2 \sin \zeta \cos \zeta \\ \sin \zeta \cos \zeta & -\sin \zeta \cos \zeta & \cos^2 \zeta - \sin^2 \zeta \end{bmatrix}.$$

It can be seen that the coefficients  $\boldsymbol{S}$ ,  $\boldsymbol{g}$  and  $\boldsymbol{\beta}$  are functions of the angular rotation  $\zeta$ . Again, for nonpiezoelectric materials, there is no coupling between the elastic and the electric fields, and  $\boldsymbol{g}' = \boldsymbol{g} = \mathbf{0}$ .

Here we summarize the expressions used to describe the primary and secondary fields in absence of body force and free-charge density ( $\bar{\boldsymbol{b}} = \mathbf{0}$ ,  $\bar{\rho}_f = 0$ ) using the Lekhnitskii formalism. For more details, the reader is referred to [Bishay and Atluri 2014; Sheng et al. 2006]. However, if the material is not piezoelectric and there is no coupling ( $g_{ij} = 0$ ), the expressions presented in the aforementioned references break down. Hence, the following expressions are modified to account for both coupled and uncoupled materials:

$$\begin{Bmatrix} u_1 \\ u_3 \\ \varphi \end{Bmatrix} = 2 \operatorname{Re} \sum_{k=1}^3 \begin{Bmatrix} p_k \\ q_k / \mu_k \\ s_k \end{Bmatrix} \omega_k(z_k), \quad (15)$$

$$\begin{Bmatrix} \sigma_1 \\ \sigma_3 \\ \sigma_5 \end{Bmatrix} = 2 \operatorname{Re} \sum_{k=1}^3 \begin{Bmatrix} \gamma_k \mu_k^2 \\ \gamma_k \\ -\gamma_k \mu_k \end{Bmatrix} \omega'_k(z_k), \quad \begin{Bmatrix} D_1 \\ D_3 \end{Bmatrix} = 2 \operatorname{Re} \sum_{k=1}^3 \begin{Bmatrix} \lambda_k \mu_k \\ -\lambda_k \end{Bmatrix} \omega'_k(z_k),$$

$$\begin{Bmatrix} \epsilon_1 \\ \epsilon_3 \\ \epsilon_5 \end{Bmatrix} = 2 \operatorname{Re} \sum_{k=1}^3 \begin{Bmatrix} p_k \\ q_k \\ r_k \end{Bmatrix} \omega'_k(z_k), \quad \begin{Bmatrix} E_1 \\ E_3 \end{Bmatrix} = -2 \operatorname{Re} \sum_{k=1}^3 \begin{Bmatrix} s_k \\ t_k \end{Bmatrix} \omega'_k(z_k), \quad (16)$$

where  $z_k = x_1 + \mu_k x_3$ ,  $\omega_k(z_k)$  are three complex potential functions, the prime denotes differentiation with respect to  $z_k$  and

$$\begin{aligned} p_k &= \gamma_k (S_{11} \mu_k^2 + S_{13} - S_{15} \mu_k) + \lambda_k (g_{11} \mu_k - g_{31}), \\ q_k &= \gamma_k (S_{13} \mu_k^2 + S_{33} - S_{35} \mu_k) + \lambda_k (g_{13} \mu_k - g_{33}), \\ r_k &= \gamma_k (S_{15} \mu_k^2 + S_{15} - S_{55} \mu_k) + \lambda_k (g_{15} \mu_k - g_{35}), \\ s_k &= \gamma_k (g_{11} \mu_k^2 + g_{13} - g_{15} \mu_k) - \lambda_k (\beta_{11} \mu_k - \beta_{31}), \\ t_k &= \gamma_k (g_{31} \mu_k^2 + g_{33} - g_{35} \mu_k) - \lambda_k (\beta_{13} \mu_k - \beta_{33}), \end{aligned}$$

$$\lambda_k = \frac{g_{11}\mu_k^3 - (g_{15} + g_{31})\mu_k^2 + (g_{13} + g_{35})\mu_k - g_{33}}{\beta_{11}\mu_k^2 - 2\beta_{13}\mu_k + \beta_{33}}, \quad \gamma_k = 1 \quad \text{for piezoelectric material,}$$

$$\lambda_k = \delta_{k3}, \quad \gamma_k = \delta_{k1} + \delta_{k2} \quad \text{for nonpiezoelectric material,}$$

where  $\delta_{ij}$  is the Kronecker delta. For piezoelectric materials,  $\mu_k$  ( $k = 1, \dots, 6$ ) are the roots of the characteristic equation

$$c_6\mu^6 + c_5\mu^5 + c_4\mu^4 + c_3\mu^3 + c_2\mu^2 + c_1\mu + c_0 = 0, \tag{17}$$

where

$$\begin{aligned} c_0 &= S_{33}\beta_{33} + g_{33}^2, \\ c_1 &= -2S_{35}\beta_{33} - 2S_{33}\beta_{13} - 2g_{33}(g_{13} + g_{35}), \\ c_2 &= S_{33}\beta_{11} + 4S_{35}\beta_{13} + \beta_{33}(2S_{13} + S_{55}) + 2g_{33}(g_{31} + g_{15}) + (g_{13} + g_{35})^2, \\ c_3 &= -2g_{11}g_{33} - 2S_{15}\beta_{33} - 2S_{35}\beta_{11} - 2\beta_{13}(2S_{13} + S_{55}) - 2(g_{31} + g_{15})(g_{13} + g_{35}), \\ c_4 &= S_{11}\beta_{33} + 4S_{15}\beta_{13} + \beta_{11}(2S_{13} + S_{55}) + 2g_{11}(g_{13} + g_{35}) + (g_{31} + g_{15})^2, \\ c_5 &= -2S_{11}\beta_{13} - 2S_{15}\beta_{11} - 2g_{11}(g_{31} + g_{15}), \\ c_6 &= S_{11}\beta_{11} + g_{11}^2, \end{aligned}$$

while for elastic dielectric materials,  $\mu_1, \mu_2, \mu_4$  and  $\mu_5$  are obtained from the elasticity equation (18), and  $\mu_3$  and  $\mu_6$  are obtained from the electrostatics equation (19):

$$S_{11}\mu^4 - 2S_{15}\mu^3 + (2S_{13} + S_{55})\mu^2 - 2S_{35}\mu^3 + S_{33} = 0, \tag{18}$$

$$\beta_{11}\mu^2 - 2\beta_{13}\mu + \beta_{33} = 0. \tag{19}$$

In general, the roots of (17) or those of (18) and (19) are complex with three conjugate pairs:

$$\mu_1 = A_{\mu 1} + iB_{\mu 1}, \quad \mu_2 = A_{\mu 2} + iB_{\mu 2}, \quad \mu_3 = A_{\mu 3} + iB_{\mu 3}, \quad \mu_4 = \bar{\mu}_1, \quad \mu_5 = \bar{\mu}_2, \quad \mu_6 = \bar{\mu}_3, \tag{20}$$

in which  $i = \sqrt{-1}$ ,  $A_{\mu k}$  and  $B_{\mu k}$  ( $k = 1, 2, 3$ ) are all distinct. Over-bar denotes complex conjugate.

**3.1. Basic solution sets.** For an elliptical void/inclusion as shown in Figure 1(right), the following conformal mapping can be used to transform an ellipse in  $z_k$ -plane into a unit circle in  $\xi_k$ -plane [Lekhnitskii 1977]:

$$\xi_k = \frac{z_k \pm \sqrt{z_k^2 - (a_o^2 + \mu_k^2 b_o^2)}}{a_o - i\mu_k b_o}, \quad k = 1, 2, 3, \tag{21}$$

where  $a_o$  and  $b_o$  are the half lengths of the void/inclusion axes as shown in Figure 1 (right) and the sign of the square root ( $\pm$ ) is chosen in such a way that  $|\xi_k| \geq 1$ . The inverse mapping has the form

$$z_k = \frac{a_o - i\mu_k b_o}{2}\xi_k + \frac{a_o + i\mu_k b_o}{2}\xi_k^{-1}, \quad k = 1, 2, 3. \tag{22}$$

Along the void/inclusion boundary which is a unit circle in the  $\xi_k$ -plane, we have  $|\xi_k| = 1$  or  $\xi_1 = \xi_2 = \xi_3 = e^{i\Theta}$  where  $\Theta \in [-\pi, \pi]$ .

The *basic set* of Trefftz functions for electromechanical displacements  $\underline{\mathbf{u}} = \{u_1, u_3, \varphi\}^T$ , electromechanical stresses and strains  $\underline{\boldsymbol{\sigma}} = \{\sigma_1 \ \sigma_3 \ \sigma_5 \ D_1 \ D_3\}^T$ ,  $\underline{\boldsymbol{\epsilon}} = \{\epsilon_1 \ \epsilon_3 \ \epsilon_5 \ E_1 \ E_3\}^T$  for interior or exterior domains, respectively, can be obtained as

$$\underline{\mathbf{u}} = 2 \sum_{n=M_s}^M \sum_{k=1}^3 \left[ (\operatorname{Re} \mathcal{D}_k \operatorname{Re} Z_k^n - \operatorname{Im} \mathcal{D}_k \operatorname{Im} Z_k^n) a_k^{(n)} - (\operatorname{Re} \mathcal{D}_k \operatorname{Im} Z_k^n + \operatorname{Im} \mathcal{D}_k \operatorname{Re} Z_k^n) b_k^{(n)} \right], \quad (23)$$

$$\underline{\boldsymbol{\sigma}} = 2 \sum_{n=M_s}^M \sum_{k=1}^3 \left[ (\operatorname{Re} \mathcal{G}_k \operatorname{Re} n Y_k^{n-1} - \operatorname{Im} \mathcal{G}_k \operatorname{Im} n Y_k^{n-1}) a_k^{(n)} - (\operatorname{Re} \mathcal{G}_k \operatorname{Im} n Y_k^{n-1} + \operatorname{Im} \mathcal{G}_k \operatorname{Re} n Y_k^{n-1}) b_k^{(n)} \right], \quad (24)$$

$$\underline{\boldsymbol{\epsilon}} = 2 \sum_{n=M_s}^M \sum_{k=1}^3 \left[ (\operatorname{Re} \mathcal{H}_k \operatorname{Re} n Y_k^{n-1} - \operatorname{Im} \mathcal{H}_k \operatorname{Im} n Y_k^{n-1}) a_k^{(n)} - (\operatorname{Re} \mathcal{H}_k \operatorname{Im} n Y_k^{n-1} + \operatorname{Im} \mathcal{H}_k \operatorname{Re} n Y_k^{n-1}) b_k^{(n)} \right]. \quad (25)$$

In the above,

$$\begin{aligned} \mathcal{D}_k &= \{p_k, q_k/\mu_k, s_k\}^T, & \mathcal{G}_k &= \{\gamma_k \mu_k^2, \gamma_k, -\gamma_k \mu_k, \lambda_k \mu_k, -\lambda_k\}^T, \\ \mathcal{H}_k &= \{p_k, q_k, r_k, -s_k, -t_k\}^T, \end{aligned}$$

and

$$\begin{aligned} M_s &= 0, & Z_k &= z_k, & Y_k^{n-1} &= z_k^{n-1} && \text{for simply connected domains,} \\ M_s &= 0, & Z_k &= \xi_k, & Y_k^{n-1} &= \xi_k^{n-1} && \text{for ellipse-interior domains,} \\ M_s &= -M, & Z_k &= \xi_k, & Y_k^{n-1} &= \frac{\xi_k^{n-1}}{A - B \xi_k^{-2}} && \text{for ellipse-exterior domains,} \end{aligned}$$

where  $A = \frac{1}{2}(a_o - i \mu_k b_o)$ ,  $B = \frac{1}{2}(a_o + i \mu_k b_o)$ .

For interior/exterior solutions, when  $M$  is increased by one, six/twelve Trefftz functions with their corresponding undetermined real coefficients  $\{a_1^{(\pm n)}, b_1^{(\pm n)}, a_2^{(\pm n)}, b_2^{(\pm n)}, a_3^{(\pm n)}, b_3^{(\pm n)}\}$  are added to the solution. So the number of Trefftz functions  $m_T$  (which is also equivalent to the number of undetermined real coefficients) is:

$$m_T = \begin{cases} 6(M+1) & \text{for interior domain solution,} \\ 6(2M+1) & \text{for exterior domain solution.} \end{cases} \quad (26)$$

Because of the exponential growth of the term  $Z_k^n$  as  $n$  is increased, we introduce a characteristic length to scale the Trefftz solution set in order to prevent the system of equations from being ill-conditioned. For an arbitrary polygonal grain as shown in [Figure 1](#) (left), where the coordinates of the nodes are  $(x_1^j, x_3^j)$ ,  $j = 1, 2, \dots, m$ , the center point of the polygon has coordinates  $(x_1^c, x_3^c)$ . Relative to the local coordinates at the center point, we have  $\hat{z}_k = \hat{x}_1 + \mu_k \hat{x}_3 = (x_1 - x_1^c) + \mu_k (x_3 - x_3^c)$ ,  $k = 1, 2, 3$  and correspondingly,

$$\hat{\xi}_k = \frac{\hat{z}_k \pm \sqrt{\hat{z}_k^2 - (a_o^2 + \mu_k^2 b_o^2)}}{a_o - i \mu_k b_o}.$$

Now,  $Z_k$  ( $z_k$  for interior domains or  $\xi_k$  for exterior domains) will be replaced by  $\hat{Z}_k/R_c$  where

$$R_c = \max(R_{ck}), \quad R_{ck} = \max_j \sqrt{[\operatorname{Re} \hat{Z}_k^j]^2 + [\operatorname{Im} \hat{Z}_k^j]^2}, \quad j = 1, 2, \dots, m. \quad (27)$$

This is done only for terms with positive exponents. In this way, the exponential growth of  $Z_k^n$  is prevented as  $n$  is increased because  $0 < |(\hat{Z}_k/R_c)^n| < 1$  for any point within the grain or along the grain boundaries.

**3.2. Special solution set for impermeable elliptical voids.** Trefftz special solution set accounts for the homogeneous boundary conditions of voids, cracks, etc. Wang et al. [2004] constructed a special solution set of Trefftz functions for elliptical voids with axes parallel/perpendicular to poling direction. Sheng et al. [2006] extended this to the case of arbitrarily oriented impermeable elliptical voids.

By enforcing traction-free, charge-free boundary conditions along the void surface, we can express  $a_k^{(-n)}$  and  $b_k^{(-n)}$  in terms of  $a_k^{(n)}$  and  $b_k^{(n)}$ , as (see [Stroh 1958])

$$a_k^{(-n)} = \sum_{j=1}^3 (\text{Re}(E_{kj})a_j^{(n)} - \text{Im}(E_{kj})b_j^{(n)}), \quad b_k^{(-n)} = - \sum_{j=1}^3 (\text{Im}(E_{kj})a_j^{(n)} + \text{Re}(E_{kj})b_j^{(n)}), \quad (28)$$

where

$$\begin{bmatrix} E_{11} & E_{12} & E_{13} \\ E_{21} & E_{22} & E_{23} \\ E_{31} & E_{32} & E_{33} \end{bmatrix} = - \begin{bmatrix} \gamma_1 & \gamma_2 & \gamma_3 \\ \gamma_1 \bar{\mu}_1 & \gamma_2 \bar{\mu}_2 & \gamma_3 \bar{\mu}_3 \\ \bar{\lambda}_1 & \bar{\lambda}_2 & \bar{\lambda}_3 \end{bmatrix}^{-1} \begin{bmatrix} \gamma_1 & \gamma_2 & \gamma_3 \\ \gamma_1 \mu_1 & \gamma_2 \mu_2 & \gamma_3 \mu_3 \\ \lambda_1 & \lambda_2 & \lambda_3 \end{bmatrix}.$$

So the number of Trefftz functions  $m_T$  (which is also equivalent to the number of undetermined real coefficients) is reduced to  $m_T = 6(M + 1)$ .

Substituting (28) into (23)–(25) yields the following *special set* of Trefftz functions:

$$\begin{aligned} \underline{u}_{\text{void}} &= \sum_{n=0}^M \sum_{k=1}^3 (\Phi_{a_k}^{(n)} a_k^{(n)} + \Phi_{b_k}^{(n)} b_k^{(n)}), \\ \underline{\sigma}_{\text{void}} &= \sum_{n=0}^M \sum_{k=1}^3 (\Psi_{a_k}^{(n)} a_k^{(n)} + \Psi_{b_k}^{(n)} b_k^{(n)}), \\ \underline{\epsilon}_{\text{void}} &= \sum_{n=0}^M \sum_{k=1}^3 (\Gamma_{a_k}^{(n)} a_k^{(n)} + \Gamma_{b_k}^{(n)} b_k^{(n)}), \end{aligned} \quad (29)$$

where

$$\begin{aligned} \Phi_{a_k}^{(n)} &= \chi_{a_k}^{(n)} + \sum_{j=1}^3 (\text{Re}(E_{jk})\chi_{a_j}^{(-n)} - \text{Im}(E_{jk})\chi_{b_j}^{(-n)}), \quad \Phi_{b_k}^{(n)} = \chi_{b_k}^{(n)} - \sum_{j=1}^3 (\text{Im}(E_{jk})\chi_{a_j}^{(-n)} + \text{Re}(E_{jk})\chi_{b_j}^{(-n)}), \\ \Psi_{a_k}^{(n)} &= \Sigma_{a_k}^{(n)} + \sum_{j=1}^3 (\text{Re}(E_{jk})\Sigma_{a_j}^{(-n)} - \text{Im}(E_{jk})\Sigma_{b_j}^{(-n)}), \quad \Psi_{b_k}^{(n)} = \Sigma_{b_k}^{(n)} - \sum_{j=1}^3 (\text{Im}(E_{jk})\Sigma_{a_j}^{(-n)} + \text{Re}(E_{jk})\Sigma_{b_j}^{(-n)}), \\ \Gamma_{a_k}^{(n)} &= \Upsilon_{a_k}^{(n)} + \sum_{j=1}^3 (\text{Re}(E_{jk})\Upsilon_{a_j}^{(-n)} - \text{Im}(E_{jk})\Upsilon_{b_j}^{(-n)}), \quad \Gamma_{b_k}^{(n)} = \Upsilon_{b_k}^{(n)} - \sum_{j=1}^3 (\text{Im}(E_{jk})\Upsilon_{a_j}^{(-n)} + \text{Re}(E_{jk})\Upsilon_{b_j}^{(-n)}), \end{aligned} \quad (30)$$

and in (30):

$$\begin{aligned} \chi_{a_k}^{(\pm n)} &= 2 \text{Re } \mathcal{D}_k \text{ Re } \xi_k^{\pm n} - 2 \text{Im } \mathcal{D}_k \text{ Im } \xi_k^{\pm n}, \\ \chi_{b_k}^{(\pm n)} &= -2 \text{Re } \mathcal{D}_k \text{ Im } \xi_k^{\pm n} - 2 \text{Im } \mathcal{D}_k \text{ Re } \xi_k^{\pm n}, \end{aligned}$$



$$\begin{aligned}\Sigma_{a_k}^{(\pm n)} &= \pm 2n \left( \operatorname{Re} \mathcal{G}_k \operatorname{Re} \frac{\xi_k^{\pm n-1}}{z'_k} - \operatorname{Im} \mathcal{G}_k \operatorname{Im} \frac{\xi_k^{\pm n-1}}{z'_k} \right), \\ \Sigma_{b_k}^{(\pm n)} &= \mp 2n \left( \operatorname{Re} \mathcal{G}_k \operatorname{Im} \frac{\xi_k^{\pm n-1}}{z'_k} + \operatorname{Im} \mathcal{G}_k \operatorname{Re} \frac{\xi_k^{\pm n-1}}{z'_k} \right), \\ \Upsilon_{a_k}^{(\pm n)} &= \pm 2n \left( \operatorname{Re} \mathcal{H}_k \operatorname{Re} \frac{\xi_k^{\pm n-1}}{z'_k} - \operatorname{Im} \mathcal{H}_k \operatorname{Im} \frac{\xi_k^{\pm n-1}}{z'_k} \right), \\ \Upsilon_{b_k}^{(\pm n)} &= \mp 2n \left( \operatorname{Re} \mathcal{H}_k \operatorname{Im} \frac{\xi_k^{\pm n-1}}{z'_k} + \operatorname{Im} \mathcal{H}_k \operatorname{Re} \frac{\xi_k^{\pm n-1}}{z'_k} \right).\end{aligned}$$

#### 4. Multi-region Trefftz collocation grain (MTCGs) formulation for direct problems

Consider a 2D irregular  $m$ -sided polygonal grain with/without void/inclusion as shown in [Figure 1](#) (left). The basic solution set in Equations (23)–(25) can be used as the interior/exterior fields, which satisfy the constitutive law, the strain-displacement relationship, the electric field-electric potential relationship and the equilibrium and Maxwell's equations. For the case of impermeable elliptical voids, the special solution set in Equations (29) which additionally satisfies the void stress-free charge-free boundary conditions can be used instead. In matrix and vector notation, these interior/exterior fields in  $\Omega^e$  when  $\alpha = m$ , and in  $\Omega_c^e$  when  $\alpha = c$ , can be written in the form

$$\begin{Bmatrix} \mathbf{u}^\alpha \\ \varphi^\alpha \end{Bmatrix} = \begin{Bmatrix} N_u^\alpha \\ N_\varphi^\alpha \end{Bmatrix} \mathbf{c}^\alpha, \quad \begin{Bmatrix} \boldsymbol{\sigma}^\alpha \\ D^\alpha \end{Bmatrix} = \begin{Bmatrix} M_\sigma^\alpha \\ M_D^\alpha \end{Bmatrix} \mathbf{c}^\alpha, \quad (31)$$

or

$$\underline{\mathbf{u}}^\alpha = N^\alpha \mathbf{c}^\alpha, \quad \underline{\boldsymbol{\sigma}}^\alpha = M^\alpha \mathbf{c}^\alpha,$$

where  $N^\alpha$  are the Trefftz functions in the order of  $M_s, \dots, 0, 1, \dots, M$  and  $\mathbf{c}^\alpha$  denotes the unknown real coefficients ( $a_k^{(\pm n)}, b_k^{(\pm n)}$ ,  $k = 1, 2, 3$  and  $n = M_s, \dots, M$ ) associated with Trefftz functions. If there is no void/inclusion, only the nonnegative exponents are used in the basic solution set.

The tractions and density of free charge on the boundaries  $\partial\Omega^e$  when  $\alpha = m$ , and  $\partial\Omega_c^e$  when  $\alpha = c$ , can be written as

$$\mathbf{t}^\alpha = n_\sigma \boldsymbol{\sigma}^\alpha = n_\sigma M_\sigma^\alpha \mathbf{c}^\alpha, \quad Q = n_e D^\alpha = n_e M_D^\alpha \mathbf{c}^\alpha,$$

or

$$\underline{\mathbf{t}}^\alpha = \begin{Bmatrix} \mathbf{t}^\alpha \\ Q \end{Bmatrix} = \begin{bmatrix} n_\sigma & \mathbf{0} \\ \mathbf{0} & n_e \end{bmatrix} \begin{Bmatrix} \boldsymbol{\sigma}^\alpha \\ D^\alpha \end{Bmatrix} = \underline{n} \boldsymbol{\sigma}^\alpha = \underline{n} M^\alpha \mathbf{c}^\alpha. \quad (32)$$

Now the following conditions should be enforced:

- (1) Continuities of primal fields (electromechanical displacements), in (7), as well as reciprocity conditions, in (8), at all boundaries,  $S_g^e$ , between a grain and its neighboring grains, if any.
- (2) Essential boundary conditions (in (4) and (5)) if prescribed on boundaries  $S_u^e$  and  $S_\varphi^e$ ,
- (3) Natural boundary conditions ((4) and (5)) if prescribed on boundaries  $S_t^e$  and  $S_Q^e$ .
- (4) Void/inclusion interface conditions as mentioned in [Section 2](#) (when an inclusion is present in the grain or when a void is present in the grain and the basic solution set is to be used).

In this work, we use the simple collocation/least squares method to enforce all these conditions. Galerkin method can also be used and may yield a slightly better accuracy, but it is more susceptible to round-off errors [Sheng et al. 2006] as compared to the straightforward collocation method. When the void/inclusion boundary  $\partial\Omega_c^e$  shrinks to zero, the grain is reduced to the case of a grain with no void/inclusion.

For the case of an impermeable void, using the special solution set, which already satisfies the void traction-free charge-free boundary conditions, is clearly more efficient than using the basic set because there is no need to enforce any conditions on the void boundary, however if the void is pressurized, filled with conducting fluid or replaced by any type of inclusions, the basic set should be used as mentioned earlier (there is no special solution set in this case).

The first three of the aforementioned conditions are enforced in a strong sense at several preselected collocation points along the grain boundary  $\partial\Omega^e$ .  $n_c$  points,  $(\mathbf{x}^{(r)}, r = 1, 2, \dots, n_c)$ , are selected along each side of the grain's outer boundary. Also when using the basic solution set, (Equations (23)–(25)), void/inclusion boundary conditions are enforced by dividing the void/inclusion periphery into a number of curved segments,  $n_s$ , along the void/inclusion boundary  $\partial\Omega_c^e = \sum_{j=1}^{n_s} \partial\Omega_{c_j}^e$ , and enforcing the boundary conditions on each segment, or on the center point of each segment. So,

- (1) Continuity of electromechanical displacements and reciprocity of electromechanical tractions along  $S_g^{ab}$ , the boundary side that separates any two neighboring grains  $a$  and  $b$ :

$$\begin{aligned} \underline{\mathbf{u}}^{m(\Omega^a)}(\mathbf{x}^{(r)}, \mathbf{c}_a^m) - \underline{\mathbf{u}}^{m(\Omega^b)}(\mathbf{x}^{(r)}, \mathbf{c}_b^m) &= \mathbf{0}, & \mathbf{x}^{(r)} \in S_g^{ab}, & r = 1, 2, \dots, n_c, \\ \underline{\mathbf{t}}^{m(\Omega^a)}(\mathbf{x}^{(r)}, \mathbf{c}_a^m) + \underline{\mathbf{t}}^{m(\Omega^b)}(\mathbf{x}^{(r)}, \mathbf{c}_b^m) &= \mathbf{0}, & \mathbf{x}^{(r)} \in S_g^{ab}, & r = 1, 2, \dots, n_c. \end{aligned} \quad (33)$$

- (2) Essential boundary conditions along the boundaries  $S_u^e$  and  $S_\varphi^e$  in grain  $e$ :

$$\begin{aligned} \underline{\mathbf{u}}^m(\mathbf{x}^{(r)}, \mathbf{c}_e^m) &= \bar{\mathbf{u}}, & \mathbf{x}^{(r)} \in S_u^e, & r = 1, 2, \dots, n_c, \\ \underline{\varphi}^m(\mathbf{x}^{(r)}, \mathbf{c}_e^m) &= \bar{\varphi}, & \mathbf{x}^{(r)} \in S_\varphi^e, & r = 1, 2, \dots, n_c. \end{aligned} \quad (34)$$

- (3) Natural boundary conditions along the boundaries  $S_t^e$  and  $S_Q^e$  in grain  $e$ :

$$\begin{aligned} \underline{\mathbf{t}}^m(\mathbf{x}^{(r)}, \mathbf{c}_e^m) &= \bar{\mathbf{t}}, & \mathbf{x}^{(r)} \in S_t^e, & r = 1, 2, \dots, n_c, \\ \underline{Q}^m(\mathbf{x}^{(r)}, \mathbf{c}_e^m) &= \bar{Q}, & \mathbf{x}^{(r)} \in S_Q^e, & r = 1, 2, \dots, n_c. \end{aligned} \quad (35)$$

- (4) Void/inclusion interface conditions along  $\partial\Omega_c^e$  (when using the basic solution set):

- (a) Impermeable void: traction-free and charge-free conditions along  $\partial\Omega_c^e$ :

$$\int_{\partial\Omega_{c_j}^e} \underline{\mathbf{t}}^m(\mathbf{x}, \mathbf{c}_e^m) ds = 0, \quad j = 1, 2, \dots, n_s. \quad (36)$$

- (b) Inclusion: primal fields' continuity, traction reciprocity and charge-continuity conditions along  $\partial\Omega_c^e$ :

$$\begin{aligned} \underline{\mathbf{u}}^m(\mathbf{x}^{(j)}, \mathbf{c}_e^m) - \underline{\mathbf{u}}^c(\mathbf{x}^{(j)}, \mathbf{c}_e^c) &= \mathbf{0}, & j &= 1, 2, \dots, n_s, \\ \underline{\mathbf{t}}^m(\mathbf{x}^{(j)}, \mathbf{c}_e^m) + \underline{\mathbf{t}}^c(\mathbf{x}^{(j)}, \mathbf{c}_e^c) &= \mathbf{0}, & j &= 1, 2, \dots, n_s. \end{aligned} \quad (37)$$

Combining all these conditions for  $N$  grains in a matrix/vector form leads to

$$\mathbf{A}\mathbf{c} = \mathbf{b} \quad \text{or} \quad \mathbf{c} = \mathbf{A}^{-1}\mathbf{b}, \quad (38)$$

where  $\mathbf{c}$  is a column matrix containing the unknown coefficients of the matrix and inclusion of all grains. The length of the vector  $\mathbf{c}$  can be expressed as

$$N_T = \sum_{e=1}^N ((m_T)_e + (m_{Tc})_e), \quad (39)$$

where  $(m_T)_e$  is the number of Trefftz functions in the matrix of grain  $e$ , and  $(m_{Tc})_e$  is the number of Trefftz functions in the inclusion of grain  $e$  (if applicable). These numbers depend on  $M$ , the highest order of  $Z_k$  in (23)–(25) or (29), used in the matrix and inclusion of each grain. In this study, we use the following (according to (26)):

$M = 4$  (for matrix of a grain with void or inclusion):

$$(m_T)_e = 6(2M + 1) = 54 \text{ (basic solution set, ellipse-exterior domain)}$$

$M = 4$  (for inclusions):

$$(m_{Tc})_e = 6(M + 1) = 30 \text{ (basic solution set, ellipse-interior domain)}$$

$M = 2$  (for matrix of a grain with impermeable void):

$$(m_T)_e = 6(M + 1) = 18 \text{ (special solution set).}$$

Since we are collocating six variables at each collocation point on each of the inner boundaries (boundaries shared by any two neighboring grains), and three variables at each collocation point on each of the outer boundaries (grain boundaries on the outer frame of the domain), the number of collocation equations can be expressed as:

$$N_E = n_c(6N_i + 3N_o) + \sum_{e=1}^N p_e(n_s)_e, \quad (40)$$

where  $N_i$  is the number of inner grain boundaries (sides) in the whole domain,  $N_o$  is the number of outer grain boundaries (sides) in the whole domain, and  $(n_s)_e$  is the number of segments used to divide the void periphery in grain  $e$  (only if the basic solution set is used) or the number of collocation points along the inclusion periphery in grain  $e$ , and  $p_e = 0$  if we are using the special solution set,  $p_e = 3$  if grain  $e$  contains a void and the basic solution set is used, while  $p_e = 6$  if grain  $e$  contains an inclusion.

In order for the system of equations (38) to be solved, we need  $N_T \leq N_E$ . In the last three examples we present in Section 7, we use two uniformly distributed collocation points on each side of the outer boundary of each grain ( $n_c = 2$ ) and 16 points or segments on the void/inclusion boundary in each grain ( $(n_s)_e = 16$ ). This ensures that the number of equations is larger than the number of unknowns; hence the system is over-constrained and is solved using singular value decomposition (SVD). The SVD method can solve even the singular system of equations and produces the least squares solutions to the over-constrained systems. The distribution of collocation points along each side of a grain's outer boundary could be selected as the Gaussian points [Bishay and Atluri 2012]. However this makes no significant difference in the solution.

## 5. Multi-region Trefftz collocation grain (MTCG) formulation for inverse problems with regularization

If both electromechanical displacements and tractions are specified or known only on a part of the problem boundary, the inverse problem is to determine the electromechanical displacements and tractions in the domain as well as the other part of the boundary where everything is unknown. The same can be said if “tractions” is replaced by “strains” in the previous sentence. One example is in health monitoring of piezoelectric composites and devices when data are known or measured on the outer boundaries, but not available at the inaccessible cavities in the domain.

Now let  $S_c^e$  be a part of the boundary of grain  $e$  (outer boundaries for a grain containing an inclusion, and both inner and outer boundaries for a grain with a void) where electromechanical displacements and tractions (or strains) are known. We use the available data and select enough collocation points ( $\mathbf{x}^{(p)} \in S_c^e$ ,  $p = 1, 2, \dots, P$ ) along  $S_c^e$  to get

$$\mathbf{u}^m(\mathbf{x}^{(p)}, \mathbf{c}_e^m) = \bar{\mathbf{u}}, \quad \varphi^m(\mathbf{x}^{(p)}, \mathbf{c}_e^m) = \bar{\varphi}, \quad p = 1, 2, \dots, P, \quad (41)$$

and

$$\mathbf{t}^m(\mathbf{x}^{(p)}, \mathbf{c}_e^m) = \bar{\mathbf{t}}, \quad Q^m(\mathbf{x}^{(p)}, \mathbf{c}_e^m) = \bar{Q}, \quad p = 1, 2, \dots, P, \quad (42)$$

or

$$\boldsymbol{\epsilon}^m(\mathbf{x}^{(p)}, \mathbf{c}_e^m) = \bar{\boldsymbol{\epsilon}}, \quad \mathbf{E}^m(\mathbf{x}^{(p)}, \mathbf{c}_e^m) = \bar{\mathbf{E}}, \quad p = 1, 2, \dots, P. \quad (43)$$

Combining (41) and (42) or (43) in addition to the continuity of electromechanical displacements and reciprocity of electromechanical tractions along  $S_g^{ab}$  in (33), and the inclusion boundary conditions in (37) for grains with inclusions, represent the measured or known data in all grains. This can be written in matrix form as

$$\mathbf{A}_I \mathbf{c}_I = \mathbf{b}_I. \quad (44)$$

This equation cannot be solved directly using the least squares method because the system of equations in inverse problems is known to be ill-posed and generally very-sensitive to perturbation in the measurement data on the boundary  $S_c^e$ . Hence, regularization techniques should be used to mitigate this ill-posedness. There are several regularization methods that were used in the literature, among which are the truncated singular value decomposition (TSVD), selective singular value decomposition (SSVD), and the Tikhonov regularization [Hansen 1994; Tikhonov and Arsenin 1974]. In this work, TSVD method was used and the regularization parameter is obtained using the generalized cross-validation (GCV) method. For details about the aforementioned methods, the reader is referred to [Hansen 1994].

This formulation is generally suitable for any selection of  $S_c^e$ . For a plate with a hole modeled with only one region ( $N = e = 1$ ), for instance,  $S_c$  could be all or part of the outer boundary where all measurements can be taken.

## 6. On using representative volume element (RVE) to predict the effective material properties of piezoelectric composites

In order to determine the overall properties of piezoelectric composites from known properties of their constituents (matrix and particles or fibers), two approaches were used in the literature: macromechanical

and micromechanical. In the macromechanical approach, the heterogeneous structure of the composite is replaced by a homogeneous medium with anisotropic properties, while in the micromechanical approach, a periodic RVE or a unit cell model is used to obtain the global properties of the composite [Berger et al. 2006]. A unit cell is the smallest part that contains sufficient information on the geometrical and material parameters at the microscopic level to allow for prediction of the effective properties of the composite. The numerical methods, such as the finite elements, are well-suited to model the RVE and to describe the behavior of these composite materials because there are no restrictions on the geometry, the material properties, the number of phases, and the size of the composite constituents. When employing unit cell models, the local fields in the constituent phases can be accurately determined by the numerical method, and various mechanisms such as damage initiation and propagation can be studied through the analysis. Numerical homogenization method is based on finding a globally homogeneous medium equivalent to the original composite, where the strain energy stored in both systems is approximately the same. In order to do so, first, a representative volume element which captures the overall behavior of a composite structure is created. Then the effective material properties are calculated by applying periodic boundary conditions and appropriate load cases, which are connected to specific deformation patterns, to the unit cell [Kari et al. 2008].

It is known that the advantages of the analytical approaches over the FE analyses are their ability to model statistical distributions of fibers/particles in the composite, and their low computational time, while the FE analysis, in contrast, is appropriate for estimating the effective properties of composites with a given periodic fiber/particle distribution and more complicated geometries (different shapes of fibers' cross-section, more than two phases, etc.), and at the same time, the local fields can be obtained accurately. Berger et al. [2006] found that in order to get sufficiently accurate results from the FE model, the mesh density should be chosen in such a way that the average element width is at least 5% of the unit cell width. This means that at least 400 two-dimensional regular elements are required to accurately model a two-dimensional unit cell that includes only one fiber or particle. Finite element results are sensitive to mesh density; hence it could be a difficult task to find appropriate meshes for the RVE [Berger et al. 2005]. The disadvantages of the numerical models can be avoided if we resort to the newly developed techniques such as those presented in this article and in [Bishay and Atluri 2014; Bishay et al. 2014; Dong and Atluri 2012a; 2012b; 2012c; 2012d] because these advanced methods can model a grain with its inclusion using only one element or region whose geometric shape is arbitrary, hence any statistical random distribution of fibers or particles can be accounted for with relatively very small computational cost and with high resolution in local fields' calculation.

In Section 7.4, we show the ability of MTCGs method to predict the effective material properties of a piezoelectric composite using only one region, while in Section 7.5, we show the ability of the proposed method to model random distributions of the second phase, and to obtain high resolution of local fields that enables studying damage initiation mechanisms in the microlevel.

## 7. Numerical examples

The formulation described above is programmed using Matlab in a 64-bit Windows operating system, and executed on a PC computer equipped with Intel Q8300 2.5 GHz CPU, and 8 GB RAM. The material properties of the materials used in the examples in this section are listed in Table 1.

Property	$C_{11}$	$C_{12}$	$C_{13}$	$C_{22}$	$C_{23}$	$C_{33}$	$C_{44}$	$C_{55}$
PZT-4	139	77.8	74.3	139	74.3	113	25.3	25.3
PZT-7A	148	76.2	74.2	148	74.2	131	25.4	25.4
LaRC-SI	8.1	5.4	5.4	8.1	5.4	8.1	1.4	1.4
Property	$C_{66}$	$e_{31}$	$e_{32}$	$e_{33}$	$e_{15}$	$h_{11}$	$h_{22}$	$h_{33}$
PZT-4	30.6	-6.98	-6.98	13.84	13.44	6	6	5.47
PZT-7A	35.9	460	460	235	9.2	-2.1	-2.1	9.5
LaRC-SI	1.4	0	0	0	0	2.8	2.8	2.8

**Table 1.** Material properties used in the numerical examples:  $C_{ij}$  in GPa,  $e_{ij}$  in C/m<sup>2</sup>,  $h_{ii}$  in pC/(Vm).

Simple problems that use grains with no voids or inclusions, such as patch test and bending of a piezoelectric panel, can be easily and accurately modeled using any number of grains (with no voids or inclusions) to mesh the problem domain, and the error in the whole structure is less than 1%. Patch test with any number of grains containing inclusions having the same material properties as that of the matrix can also be passed with error less than 1%.

In the following, we show some numerical examples using the proposed MTCGs. In the first example we present inverse problem where the electromechanical displacements and tractions are all measured with white noise on the outer boundary of a piezoelectric domain with an impermeable elliptical void under mechanical loading, and the variables on the unreachable void surface are predicted. Then we study the convergence of this inverse problem as the accessible part on the outer boundary of the domain shrinks. The problem of a piezoelectric inclusion in an infinite piezoelectric matrix is then studied. This is followed by evaluation of material properties of a piezoelectric particulate composite material as functions of particle volume fraction. Finally we present contour plots that detect damage-prone sites in porous piezoelectric material samples with arbitrary elliptical voids. Comparisons with other analytical and computational results are presented whenever possible.

**7.1. Piezoelectric panel with impermeable void: inverse problem.** Consider a piezoelectric panel with an arbitrarily oriented elliptical void whose semi-axes are  $a$  and  $b$  and the inclination angle between the elliptical void minor axis and the poling direction is  $\zeta$  as shown in Figure 2 (left). The local coordinate system of the ellipse is denoted  $x_1$ - $x_3$ , while the global coordinate system is denoted  $X_1$ - $X_3$ . The poling direction is aligned with the global vertical  $X_3$  axis (shown in blue in the figure). The material is PZT-4 whose properties are presented in Table 1 (taken from [Xu and Rajapakse 1999]) and plane strain assumption is used in this problem. Now consider that the electromechanical displacements and tractions are all measured at the outer boundary and that there is some white noise in the measurements. The inverse problem is to use these available measurements to predict the electromechanical tractions and displacements at the inner cavity. In this example, we use the analytical solution presented in [Xu and Rajapakse 1999] for an elliptical void in an infinite piezoelectric panel as the prescribed (or measured) data on the outer boundary after adding certain level of white noise. Mechanical load  $\sigma_o = 1$  Pa is applied on the panel's upper and lower edges. In this example we take  $L = W = 6a$ ,  $b/a = 0.6$ ,  $\zeta = 0$ ,  $M = 4$

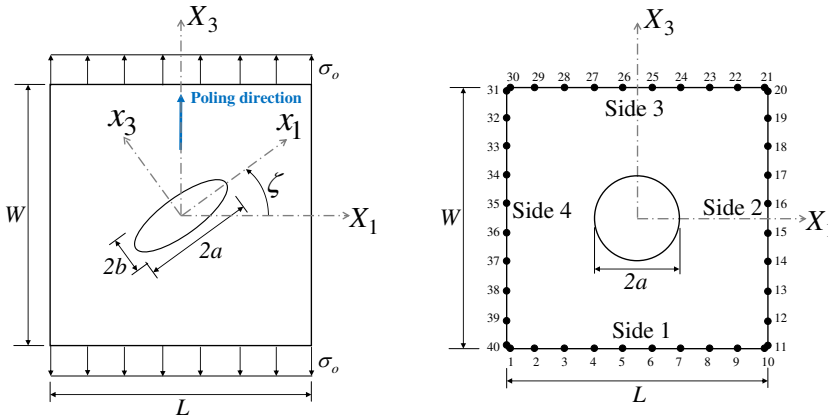


**Figure 2.** Left: a finite rectangular domain with arbitrarily oriented elliptical void. Right: collocation points considered in Section 7.2.

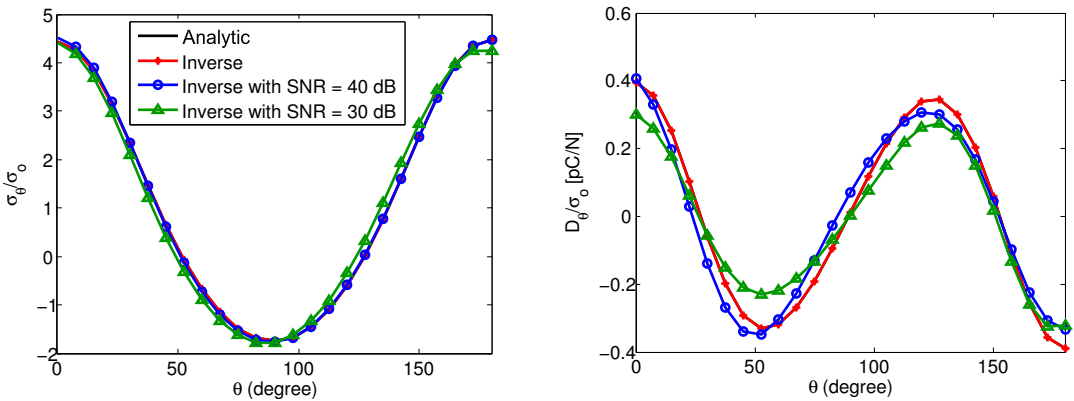


**Figure 3.** Variations of  $\sigma_\theta/\sigma_o$  (left),  $D_\theta/\sigma_o$  (right) along the periphery of an elliptical void.

(equivalent to 54 unknown coefficients) and we use 3 collocation points per side (giving 72 collocation equations). Hence, in this case  $S_c$ , mentioned in Section 5, is all the outer boundary of the plate where all data are measured.

Figure 3 and Figure 4 show the computed circumferential distributions of  $\sigma_\theta$ ,  $D_\theta$ ,  $E_\theta$  and  $E_r$  divided by  $\sigma_o$  obtained from the solution of the inverse problem with different levels of white noise added to the measured electromechanical displacements and tractions. The figures show that when there is no noise present, this approach can always exactly reproduce the electromechanical tractions in the domain. When white noise of 40 dB and 30 dB signal-to-noise ratio (SNR), which is equivalent to 1% and 3.3% amplitude of noise in the measurements, is added, only limited error is obtained in the predicted stress, electric displacement and electric field on the void periphery.

The effects of varying  $\zeta$ ,  $a/b$  and  $W/a$  ratios on the stress, electric displacement and electric field are presented in [Xu and Rajapakse 1998].



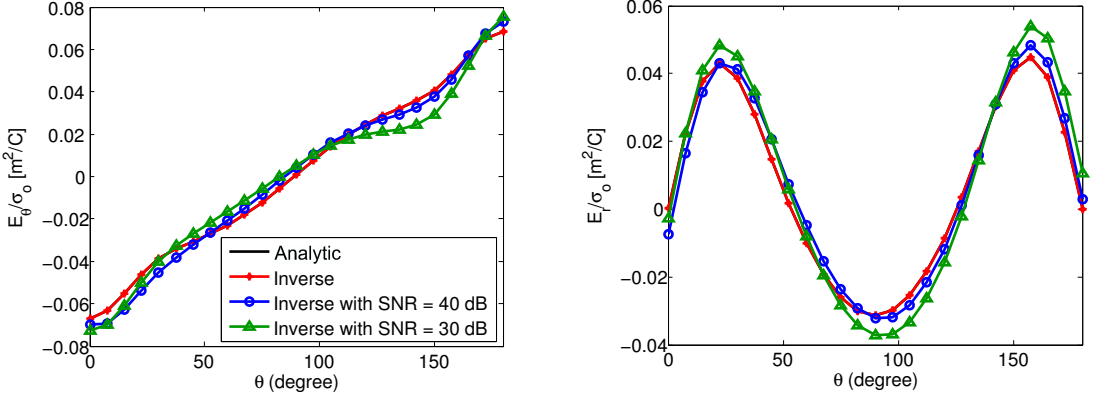


**Figure 4.** Variations of  $E_\theta/\sigma_o$  (left),  $E_r/\sigma_o$  (right) along the periphery of an elliptical void.

**7.2. Convergence study for the inverse problem.** In this study, the same problem presented in Section 7.1 is considered again when the outer boundary is not fully accessible. Hence we rely on measurements taken from only a limited part of the outer boundary. Ten collocation points are used along each side of the outer boundary as shown in Figure 2 (right) and we keep removing collocation equations corresponding to these points from side 2 first (starting from point 11 in the figure) followed by side 3, then side 4. Every time we remove two points, we solve the problem and calculate the discrete extreme mechanical and electrical errors, expressed as

$$E_{\text{mech}} = \max_{\mathbf{x}_r \in \partial\Omega_c} \left( \frac{|\sigma_\theta(\mathbf{x}_r) - \tilde{\sigma}_\theta(\mathbf{x}_r)|}{\tilde{\sigma}_{\text{max}}} \right), \quad E_{\text{elect}} = \max_{\mathbf{x}_r \in \partial\Omega_c} \left( \frac{|D_\theta(\mathbf{x}_r) - \tilde{D}_\theta(\mathbf{x}_r)|}{\tilde{D}_{\text{max}}} \right), \quad (45)$$

where  $\tilde{\sigma}_\theta(\mathbf{x}_r)$  and  $\tilde{D}_\theta(\mathbf{x}_r)$  are the exact solutions at boundary points  $\mathbf{x}_r$  along the periphery of the void;  $\tilde{\sigma}_{\text{max}}$  and  $\tilde{D}_{\text{max}}$  are respectively the maximum magnitudes of  $\tilde{\sigma}_\theta(\mathbf{x}_r)$  and  $\tilde{D}_\theta(\mathbf{x}_r)$ .

It was found that when there is no noise in the prescribed (measured) data, only nine points (equivalent to 54 collocation equations, which is equal to the number of unknown coefficients when  $M = 4$  is used) are required to get accurate results with  $E_{\text{mech}}$  and  $E_{\text{elect}}$  less than 0.001. These nine points could be prescribed on only a small part (quarter) of side 1 only, side 3 only, or on both sides 2 and 4 such that at least one point is on one of these two sides and the remaining points are on the other side. However when there is a white noise in the prescribed (measured) data, errors increase as we remove more points (or take our measurements from only a limited part of the outer boundary). The mechanical and electrical discrete extreme errors are presented in Table 2, when white noise of 40 dB signal-to-noise ratio (SNR) is added to the prescribed data, as more points are removed from the collocation points in Figure 2. It is clear from the table that the errors increase as more collocation points are removed from the outer boundary. When all collocation points on side 2 are not used, we get  $E_{\text{mech}} \approx 3\%$ , and  $E_{\text{elect}} \approx 12\%$ . When all collocation points on both side 2 and side 3 are not used, we get  $E_{\text{mech}} \approx 17.5\%$ , and  $E_{\text{elect}} \approx 51\%$ . Removing additional points from side 4, results in highly increasing  $E_{\text{elect}}$ .

It should be noted that the numbers in Table 2 change slightly every time we change the added random white noise. In addition, errors increase as the noise level increases.

Points removed	None	11–12	11–14	11–16	11–18	11–20	11–22
$E_{\text{mech}}$	0.0045	0.0106	0.0177	0.0225	0.0260	0.0297	0.0392
$E_{\text{elect}}$	0.0117	0.0525	0.0642	0.1030	0.1133	0.1207	0.1570
Points removed	11–24	11–26	11–28	11–30	11–32	11–34	11–36
$E_{\text{mech}}$	0.0423	0.0875	0.1004	0.1753	0.2807	0.4458	1.9738
$E_{\text{elect}}$	0.2393	0.2825	0.3373	0.5123	2.1058	5.4703	8.0255

**Table 2.** Discrete extreme mechanical and electrical errors as more collocation points are removed from the outer boundary (white noise of 40 dB SNR is added to the prescribed data on the outer boundary).

**7.3. Infinite piezoelectric domain with elliptical inclusion.** Consider an infinite piezoelectric plane with an elliptical inclusion subjected to vertical mechanical loading in the far field. For numerical implementations, the infinite domain is truncated into a rectangle with length  $L$  and width  $W$ , as shown in Figure 2 (left) with  $\zeta = 0$ ,  $L = W = 6a$ , and  $\sigma_o = 1$  Pa. The matrix material is PZT-4 whose properties are presented in Table 1 and plane strain assumption is used. The properties of the inclusion are given as:

$$\begin{bmatrix} \mathbf{C}_E^c & -\mathbf{e}^{cT} \\ \mathbf{e}^c & \mathbf{h}_\epsilon^c \end{bmatrix} = \Gamma \begin{bmatrix} \mathbf{C}_E^m & -\mathbf{e}^{mT} \\ \mathbf{e}^m & \mathbf{h}_\epsilon^m \end{bmatrix}, \quad (46)$$

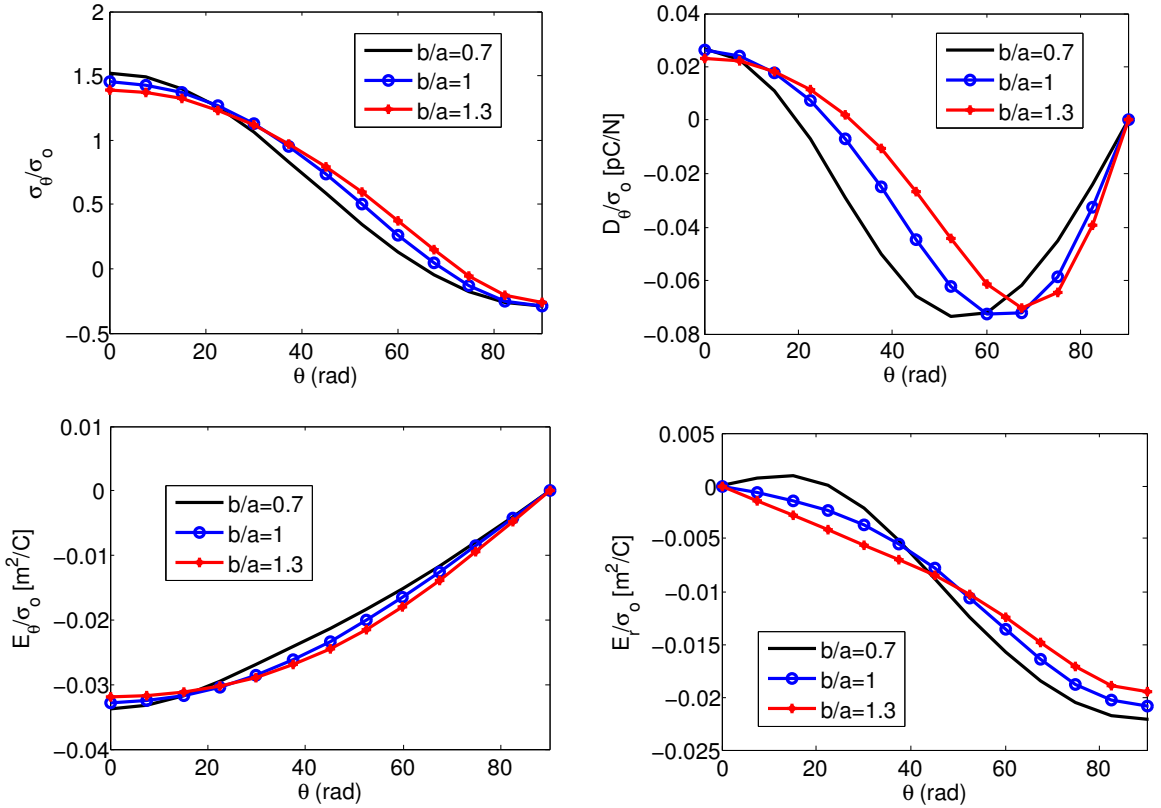
where  $\Gamma$  is a factor that can be varied.  $\Gamma > 1$  is equivalent to an inclusion material with stronger properties than those of the matrix material (larger stiffness, dielectric and piezoelectric material constants), while  $\Gamma < 1$  is equivalent to an inclusion with weaker properties.

Figure 5 shows the effect of  $b/a$  on  $\sigma_\theta/\sigma_o$ ,  $D_\theta/\sigma_o$ ,  $E_\theta/\sigma_o$  and  $E_r/\sigma_o$  along the inclusion periphery with  $\Gamma = 0.5$ .

It can be seen from the figure that controlling the shape of the inclusions can result in varying the distribution and the maximum absolute values of the circumferential stress and electric displacement, as well as the circumferential and radial electric field, along the inclusion periphery. The effect of varying  $\Gamma$  on the aforementioned variables along the inclusion periphery is presented in [Bishay et al. 2014].

**7.4. Evaluation of material properties of piezoelectric composites.** Our 2D models can be used to estimate all effective material properties of composites with particles or voids, while for composites with fibers, only effective properties in the plane perpendicular to the fiber axis can be obtained. In this example, we determine the material properties of PZT-7A/LaRC-SI piezoelectric composite (PZT-7A piezoelectric particles embedded in LaRC-SI polyimide matrix) as functions of particle volume fraction. PZT-7A is a ceramic that exhibits the piezoelectric effect with electric fields applied along all three principle axes. LaRC-SI is a thermoplastic polyimide that was developed for aerospace applications. The material properties of all constituents are listed in Table 1 (taken from [Odegard 2004]).

In order to calculate the effective material properties, computational models that ensure the presence of  $\epsilon_{11}$ ,  $\epsilon_{33}$ ,  $E_1$  or  $E_3$  alone in each model should be used. This is done by prescribing constant mechanical displacement or electric potential on the right or upper sides of the sample while enforcing zero electromechanical displacements on the other three sides. For more details about these computational models and how to calculate the effective material properties, the readers are referred to [Bishay and



**Figure 5.** Effect of  $b/a$  on  $\sigma_\theta/\sigma_o$  (top left),  $D_\theta/\sigma_o$  (top right),  $E_\theta/\sigma_o$  (bottom left) and  $E_r/\sigma_o$  (bottom right) along the inclusion periphery.

Atluri 2014]. Here we just present the results. The three Young's moduli  $Y_1$ ,  $Y_2$  and  $Y_3$  can be obtained from the stiffness matrix constants  $C_{ij}$ .

The RVE used is composed of just one region (grain) that includes an inclusion. Plane strain assumption is used in this study and the direction of polarization is vertically upward.

Figure 6 shows the predictions of the different effective material constants as functions of particle volume fraction and compared with Mori–Tanaka (MT), self-consistent (SC), finite element models using ANSYS (with large number of elements) and Odegard's proposed analytical model, all presented in [Odegard 2004].

It can be seen that, using only one MTCG, the proposed model gives very accurate predictions as compared to those of Mori–Tanaka's model. It is known that the self-consistent model deviates from Mori–Tanaka's model and gives unrealistic predictions as the volume fraction increases. The proposed method is much more computationally efficient as well as numerically more accurate than the simple finite element models (FEM) using ANSYS, and can be used to model piezo-composites even if the arrangement of particles is not symmetrical which is the main assumption used in all the previously mentioned analytical models.

**7.5. Damage detection in porous piezoelectric materials with arbitrary oriented elliptical voids.** We consider a porous piezoelectric RVE made of 20 PZT-4 piezoelectric grains with arbitrary sized elliptical

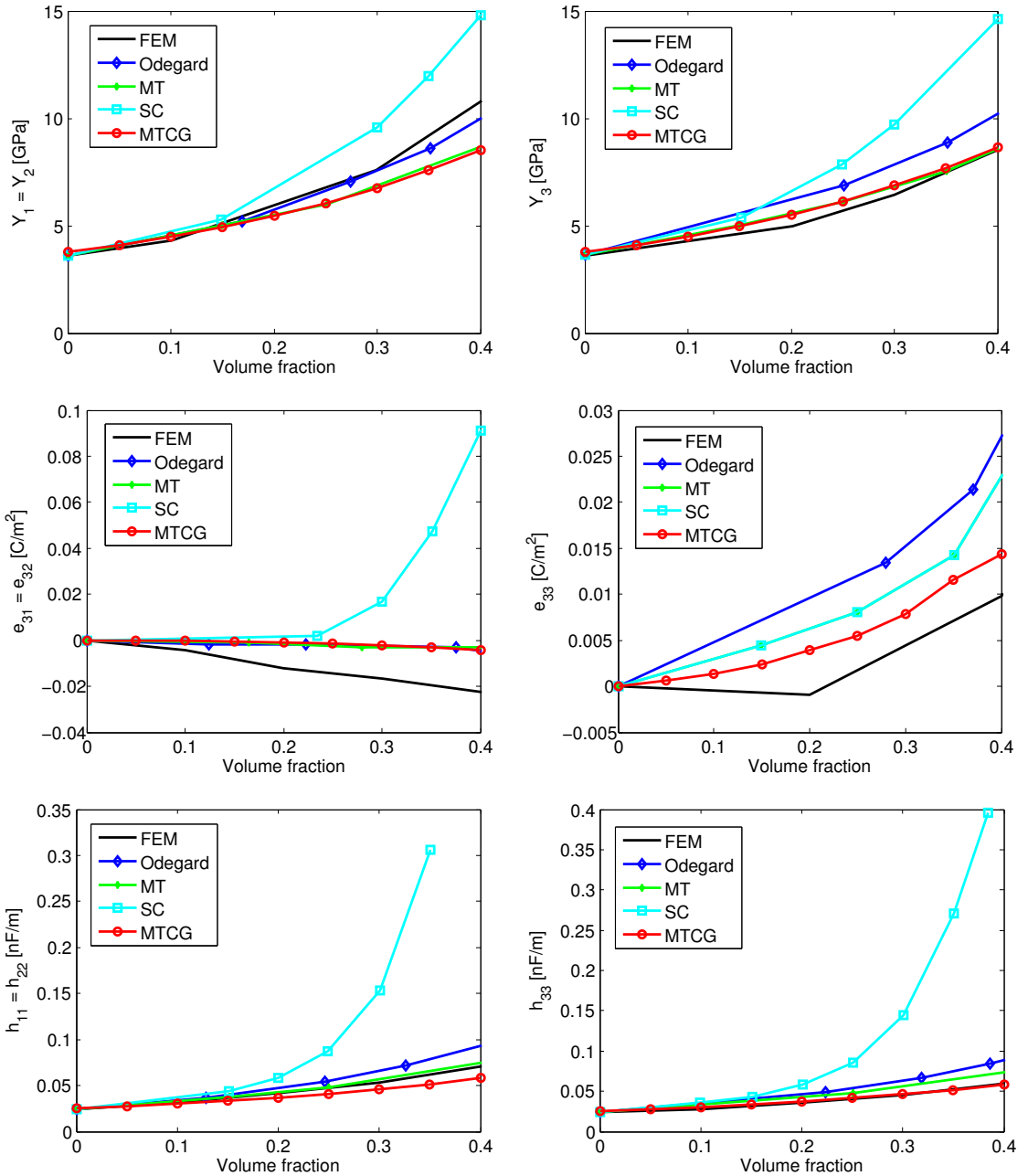


**Figure 6.** Predictions of effective piezoelectric material properties of PZT-7A/LaRC-SI as functions of particle volume fraction.

voids whose  $b/a$  ratios are in the range of 0.7–1.3. The dimensions of the RVE are  $L = W = 1$  mm and the porosity volume fraction is 0.05. The direction of polarization is vertically upward in all grains. The lower edge is prevented from motion in the vertical direction while the lower left corner node is electrically grounded and constrained in the horizontal direction. A mechanical loading  $\sigma_o = 1$  GPa is

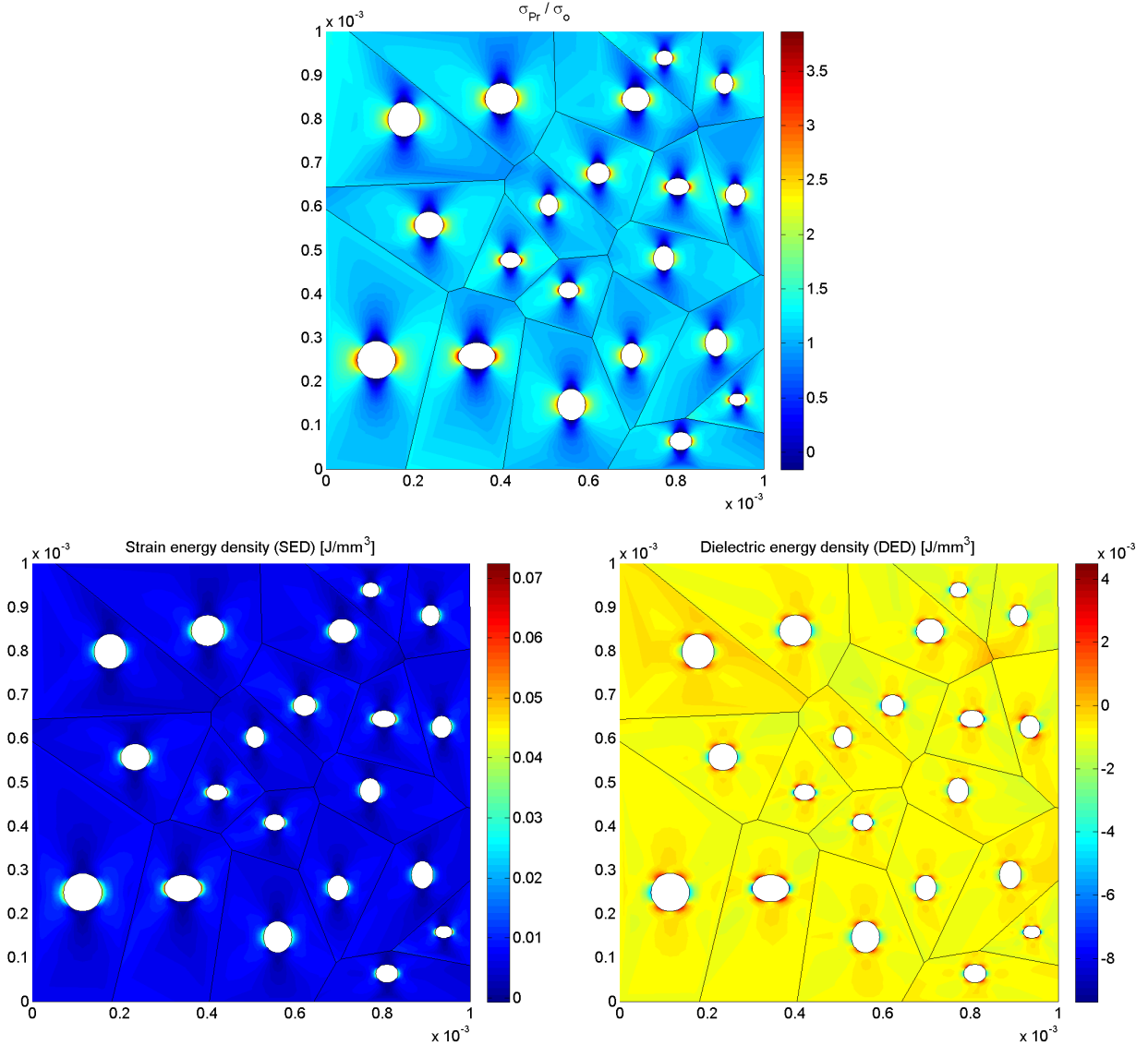


**Figure 7.** Porous piezoelectric material under mechanical loading: contour plot for principal stress (upper), strain energy density (lower left), and dielectric energy density (lower right).

applied on the upper edge. Contour plots of maximum principal stress, strain energy density (SED), as well as dielectric energy density are shown in [Figure 7](#).

As can be seen from the figures, high principal stress and strain energy density concentrations are observed near the cavities, in the direction perpendicular to the loading direction. On the other hand, at the locations near the voids, in the direction parallel to the loading direction, low stress and strain energy density values are observed. Higher stress and strain energy density concentrations can be observed around voids that have lower values of  $b/a$  (because these voids are sharper and are approaching the

shapes of cracks). This gives us an idea about where damage is more likely to initiate and develop in porous piezoelectric materials. It is also interesting to note that the dielectric energy concentrates around the voids at angles  $\pm 45^\circ$  from the mechanical loading direction, and decreases around the voids in the direction perpendicular to the loading direction.

In this example there are 44 inner grain boundaries and 17 outer grain boundaries. Since the special solution set is used, the number of collocation equations, according to (40), is  $6 \times 44 \times 2 + 3 \times 17 \times 2 = 630$ , while the number of unknowns, according to (39), is  $20 \times 18 = 360$ . Solving the same problem using a finite element analysis software like COMSOL Multiphysics and using regular triangular elements of “normal” size to mesh the problem domain generates 10,163 elements corresponding to 5,360 nodes and 16,080 degrees of freedom. COMSOL has nine levels of element sizes named: extremely coarse, extra coarse, coarser, coarse, normal, fine, finer, extra fine and extremely fine. Refining the mesh by selecting smaller element sizes in order to refine the results will definitely increase the number of nodes and the size of the FE system of equations to be solved. If voids are replaced by inclusions, according to Equations (39) and (40), the number of unknowns will be 1,680 and the number of equations will be 2,550. Solving it using COMSOL requires 12,189 regular elements of “normal” size corresponding to 6,153 nodes and 18,459 degrees of freedom. This is the case for a domain with only 20 voids/inclusions. If it is required to analyze a domain with 200, 2000 or more grains with voids/inclusions in a direct numerical simulation (DNS), the regular finite element method would be highly expensive and impractical as compared to the MTCGs method and the newly developed methods presented in [Bishay and Atluri 2014; Bishay et al. 2014; Dong and Atluri 2012b; 2012c; 2012d].

## 8. Summary and conclusions

The Lekhnitskii formalism is presented here for the general plane electromechanical problems that can be applied to coupled (piezoelectric) or uncoupled (elastic) materials. Multi-region Trefftz computational grains (MTCGs) method is proposed based on this formalism to model different porous and composite piezoelectric materials in the micro and meso scales where each computational grain has an irregular polygonal shape that resembles the shape of a material grain with arbitrary number of sides and neighboring grains. Each grain also may contain a circular or an arbitrary oriented elliptical void or inclusion, and may have its own direction of polarization. Collocation method is used to enforce the electromechanical natural and essential boundary conditions, continuity and reciprocity conditions along grain boundaries, and void/inclusion interface conditions. Applications of the proposed method include: (1) solving inverse problems by predicting the electromechanical stress at some unreachable locations in structures (like voids) using all the available or measured data even with noise (regularization methods should be used); (2) determining the effective material properties of different piezoelectric composites; (3) optimizing the material properties of piezoelectric composites by controlling the microstructure parameters (shapes of voids/inclusions, orientations, spatial distributions, material properties, etc.); and (4) obtaining the distribution of all secondary fields and the strain and dielectric energy densities in the microstructure to predict locations of damage.

## Acknowledgements

This work was funded by the Deanship of Scientific Research (DSR), King Abdulaziz University, under grant number (3-130-35-HiCi). The authors, therefore, acknowledge the technical and financial support of KAU. This research is also supported in part by the Mechanics Section, Vehicle Technology Division, of the US Army Research Labs, under a collaborative research agreement with UCI. The encouragement of Dy Le and Jaret Riddick is thankfully acknowledged.

## References

- [Araki and Halloran 2005] K. Araki and J. W. Halloran, “[Porous ceramic with interconnected pore channels by a novel freeze casting technique](#)”, *J. Am. Ceram. Soc.* **88**:5 (2005), 1108–1114.
- [Berger et al. 2005] H. Berger, S. Kari, U. Gabbert, R. Rodriguez-Ramos, R. Guinovart-Díaz, J. A. Otero, and J. Bravo-Castillero, “[An analytical and numerical approach for calculating effective material coefficients of piezoelectric fiber composites](#)”, *Int. J. Solids Struct.* **42** (2005), 5692–5714.
- [Berger et al. 2006] H. Berger, S. Kari, U. Gabbert, R. Rodriguez-Ramos, J. Bravo-Castillero, R. Guinovart-Díaz, F. J. Sabina, and G. A. Maugin, “[Unit cell models of piezoelectric fiber composites for numerical and analytical calculation of effective properties](#)”, *Smart Mater. Struct.* **15** (2006), 451–458.
- [Bishay and Atluri 2012] P. L. Bishay and S. N. Atluri, “[High-performance 3D hybrid/mixed, and simple 3D Voronoi cell finite elements, for macro- & micro-mechanical modeling of solids, without using multi-field variational principles](#)”, *Comput. Model. Eng. Sci.* **84**:1 (2012), 41–97.
- [Bishay and Atluri 2013] P. L. Bishay and S. N. Atluri, “[2D and 3D multiphysics Voronoi cells, based on radial basis functions, for direct mesoscale numerical simulation \(DMNS\) of the switching phenomena in ferroelectric polycrystalline materials](#)”, *Comput. Mater. Continua* **33**:1 (2013), 19–62.
- [Bishay and Atluri 2014] P. L. Bishay and S. N. Atluri, “[Trefftz–Lekhnitski grains \(TLGs\) for efficient direct numerical simulation \(DNS\) of the micro/meso mechanics of porous piezoelectric materials](#)”, *Comput. Mater. Sci.* **83** (2014), 235–249.
- [Bishay et al. 2014] P. L. Bishay, L. Dong, and S. N. Atluri, “[Multi-physics computational grains \(MPCGs\) for direct numerical simulation \(DNS\) of piezoelectric composite/porous materials and structures](#)”, *Comput. Mech.* (2014). Accepted for publication.
- [Cao et al. 2013] C. Cao, A. Yu, and Q.-H. Qin, “[A new hybrid finite element approach for plane piezoelectricity with defects](#)”, *Acta Mech.* **224**:1 (2013), 41–61.
- [Chung and Ting 1996] M. Y. Chung and T. C. T. Ting, “[Piezoelectric solid with an elliptic inclusion or hole](#)”, *Int. J. Solids Struct.* **33**:23 (1996), 3343–3361.
- [Dong and Atluri 2012a] L. Dong and S. N. Atluri, “[A simple multi-source-point Trefftz method for solving direct/inverse SHM problems of plane elasticity in arbitrary multiply-connected domains](#)”, *Comput. Model. Eng. Sci.* **85**:1 (2012), 1–43.
- [Dong and Atluri 2012b] L. Dong and S. N. Atluri, “[T-Trefftz Voronoi cell finite elements with elastic/rigid inclusions or voids for micromechanical analysis of composite and porous materials](#)”, *Comput. Model. Eng. Sci.* **83**:2 (2012), 183–220.
- [Dong and Atluri 2012c] L. Dong and S. N. Atluri, “[Development of 3D T-Trefftz Voronoi cell finite elements with/without spherical voids &/or elastic/rigid inclusions for micromechanical modeling of heterogeneous materials](#)”, *Comput. Mater. Continua* **29**:2 (2012), 169–211.
- [Dong and Atluri 2012d] L. Dong and S. N. Atluri, “[Development of 3D Trefftz Voronoi cells with ellipsoidal voids &/or elastic/rigid inclusions for micromechanical modeling of heterogeneous materials](#)”, *Comput. Mater. Continua* **30**:1 (2012), 39–82.
- [Dong and Atluri 2012e] L. Dong and S. N. Atluri, “[SGBEM \(using non-hyper-singular traction BIE\), and super elements, for non-collinear fatigue-growth analyses of cracks in stiffened panels with composite-patch repairs](#)”, *Comput. Model. Eng. Sci.* **89**:5 (2012), 417–458.



- [Dong and Atluri 2013] L. Dong and S. N. Atluri, “SGBEM Voronoi cells (SVCs), with embedded arbitrary-shaped inclusions, voids, and/or cracks, for micromechanical modeling of heterogeneous materials”, *Comput. Mater. Continua* **33**:2 (2013), 111–154.
- [Hansen 1994] P. C. Hansen, “Regularization tools: a Matlab package for analysis and solution of discrete ill-posed problems”, *Numer. Algorithms* **6**:1-2 (1994), 1–35.
- [Jin et al. 2003] D. R. Jin, Z. Y. Meng, and F. Zhou, “Mechanism of resistivity gradient in monolithic PZT ceramics”, *Mater. Sci. Eng. B* **99** (2003), 83–87.
- [Kari et al. 2008] S. Kari, H. Berger, and U. Gabbert, “Numerical evaluation of effective material properties of piezoelectric fibre composites”, pp. 109–120 in *Micro-macro-interactions: in structured media and particle systems*, edited by A. Bertram and J. Tomas, Springer, Berlin, 2008.
- [Klicker et al. 1981] K. A. Klicker, J. V. Biggers, and R. E. Newnham, “Composites of PZT and epoxy for hydrostatic transducer applications”, *J. Am. Ceram. Soc.* **64** (1981), 5–9.
- [Kumar et al. 2006] B. P. Kumar, H. H. Kumar, and D. K. Kharat, “Effect of porosity on dielectric properties and microstructure of porous PZT ceramics”, *Mater. Sci. Eng. B* **127** (2006), 130–133.
- [Lekhnitskii 1957] S. G. Lekhnitskii, *Анизотропные пластинки*, 2nd ed., Gostekhdat, Moscow, 1957. Translated as *Anisotropic plates*, Gordon and Breach, New York, 1968.
- [Lekhnitskii 1977] S. G. Lekhnitskii, *Теория упругости анизотропного тела*, 2nd ed., Nauka, Moscow, 1977. Translated as *Theory of elasticity of an anisotropic body*, Mir, Moscow, 1981.
- [Li et al. 2001] J. F. Li, K. Takagi, N. Terakubo, and R. Watanabe, “Electrical and mechanical properties of piezoelectric ceramic/metal composites in the Pb(Zr, Ti)O<sub>3</sub>/Pt system”, *Appl. Phys. Lett.* **79** (2001), 2441–2443.
- [Li et al. 2003] J. F. Li, K. Takagi, M. Ono, W. Pan, R. Watanabe, and A. Almajid, “Fabrication and evaluation of porous piezoelectric ceramics and porosity-graded piezoelectric actuators”, *J. Am. Ceram. Soc.* **86** (2003), 1094–1098.
- [Lu and Williams 1998] P. Lu and F. W. Williams, “Green functions of piezoelectric material with an elliptic hole or inclusion”, *Int. J. Solids Struct.* **35** (1998), 651–664.
- [Moorthy and Ghosh 1996] S. Moorthy and S. Ghosh, “A model for analysis of arbitrary composite and porous microstructures with Voronoi cell finite elements”, *Int. J. Numer. Methods Eng.* **39** (1996), 2363–2398.
- [Odegard 2004] G. M. Odegard, “Constitutive modeling of piezoelectric polymer composites”, *Acta Mater.* **52**:18 (2004), 5315–5330.
- [Piltner 1985] R. Piltner, “Special finite elements with holes and internal cracks”, *Int. J. Numer. Methods Eng.* **21**:8 (1985), 1471–1485.
- [Piltner 2008] R. Piltner, “Some remarks on finite elements with an elliptic hole”, *Finite Elem. Anal. Des.* **44**:12-13 (2008), 767–772.
- [Sheng et al. 2006] N. Sheng, K. Y. Sze, and Y. K. Cheung, “Trefftz solutions for piezoelectricity by Lekhnitskii’s formalism and boundary collocation method”, *Int. J. Numer. Methods Eng.* **65** (2006), 2113–2138.
- [Sosa 1991] H. Sosa, “Plane problems in piezoelectric media with defects”, *Int. J. Solids Struct.* **28**:4 (1991), 491–505.
- [Stroh 1958] A. N. Stroh, “Dislocations and cracks in anisotropic elasticity”, *Philos. Mag.* (8) **3**:30 (1958), 625–646.
- [Tikhonov and Arsenin 1974] A. N. Tikhonov and V. Y. Arsenin, *Методы решения некорректных задач*, Nauka, Moscow, 1974. Translated as *Solutions of ill-posed problems*, Winston, Washington, DC, 1977.
- [Wang and Qin 2012] H. Wang and Q.-H. Qin, “A new special element for stress concentration analysis of a plate with elliptical holes”, *Acta Mech.* **223**:6 (2012), 1323–1340.
- [Wang et al. 2004] X. W. Wang, Y. Zhou, and W. L. Zhou, “A novel hybrid finite element with a hole for analysis of plane piezoelectric medium with defects”, *Int. J. Solids Struct.* **41** (2004), 7111–7128.
- [Xu and Rajapakse 1998] X. L. Xu and R. K. N. D. Rajapakse, “Boundary element analysis of piezoelectric solids with defects”, *Compos. B Eng.* **29**:5 (1998), 655–669.
- [Xu and Rajapakse 1999] X. L. Xu and R. K. N. D. Rajapakse, “Analytical solution for an arbitrarily oriented void/crack and fracture of piezoceramics”, *Acta Mater.* **47** (1999), 1735–1747.

[Zhang and Katsube 1995] J. Zhang and N. Katsube, “A hybrid finite element method for heterogeneous materials with randomly dispersed rigid inclusions”, *Int. J. Numer. Methods Eng.* **38** (1995), 1635–1653.

[Zhang and Katsube 1997] J. Zhang and N. Katsube, “A polygonal element approach to random heterogeneous media with rigid ellipses or elliptic voids”, *Comput. Methods Appl. Mech. Eng.* **148** (1997), 225–234.

Received 7 Dec 2013. Revised 10 Apr 2014. Accepted 8 May 2014.

PETER L. BISHAY: [PBishay@stmartin.edu](mailto:PBishay@stmartin.edu)

*Center for Aerospace Research and Education (CARE), The Henry Samueli School of Engineering, University of California, Irvine, 4200 Engineering Gateway, Irvine, CA 92697, United States*

and

*The Hal and Inge Marcus School of Engineering, Saint Martin’s University, 5000 Abbey Way SE, OM 329, Lacey, WA 98503-7500, United States*

ABDULLAH ALOTAIBI: [aalotaibi@kau.edu.sa](mailto:aalotaibi@kau.edu.sa)

*Department of Mathematics, Faculty of Sciences, King Abdulaziz University, P.O. Box 80203, Jeddah 21589, Saudi Arabia*

SATYA N. ATLURI: [satluri@uci.edu](mailto:satluri@uci.edu)

*Center for Aerospace Research and Education (CARE), The Henry Samueli School of Engineering, University of California, Irvine, 4200 Engineering Gateway, Irvine, CA 92697, United States*

and

*Faculty of Engineering, King Abdulaziz University, Jeddah 22254, Saudi Arabia*

## ANALYTICAL SOLUTION FOR DUCTILE AND FRC PLATES ON ELASTIC GROUND LOADED ON A SMALL CIRCULAR AREA

ENRICO RADI AND PIETRO DI MAIDA

The problem of a large FRC slab resting on a Winkler-type elastic foundation and subject to a transversal load distributed over a small circular area is investigated in the present work. The mechanical behavior is described by the Kirchhoff theory of elastic-perfectly plastic plates obeying Johansen's yield criterion and associative flow rule. The governing equations within both the inner elastic-plastic circular region near to the loaded area and the outer elastic region are found in terms of the transversal displacement and solved in closed form, under the hypothesis of proportional loading. After the formation of positive yield lines, namely radial cracks at the bottom side of the plate, the onset of a negative yield line, namely a circumferential crack at the upper side of the, defines the load-carrying capacity of the slab on grade. Two possible configurations are envisaged, depending on whether the circumferential crack occurs within the inner elastic-plastic region, where radial cracks take place on the bottom side thus activating a plastic mechanism, or within the outer uncracked elastic region. The ratio between the subgrade modulus and flexural rigidity of the plate allows introducing a characteristic length. The influence of both material and geometrical parameters on the load-carrying capacity of the plate is then investigated. Based on the analytical results, a simplified method for the calculation of the load-carrying capacity of FRC slabs on grade is also proposed and compared with previously developed models.

### 1. Introduction

Concrete slabs on ground floor of factory buildings are designed to support heavy concentrated loads transmitted by columns, vehicle wheels and machinery arranged on them. To prevent cracking and collapse of concrete industrial floors, the introduction of steel reinforcement and/or welded wire meshes is a current practice. Alternatively, the addition of steel or polymeric fibers in the concrete mix may totally or partially substitute the steel reinforcement. The latter solution is becoming widely used in the construction of concrete slabs on grade, since it has proved to be efficient and cost-effective. Indeed, it can provide crack control for shrinkage and temperature effects. Moreover, it may improve the mechanical properties of concrete, as well as the flexural behavior and the fracture toughness of the slab, resulting in significant load-carrying capacity after the concrete has cracked [Falkner et al. 1995]. Full advantage of the addition of fibers to the concrete mix occurs for statically indeterminate structures, where plastic hinges and redistribution of stress take place. In particular, the post cracking capacity of the FRC slabs allows for a redistribution of moments after initial cracking, which let the FRC slab behave in a ductile manner thus increasing its carrying capacity [Barros and Figueiras 1998; 1999; 2001]. However, a valuable increase in the load-carrying capacity of the slab occurs only for a proper dosage of fibers.

*Keywords:* Kirchhoff plate theory, Winkler elastic subgrade, load-carrying capacity, yield lines, elastic-perfectly plastic material, Johansen's yield criterion, fiber reinforced concrete.

Indeed, the results of large scale load tests [Bischoff et al. 2003] predict that a low dosage of fibers provides little improvement when compared with unreinforced concrete slab and thus is not an effective substitute for welded wire reinforcement in slabs on grade.

Due to the damping effect of the soil out of the loaded region, the problem of a concentrated load acting on the top of a FRC slab on grade, or uniformly distributed over a small circular area, can be modeled by considering an infinitely large Kirchhoff plate resting on an elastic foundation. Within these assumptions, the elastic theory developed by Westergaard [1948] provides an approximate solution that is reliable for small loads only. Westergaard approach is also not suitable for FRC slabs because it does not take into account the post crack behavior. For a better evaluation of the load-carrying capacity of FRC slabs, the nonlinear behavior of fiber reinforced concrete must necessarily be taken into account. Following this approach, Meyerhof [1960; 1962] performed a limit analysis of the problem, by considering rigid-perfectly plastic behavior of the material. This author assumed that the slab is driven into the subgrade until a conical plastic mechanism develops in the slab, consisting of an infinite number of radial positive yield lines (centered fan) and an ultimate circumferential crack (i.e., a negative yield line), whose radius is determined in an approximate way. According to the upper-bound theorem of limit analysis, this kind of analysis should predict an upper bound to the collapse load, being performed under the assumption of a kinematically admissible collapse mechanism, which does not necessarily coincide with the effective one.

Generally, investigations based on the limit analysis theory [Meyerhof 1960; 1962; Gazetas and Tassios 1978; Losberg 1978, Baumann and Weisgerber 1983, Rao and Singh 1986] supply statically inadmissible distributions of bending moments and shear forces and/or introduce some degrees of arbitrariness in the choice of the plastic mechanism, e.g., in the radius of the circumferential crack and distribution of the subgrade reaction. Moreover, the limit analysis theory does not provide the plate deflection under the ultimate load. Later, the finite element method was employed by Shentu et al. [1997] in order to analyze the stress and deformation fields in concrete slabs on ground, by considering Ottosen's failure criterion. On the basis of these numerical investigations, a new analytical method was proposed [ibid.] for computing the ultimate load-carrying capacity of concrete slabs on ground. However, the model requires the measurement of the direct tensile strength of the concrete, which may introduce a high degree of uncertainty. Belenkiy [2007] proposed an application of the principle of stationary total energy in order to obtain an upper bound solution of bending problems for plates on elastic foundation.

A limited amount of work also exists on elastic-perfectly plastic plates on elastic foundations [Sokól-Supel 1985; 1988; Kocatürk 1997]. By extending the analysis developed by Tekinalp [1957] for a ductile plate under bending, Sokól-Supel performed analytical studies on the behavior of a metallic circular plate with clamped, hinged or free edge on a tensionless Winkler foundation under axisymmetric, statically increasing loading. In a preliminary work [Sokól-Supel 1985], the material is assumed to obey the Johansen's yield criterion with the associative flow rule. Then, a Tresca-type yield criterion is considered in a following study [Sokól-Supel 1988]. Later, the investigations have been extended to elastic-plastic subgrade under column load [Kocatürk 1997]. More general yielding criteria that can be adopted for concrete and FRC have been recently formulated by Bigoni and Piccolroaz [2004], Piccolroaz and Bigoni [2009] and Poltronieri et al. [2014]. These elastic-plastic constitutive models may correctly represent triaxial test results at high confining pressure and thus they can be efficiently adopted to describe the stress state arising under and in proximity of the loaded region.

A refined analytical investigation of the load-carrying capacity for a large FRC slabs on grade loaded on a small internal area is presented here. The model assumes elastic-perfectly plastic behavior of the material in order to simulate the post cracking behavior of FRC. As well known, concrete is an inhomogeneous and brittle material. Its stress-strain curve is nonlinear and appears somewhat ductile. However, with a proper dosage of fibers, the degree of ductility in FRC concrete can be opportunely improved [Concrete Society 2003]. After initial diffusion of radial cracks from the loaded area to the outer elastic region, the post cracking capacity of the FRC slabs allows for a redistribution of moments, which let the FRC slab behave in a ductile manner, thus remarkably increasing its carrying capacity with respect to plain concrete. Failure of the plate is then due to the onset of a circumferential crack on the top of the slab.

The governing ODEs for adjacent regions of the plate are derived and solved in closed form in Section 2. Accordingly, the boundary conditions between adjacent regions at the onset of the circumferential crack are set in Section 3. Two admissible configurations are envisaged, depending on whether the circumferential crack occurs within the inner radially cracked region or the outer elastic region. Some details on the calculation of ultimate bending moments in FRC slab are recalled in Section 4, according to the recommendations of the Concrete Society [2003]. Analytical results are presented in Section 5 for different material and geometrical parameters. By matching the analytical results, a simplified equation is also proposed for the calculation of the load-bearing capacity of FRC slab on grade and compared with already known solutions. The obtained analytical results thus improve the findings of the rigid-plastic analyses based on the upper-bound theorem of limit analysis and agree with widely adopted relations derived from loading tests.

## 2. Governing equations

In the following, the load carrying capacity of an infinite FRP-concrete plate resting on a Winkler-type elastic foundation is investigated by assuming elastic-perfectly plastic behavior of the plate obeying Johansen's yield criterion and associative flow rule. Moreover, bilateral contact is considered between plate and subgrade, so that the plate cannot lift off the subgrade.

Reference is made to a polar coordinate system  $(r, \theta)$  whose origin lays at the center of the loaded area of radius  $a$  (Figure 1). The external load  $P$  is applied on the upper plate surface as a uniform pressure  $p$  over a small circle of radius  $a$  centered at the origin of the polar coordinates system (Figure 1), so that the distributed load intensity is  $p = P/\pi a^2$ . In order to avoid punching failure, the radius  $a$  should not be less than the thickness of the slab [Meyerhof 1960].

Both in the elastic and elastic-plastic regions of the plate, the equilibrium equations under axisymmetrical conditions require

$$(rm_r)' - m_\theta + rt_r = 0, \quad (1)$$

$$(rt_r)' + r(kw - p) = 0, \quad (2)$$

where the apex denotes derivative with respect to  $r$ ,  $m_r$  and  $m_\theta$  are the bending moments per unit length,  $t_r$  is the transverse shear force per unit length, whose positive directions are shown in Figure 2, right,  $w$  is the out-of-plane displacement, positive if directed towards the subgrade, and  $k$  is the subgrade modulus.

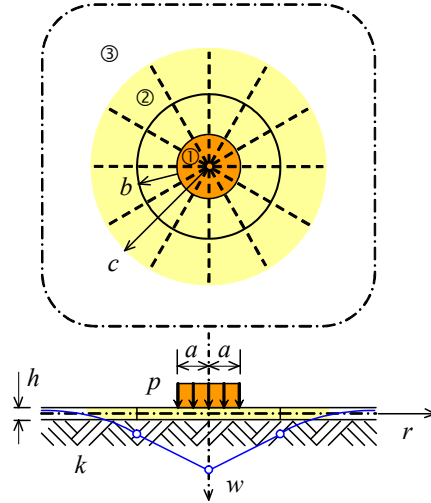


**Figure 1.** Loaded plate on elastic foundation, yield lines and plastic collapse mechanism: (1) elastic-plastic loaded region; (2) elastic-plastic unloaded region; (3) elastic region.

Under axisymmetrical conditions, all field variables depend on  $r$  only and, thus, they are independent of the angular coordinate  $\theta$ .

Johansen’s square yield criterion is assumed to hold for the plate (Figure 2, left), namely

$$-m_0^- \leq m_r \leq m_0^+, \quad -m_0^- \leq m_\theta \leq m_0^+, \tag{3}$$

where  $m_0^+$  and  $m_0^-$  are the positive and negative yield moments per unit length.

According to the Kirchhoff plate theory, the material fibers orthogonal to the midplane do not change their length but they just undergo a rigid rotation about the axes orthogonal to the radial direction, namely

$$\phi_\theta = -w'_3. \tag{4}$$

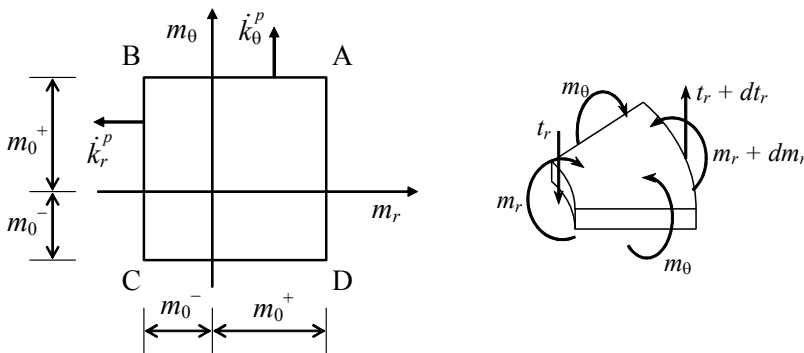


**Figure 2.** Left: Johansen’s yield locus for plates and flow rule for plastic curvatures  $k_\theta^p$  and  $k_r^p$ . Right: positive bending moments and shear force for unit length.

If the plate is driven into the soil by increasing the load, at first positive plastic moments occur along radial yield lines up to a distance  $c$  to the center of the loaded area, where the yield condition

$$m_{\theta}(r) = m_0^+ \quad \text{for } r \leq c \quad (5)$$

is attained. Correspondingly, radial cracks form and propagate along the radial direction at the bottom of the slab. In line with Meyerhof [1962], the ultimate bearing capacity of the plate is attained as a circumferential crack takes place on the top of the slab at a distance  $b$ , which can be smaller, equal or larger than  $c$ , where the radial bending moment becomes equal to the negative yield moment, namely

$$m_r(b) = -m_0^-, \quad (6)$$

so that a circumferential crack originates on the top of the slab (Figure 1). Accordingly, the bending moment  $m_r$  attains a minimum at the radial distance  $r = b$  to the center, namely:

$$m_r'(b) = 0. \quad (7)$$

Outside the circular region of radius  $c$ , the plate behaves elastically. Therefore, the distance  $c$  of the inner border of the elastic region is defined by the fulfillment of the yield condition (3), namely

$$m_{\theta}(c) = m_0^+. \quad (8)$$

Actually, the load-carrying capacity of the slab on grade is not exhausted after the formation of the circumferential crack, since the grade may carry further load. However, the usefulness and serviceability of the slab may be greatly impaired.

**2.1. Elastic-perfectly plastic region.** Let us consider the inner region of the plate for  $r \leq c$ , which undergoes elastic-perfectly plastic deformation and is subject to radial cracking at its bottom. Within this region, the bending moment  $m_{\theta}$  attains its positive limit value  $m_0^+$  according to the yield condition (5), which corresponds to the side AB of the yield locus (Figure 2, left). Under proportional loadings, the elastic-plastic constitutive equations for the bending moments are assumed in the integrated form

$$m_r = D(k_r^e + \nu k_{\theta}^e), \quad m_{\theta} = D(k_{\theta}^e + \nu k_r^e), \quad (9)$$

being  $D = Eh^3/12(1 - \nu^2)$  the flexural rigidity of the plate, where  $h$  is the plate thickness,  $E$  is the Young modulus and  $\nu$  is the Poisson coefficient of the material (approximately 0.15). The curvature tensor has been split into elastic and plastic contributions according to

$$k_r = k_r^e + k_r^p = -w''(r), \quad k_{\theta} = k_{\theta}^e + k_{\theta}^p = -w'(r)/r. \quad (10)$$

From (9) the following inverse constitutive relations can be derived for the elastic components of the curvature tensor

$$k_r^e = \frac{m_r - \nu m_{\theta}}{D(1 - \nu^2)}, \quad k_{\theta}^e = \frac{m_{\theta} - \nu m_r}{D(1 - \nu^2)}, \quad (11)$$

whereas the plastic components are given by the associative flow rule for the side AB of the yield locus, namely

$$k_r^p = 0, \quad k_{\theta}^p \geq 0, \quad (12)$$



where no previous plastic yielding is assumed to occur. Therefore, from (5), (10)–(12) and (1) the bending moment and the transverse shear force per unit length in the elastic-plastic region turn out to be

$$m_r = \nu m_0^+ - D(1 - \nu^2)w'', \quad (13)$$

$$t_r = \frac{1 - \nu}{r}[m_0^+ + D(1 + \nu)(w'' + rw''')], \quad (14)$$

respectively. From equilibrium Equations (1) and (2) and yield condition (5) it follows that

$$(rm_r)'' - r(kw - p) = 0. \quad (15)$$

Introduction of (13) into (15) then provides

$$D(1 - \nu^2)(rw'')'' + r(kw - p) = 0, \quad (16)$$

namely

$$w'''' + \frac{2}{r}w''' + \frac{1}{\ell^4(1 - \nu^2)}\left(w - \frac{p}{k}\right) = 0, \quad (17)$$

where

$$l = \sqrt[4]{\frac{D}{k}}, \quad (18)$$

is the characteristic length of plates on elastic foundation. The general solution of the fourth-order linear ODE (17) may be found by using the singular Frobenius method, implemented in Mathematica, in terms of the generalized hypergeometric function  ${}_0F_3$  and Meijer G function  $G_{04}^{20}$  defined in the [Appendix](#), namely

$$w_1(r) = \frac{p}{k} + \frac{m_0^+ \ell^2}{D} \left\{ b_0 {}_0F_3\left(\frac{1}{2}, \frac{3}{4}, \frac{3}{4}; -\frac{(1 - \nu^2)r^4}{256\ell^4}\right) + b_1 \frac{r}{4\ell} {}_0F_3\left(\frac{3}{4}, 1, \frac{5}{4}; -\frac{(1 - \nu^2)r^4}{256\ell^4}\right) \right. \\ \left. + b_2 \left(\frac{r}{4\ell}\right)^2 {}_0F_3\left(\frac{5}{4}, \frac{5}{4}, \frac{3}{2}; -\frac{(1 - \nu^2)r^4}{256\ell^4}\right) + b_3 G_{04}^{20}\left(\begin{matrix} 0 & 0 & 0 & 0 \\ 1/4 & 1/4 & 1/2 & 0 \end{matrix} \middle| -\frac{(1 - \nu^2)r^4}{256\ell^4}\right) \right\}. \quad (19)$$

The displacement field (19) holds for  $r \leq a$ , namely within the inner circular region loaded by  $p$ , whereas the displacement field

$$w_2(r) = \frac{m_0^+ \ell^2}{D} \left\{ c_0 {}_0F_3\left(\frac{1}{2}, \frac{3}{4}, \frac{3}{4}; -\frac{(1 - \nu^2)r^4}{256\ell^4}\right) + c_1 \frac{r}{4\ell} {}_0F_3\left(\frac{3}{4}, 1, \frac{5}{4}; -\frac{(1 - \nu^2)r^4}{256\ell^4}\right) \right. \\ \left. + c_2 \left(\frac{r}{4\ell}\right)^2 {}_0F_3\left(\frac{5}{4}, \frac{5}{4}, \frac{3}{2}; -\frac{(1 - \nu^2)r^4}{256\ell^4}\right) + c_3 G_{04}^{20}\left(\begin{matrix} 0 & 0 & 0 & 0 \\ 1/4 & 1/4 & 1/2 & 0 \end{matrix} \middle| -\frac{(1 - \nu^2)r^4}{256\ell^4}\right) \right\}, \quad (20)$$

holds for  $a \leq r \leq c$ , namely within the elastic-plastic annular region subject to the subgrade reaction only ( $p = 0$ ). The general solutions (19) and (20) of the ODE (17) agree with the results obtained by [Sokól-Supel \[1985; 1988\]](#) and [Kocatürk \[1997\]](#) in terms of infinite power series. The derivatives up to the third order of the functions  $w_1(r)$  and  $w_2(r)$  are supplied in the [Appendix](#).

**2.2. Elastic region.** Under axisymmetric bending, the Kirchhoff theory of elastic plates resting on a Winkler-type elastic foundation [Timoshenko and Woinowsky-Krieger 1959] provides the following ODE for the out-of-plane displacement  $w(r)$

$$w'''' + \frac{2}{r}w''' - \frac{1}{r^2}w'' + \frac{1}{r^3}w' + \frac{1}{\ell^4}w = 0. \tag{21}$$

The general solution of the ODE (21) vanishing as  $r$  becomes very large are given by Timoshenko and Woinowsky-Krieger [1959] in the form

$$w_3(r) = \frac{m_0^+ \ell^2}{D} \left( d_1 \operatorname{ker} \frac{r}{\ell} + d_2 \operatorname{kei} \frac{r}{\ell} \right), \quad \text{for } r \geq c, \tag{22}$$

where  $\operatorname{ker}$  and  $\operatorname{kei}$  are the Kelvin functions [Abramowitz and Stegun 1964] and  $d_1$  and  $d_2$  are nondimensional arbitrary constants of integration. The derivatives up to the third order of the function  $w_3(r)$  are supplied in the Appendix.

In agreement with the constitutive relations (9), bending moments per unit length for purely elastic response of the plate can be written in terms of the total curvatures as

$$m_r = -D \left( w_3'' + \frac{\nu}{r} w_3' \right), \tag{23}$$

$$m_\theta = -D \left( \frac{w_3'}{r} + \nu w_3'' \right), \tag{24}$$

whereas the transverse shear force per unit length can be obtained from the introduction of the bending moments (23) and (24) into the equilibrium condition (1) as

$$t_r = D \left( w_3''' + \frac{1}{r} w_3'' - \frac{1}{r^2} w_3' \right). \tag{25}$$

### 3. Boundary conditions

The nondimensional constants of integration  $b_k, c_k$  ( $k = 0, 1, 2, 3$ ),  $d_1$  and  $d_2$  introduced in (19), (20) and (22) can be determined by imposing the boundary conditions at  $r = 0$  and  $r \rightarrow \infty$  and continuity conditions for the displacement  $w$ , rotation  $\phi_\theta$ , bending moment  $m_r$  and shear force  $t_r$  between the three different regions delimited by the radii  $a$  and  $c$ , together with the yield condition (8) at the inner border of the elastic region.

The yield condition (5) and symmetry at  $r = 0$  require  $m_r(0) = m_0^+$  and  $t_r(0) = 0$ . By using (13), (14) and (19) both of these conditions provide

$$D(1 + \nu)w_1''(0) + m_0^+ = 0, \tag{26}$$

thus implying

$$b_2 = -\frac{8}{1 + \nu}. \tag{27}$$

Moreover, boundedness of the rotation  $\phi_\theta$  at  $r = 0$  necessarily requires

$$b_3 = 0. \tag{28}$$

Continuity of displacement  $w$ , rotation  $\phi_\theta$ , bending moment  $m_r$  and shear force  $t_r$  across the boundaries at  $r = a$  and  $r = c$ , by using (4), (13), (14), (23) and (25) then requires the eight conditions

$$w_1(a) = w_2(a), \quad w'_1(a) = w'_2(a), \quad w''_1(a) = w''_2(a), \quad w'''_1(a) = w'''_2(a), \quad (29)$$

$$w_2(c) = w_3(c), \quad w'_2(c) = w'_3(c), \quad (30)$$

$$\frac{\nu m_0^+}{D} - (1 - \nu^2)w''_2(c) = -w'''_3(c) - \frac{\nu}{c}w'_3(c), \quad (31)$$

$$(1 - \nu)\frac{m_0^+}{D} + (1 - \nu^2)[w''_2(c) + cw'''_2(c)] = cw'''_3(c) + w'''_3(c) - \frac{1}{c}w'_3(c). \quad (32)$$

By using (24), fulfillment of the yield condition (8) as  $r$  approaches  $c$  from above then implies

$$\nu w''_3(c) + \frac{1}{c}w'_3(c) = -\frac{m_0^+}{D}. \quad (33)$$

The ultimate distributed load  $p = p_0$  is attained as soon as the bending moment  $m_r$  obeys the yield condition (6) at a distance  $b$  determined by the minimum condition (7). Let us first assume that the circumferential crack occurs within the elastic plastic unloaded region, namely for  $a < b < c$ . Then, by using (13), conditions (6) and (7) become

$$D(1 - \nu^2)w''_2(b) = (\nu + \mu)m_0^+, \quad w'''_2(b) = 0, \quad (34)$$

with  $b \leq c$ , where

$$\mu = m_0^-/m_0^+, \quad (35)$$

is the ratio between negative and positive yield moments. If conditions (34) provide  $b > c$  then the minimum value of the radial bending moment  $m_r = -m_0^-$  is attained within the elastic region at  $r = b$ , where a circumferential crack occurs on the top of the slab. In this case, by using (23) conditions (6) and (7) require

$$w''_3(b) + \frac{\nu}{b}w'_3(b) = \mu\frac{m_0^+}{D}, \quad w'''_3(b) + \frac{\nu}{b}w''_3(b) - \frac{\nu}{b^2}w'_3(b) = 0, \quad (36)$$

with  $c < b$ , instead of (34).

By introducing the derivatives of function  $w_k$  ( $k = 1, 2, 3$ ) provided in the Appendix, the boundary conditions (29)–(33) yield a linear system of nine equations for the eight constants of integration  $b_0, b_1, c_0, c_1, c_2, c_3, d_1, d_2$  and the ultimate distributed load  $p_0$ , which can be solved by using Mathematica. Once these nine constants are known in terms of the parameters  $b$  and  $c$ , the two Equations (34) can be solved numerically (using the command FindRoot in Mathematica) in order to obtain the last two unknowns  $b$  and  $c$ . If conditions (34) provide  $b > c$  then conditions (36) must replace the former. Once the values of  $b$  and  $c$  have been obtained, all the unknown constants can be consequently calculated. In particular, the ultimate load is then given by

$$P_0 = \pi a^2 p_0. \quad (37)$$

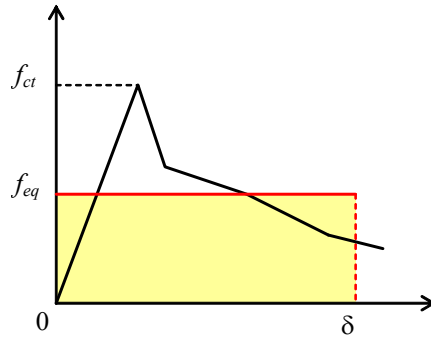


**Figure 3.** Equivalent flexural strength (vertical axis) versus deflection determined from a third-point loading beam.

#### 4. Moment-carrying capacity for FRC slabs

As remarked, for design purposes it is assumed that the limiting criterion is the onset of cracking on the top surface. While fibers increase the post-cracking behavior and thus the ductility of the slab they do not affect the cracking stress, namely they do not increase the negative bending moment capacity [Soutsos et al. 2012] which is therefore the same of the plain concrete

$$m_0^- = m_0^{\text{PC}} = f_{ct} \frac{h^2}{6}, \quad (38)$$

where  $f_{ct}$  the maximum tensile stress derived from a third-point flexural test on a FRC beam.

According to the design method for industrial floor proposed by the Concrete Society [2003], the difference between plain concrete and FRC slabs can be attributed to the post-cracking strength due to the presence of the fibers, which provide an additional contribution to the bending moment capacity, namely

$$m_0^{\text{FRC}} = \frac{R_{e,3}}{100} f_{ct} \frac{h^2}{6}, \quad (39)$$

where  $R_{e,3}$  is the residual flexural strength ratio

$$R_{e,3} = \frac{f_{eq}}{f_{ct}} 100, \quad (40)$$

and  $f_{eq}$  is the equivalent flexural strength for a deflection of 1/150 of the test beam span (Figure 3), namely  $\delta = 3 \text{ mm}$  for a span of 450 mm. The ratio  $R_{e,3}$  is related to the rate of improvement in the flexural strength of FRC compared to plain concrete, according to standard third-point flexural test [Concrete Society 2003].

The ductility of FRC slabs becomes effective after the first crack, namely in the plastic phase when a positive plastic hinge is formed under loading. In this case due to the post-cracking behavior of the fibers, the FRC slab can bear a further increase in the value of the positive bending moment with respect to the plain concrete, so that the total value of the moment-carrying capacity is given by the sum

$$m_0^+ = m_0^{\text{PC}} + m_0^{\text{FRC}} = \left(1 + \frac{R_{e,3}}{100}\right) f_{ct} \frac{h^2}{6}, \quad (41)$$

where  $m_0^+$  is the ultimate positive bending moment. Therefore, for FRC slabs the ratio  $\mu$  between negative and positive yield moments introduced in (35) turns out to be

$$\mu = \frac{100}{100 + R_{e,3}}. \quad (42)$$

## 5. Results

The nondimensional variations of displacement  $w$  and bending moments  $m_r$  and  $m_\theta$  along the radial direction under the ultimate load  $p_0$  are plotted in Figure 4 for different sizes  $a$  of the loaded area, for  $\nu = 0.15$  and for two different values of the ratio  $\mu$  between negative and positive yield moments, namely  $\mu = 0.5$  and  $\mu = 1$ . Figure 4 shows that the displacement  $w$  and thus the reaction  $kw$  of the subgrade increase with the size  $a$  of the loaded area. Figure 4 also shows that all quantities of interest (deflection, tangential and radial moments) become negligible at a distance larger than 4 to 5 times  $\ell$  (denoted by  $4-5\ell$ ) from the applied load. Therefore, the assumption of an infinitely large plate is reliable also for plates of finite size, if they are loaded at a distance larger than  $4-5\ell$  from their edges.

The nondimensional variations of the ultimate load  $P_0$  and radii  $b$  and  $c$  with the radius  $a$  of the loaded area are plotted in Figures 5 and 6, respectively, both for  $\mu = 1$  and  $\mu = 0.5$ . From these figures it can be observed that the ultimate load  $P_0$  increases with the radius  $a$  of the loaded area. Moreover, the radius  $b$  of the circumferential crack turns out to be smaller than  $2\ell$ . It must be remarked that the minimum of the radial bending moment predicted by the elastic analyses of Meyerhof [1960] and Timoshenko and Woinowsky-Krieger [1959] is attained at a distance  $2\ell$  to the center of the loaded area, and this value has been adopted as the radius of the circumferential crack in several investigations based on the limit analysis theory [Westergaard 1948; Baumann and Weisgerber 1983].

As the size  $a$  of the loaded area becomes larger, the radius  $b$  of the circumferential crack increases more rapidly than the length  $c$  of the radial cracks (Figure 6) and the latter two distances become coincident for a special value of  $a$ . Then, the circumferential crack occurs within the elastic region for  $a$  larger than this special value. In this case, however, the onset of the circumferential crack does not imply the activation of a conical plastic mechanism as observed for a small value of  $a$ . However, the formation of a circumferential crack on upper side of the plate defines the serviceability limit of industrial ground floors according to current design standards [Concrete Society 2003].

For use in practice, the following simplified equation for calculating the load-carrying capacity of slabs on grade is proposed on the basis of the analytical results here obtained:

$$P_0^* = 2\pi m_0^+ (1 + \mu) \left( 1 + (1 + \mu) \frac{a}{\ell} \right), \quad (43)$$

where  $\mu$  assumes the value in (42) for FRC slabs. From Figure 5 it can be established that the approximate value  $P_0^*$  introduced in (43) approaches the load carrying capacity  $P_0$  obtained from the present exact analysis. From Table 1, where the values of  $P_0$  and  $P_0^*$  are reported for different sizes of the loaded area, it can be observed that the agreement between analytical and approximate results is excellent for  $\mu = 1$ , whereas for  $\mu = 0.5$  the approximate value  $P_0^*$  underestimates to some extent the ultimate load  $P_0$ , thus providing more conservative results.

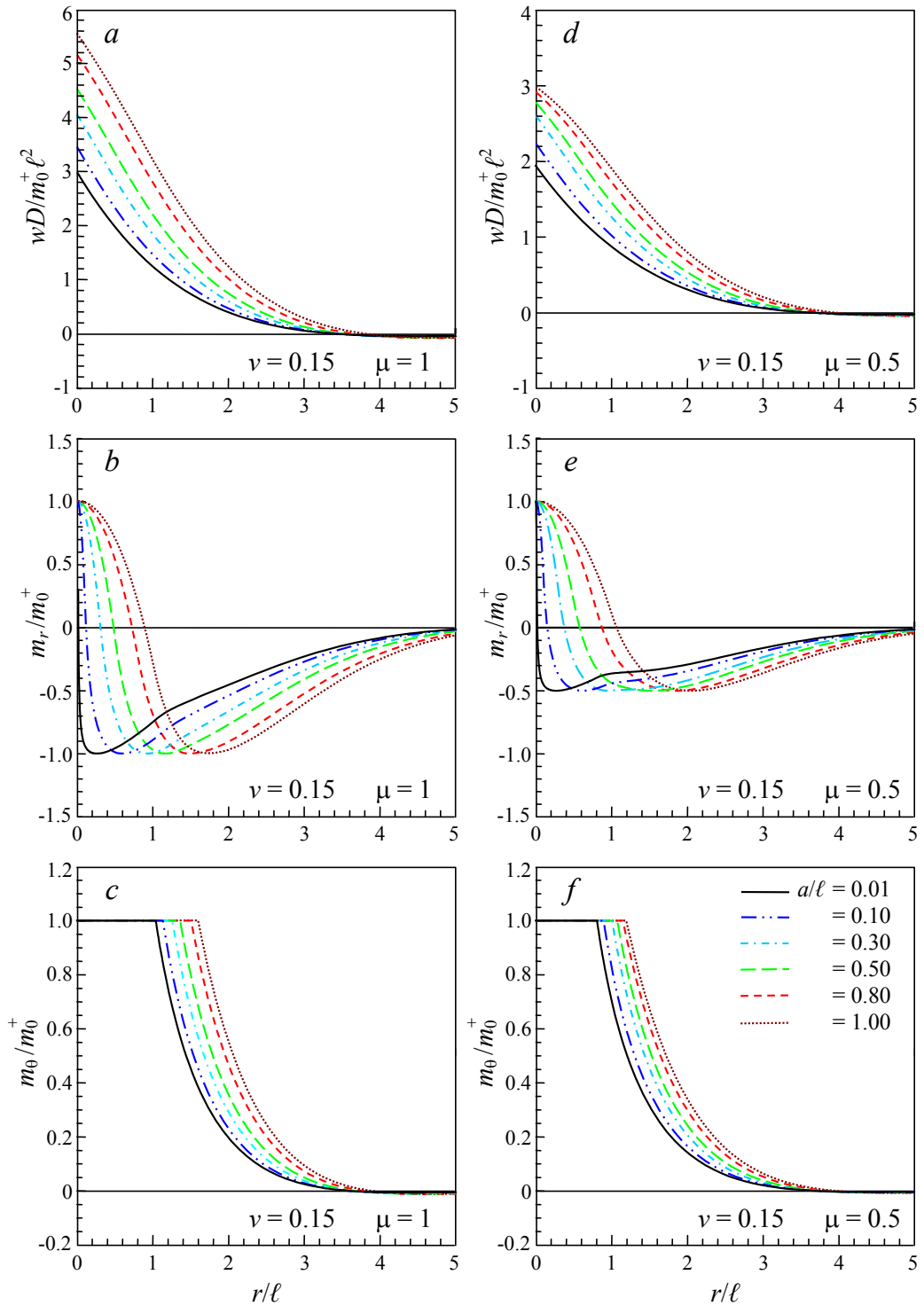


**Figure 4.** Variations of displacement  $w$  and bending moments  $m_r$  and  $m_\theta$  along the radial direction under the collapse load for different sizes  $a$  of the loaded area.

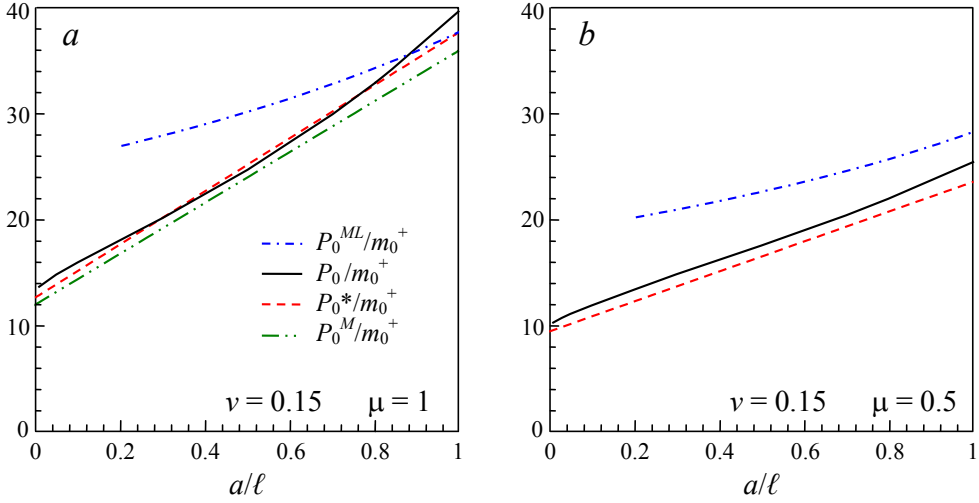


**Figure 5.** Nondimensional variations of the ultimate load  $P_0$ , approximate value  $P_0^*$  and Meyerhof collapse loads  $P_0^{ML}$  and  $P_0^M$  with the radius  $a$  of the loaded area for (a)  $\mu = 1$  and (b)  $\mu = 0.5$ .

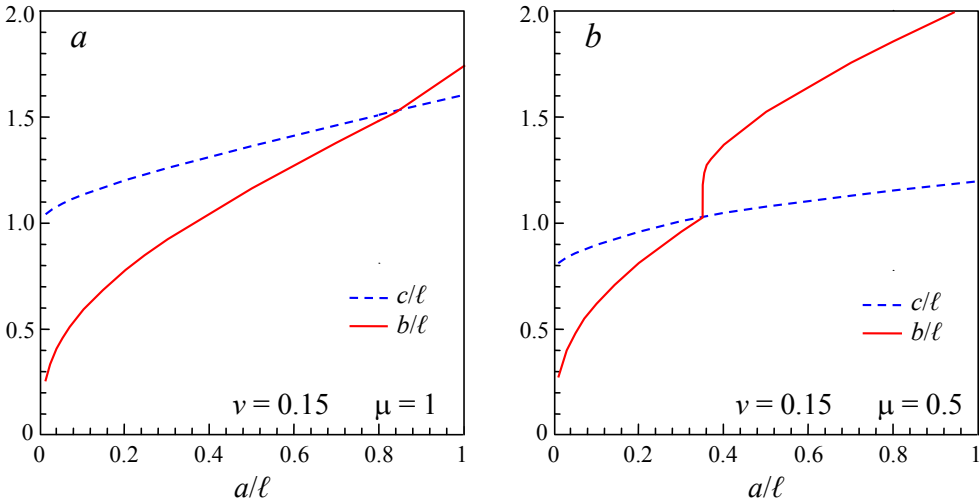


**Figure 6.** Nondimensional variations of the radii  $b$  and  $c$  with the radius  $a$  of the loaded area.

**5.1. Comparison with previous methods.** In the following, the load-carrying capacities found in previous investigations are reported in order to compare them with the predictions of the present analysis. For a large slab Meyerhof [1962] found the ultimate load

$$P_0^{ML} = \frac{4\pi(m_0^+ + m_0^-)}{1 - \frac{a}{3\ell}}, \quad \text{for } a > 0.2\ell, \tag{44}$$

where the assumption  $b \approx 3.9-4\ell$  is made. It must be specified that in the rigid-plastic analysis of



$\mu = 1$			$\mu = 0.5$		
$a/\ell$	$P_0/m_0^+$	$P_0^*/m_0^+$	$a/\ell$	$P_0/m_0^+$	$P_0^*/m_0^+$
0.01	13.6942	12.8177	0.01	10.2513	9.4247
0.05	14.8298	13.8230	0.05	11.0604	10.1316
0.10	15.9689	15.0796	0.10	11.8682	10.8385
0.20	18.0721	17.5929	0.20	13.3502	12.2522
0.30	20.1759	20.1062	0.30	14.8202	13.6659
0.40	22.3747	22.6195	0.40	16.2143	15.0796
0.50	24.7162	25.1327	0.50	17.5310	16.4934
0.70	29.9581	30.1593	0.70	20.3785	19.3208
0.80	32.9149	32.6726	0.80	21.9421	20.7345
1.00	39.5404	37.6991	1.00	25.4027	23.5619

**Table 1.** Ultimate load  $P_0$  and its approximate value  $P_0^*$  for different radii  $a$  of the loaded area, for  $\mu = 1$  (left) and  $\mu = 0.5$  (right).

[Meyerhof 1962], the cracking radius  $b$  is assumed to coincide with the radius of the circular area loaded by the subgrade reaction pressure. In the present elastic-perfectly plastic analysis the circumferential crack is found to occur much inside the area loaded by the subgrade reaction pressure. The results depicted in Figure 6 show that the assumption  $b \approx 3.9-4\ell$  [Meyerhof 1962] made in the derivation of (44) may be acceptable for the size of the area loaded by the subgrade reaction pressure (see Figures 5(a) and 5(d)), but is rather inaccurate for the cracking radius. The present analysis, indeed, predicts a cracking radius  $b$  about  $1-1.5\ell$  (see Figure 6) and thus much smaller than the value assumed in the derivation of (44). The load-carrying capacity (44) predicted by Meyerhof [1962] would remarkably increases if values of  $b$  smaller than  $4\ell$  are considered, e.g.,  $b \leq 2\ell$ , thus providing non conservative and unrealistic results.

The load-carrying capacity of the plate under a concentrated load provided by Meyerhof [1962] is

$$P_0^{ML} = 2\pi(m_0^+ + m_0^-) \quad \text{for } a = 0. \tag{45}$$

It can be observed that for a vanishing small size  $a$  of the loaded area, Equation (43) coincides with the result (45) obtained by Meyerhof under a concentrated force.

The use of  $m_0^- = 0$  in Equations (44) and (45) is recommended for small slabs that can not develop a negative bending moment along the negative circumferential yield line [Meyerhof 1962]. In this case, the load-carrying capacity of small slabs  $P_0^{MS}$  is reduced to about one-half with respect to a large slab, and thus expressions (44) and (45) may be too conservative if adopted for sufficiently large slabs with  $m_0^- = 0$ . However, similar expressions have also been accepted by the Concrete Society [2003], with no specification about the extension of the slab.

On the basis of the results of both limit analysis theory and loading tests, the following simple and conservative formula is suggested in [Meyerhof 1962] for a central load

$$P_0^M = 6(m_0^+ + m_0^-) \left(1 + 2\frac{a}{\ell}\right), \tag{46}$$

with  $a > h$  in order to avoid punching failure. Moreover, the following approximate relation for the radius of the circumferential crack

$$\frac{b}{\ell} = 1.63 \sqrt{\frac{a}{\ell}}, \quad (47)$$

was also proposed by Meyerhof [1960]. Relations (46) and (47) reasonably agree with the analytical results here obtained for elastic-perfectly plastic behavior of the plate, with  $\mu = 1$ , as it can be verified by comparing Equations (46) and (43) and the results plotted in Figures 5(a) and 7(b). In particular, the difference between relations (46) and (43) is less than 5%, for  $\mu = 1$ . On the contrary, the load carrying capacity (44) predicted by Meyerhof for large slabs turns out to be much higher than the findings of the present analysis. As already discussed, this result is expected according to the upper-bound theorem of limit analysis, since the Meyerhof analysis is based on the assumption of a rigid-plastic mechanism.

The ultimate load proposed by Baumann and Weisgerber [1983] is

$$P_0^{\text{BW}} = \frac{8\pi(m_0^+ + m_0^-)}{3(1 - \frac{a}{3\ell})^2} \left(1 - \frac{11a}{32\ell}\right), \quad (48)$$

where the same cracking radius  $b = 2\ell$  predicted by the elastic solution [Westergaard 1948; Timoshenko and Woinowsky-Krieger 1959] has been considered.

The ultimate load found by Rao and Singh [1986] for a single plastic hinge centered under the loaded area becomes

$$P_0^{\text{RS}} = 2\pi(m_0^+ + m_0^-) \frac{1.8 + 6.9a/\ell}{1.8 + 2.9a/\ell}. \quad (49)$$

These authors evaluated the cracking radius  $b$  throughout the following relation

$$\frac{b}{\ell} = 0.6 + 2.3 \frac{a}{\ell}, \quad (50)$$

derived from a hundred experimental observations made for plain and reinforced concrete.

The load-carrying capacities  $P_0$  and the cracking radius  $b$  predicted by the present model and by previously developed analyses are compared for  $\mu = 1$  in Figures 7(a) and 7(b), respectively. From these plots it can be observed that the present model provides higher load-carrying capacities than the other models, except for the result (44) obtained by Meyerhof [1962] for large slabs. Moreover, the radius  $b$  of the circumferential crack predicted by the present analysis closely agrees with the approximation (47) proposed by Meyerhof [1960], at least for  $\mu = 1$ , whereas it is clearly smaller than the value  $2\ell$  predicted by the elastic analyses and that adopted by Rao and Singh [1986] for the derivation of (50).

Unfortunately, experimental results are not easily available in the literature for slabs larger than  $8-10\ell$ , thus allowing the formation of a circumferential crack. Most of the performed tests concern small slabs whose collapse mechanism consists of radial cracks reaching the edges of the slab, with no formation of the circumferential crack on the top surface [Chen 2004; Roesler et al. 2004; 2006].

## 6. Conclusions

A refined model for the evaluation of the load-carrying capacity of large FRC slabs on ground has been presented here. The model takes into account the post-crack strength of FRC slabs and the associated ductile behavior. Compared with the approaches based on the limit analysis theory, the present model is

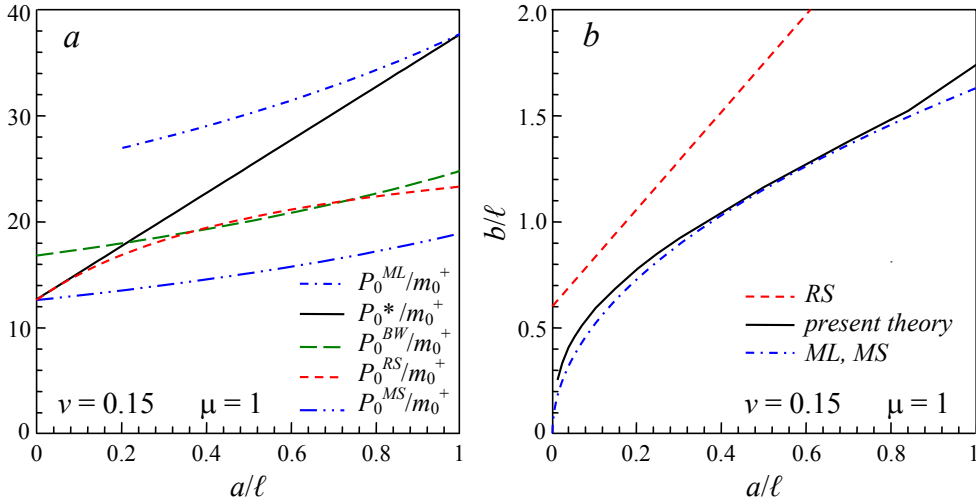


**Figure 7.** Comparison between the load-carrying capacity  $P_0$  and cracking radius  $b$  predicted by the present model and by previous theories.

more accurate and complete, since it does not require the introduction of rough approximations on the collapse mechanism and location of the yield lines. The proposed approach provides more conservative results with respect to the prediction of the Meyerhof model for large slabs. However, it is in reasonable agreement with the approximate formula (46) suggested by Meyerhof [1962] on the basis of loading tests. Moreover, the load-carrying capacity provided by the present method turns out to be higher than those recommended by conventional codes for industrial ground floors [Concrete Society 2003], which are generally based on the results of Meyerhof analysis for small slabs on grade.

Differently from the investigations based on limit analysis, the present model is also able to predict the deflection under the ultimate load, and thus it can be validated by comparison with experimental results. Moreover, being deflection a crucial aspect for the design of ground slab, deflection limiting criteria can be easily implemented within the framework of the present method.

The interaction between slab and subgrade has been here modeled by adopting the simple Winkler elastic model. However, more refined approaches can be envisaged within the same framework, which can take into account for tensionless subgrade reaction [Gazetas 1981; Silva et al. 2001], frictional contact [Chen 2004] and nonlocal response of the foundation, like the model adopted by Nobili et al. [2014] and Lanzoni et al. [2014] for the study of cracked elastic plates on Pasternak foundation.

Finally, it must be remarked that a large moment-rotation capacity after yielding must be assured, the present approach being based on the yield line method, commonly used to determine the load capacity of ductile and RC slabs. However, application of the present results to materials exhibiting brittle or softening behavior, like lightly reinforced concrete, may be questionable.

### Appendix

By using the following derivative rule for the hypergeometric function  ${}_0F_3$  and Meijer  $G$  function  $G_{04}^{20}$

[Luke 1969; Lardner 1969]

$$\begin{aligned} \frac{d}{dx} {}_0F_3(\alpha, \beta, \gamma; x) &= \frac{1}{\alpha\beta\gamma} {}_0F_3(\alpha + 1, \beta + 1, \gamma + 1; x), \\ \frac{d}{dx} G_{04}^{20} \left( \begin{matrix} 0 & 0 & 0 & 0 \\ \alpha & \alpha & \beta & 0 \end{matrix} \middle| x \right) &= G_{04}^{20} \left( \begin{matrix} 0 & 0 & 0 & 0 \\ \alpha - 1 & \alpha - 1 & \beta - 1 & 0 \end{matrix} \middle| x \right), \end{aligned} \quad (\text{A.1})$$

the derivatives up to the third order with respect to  $r$  of the function  $w_1(r)$  introduced in (19) can be written as

$$\begin{aligned} w_1'(r) &= \frac{m_0^+ \ell}{D} \left\{ -b_0 \frac{(1-\nu^2)r^3}{18\ell^3} {}_0F_3 \left( \frac{3}{2}, \frac{7}{4}, \frac{7}{4}; -\frac{(1-\nu^2)r^4}{256\ell^4} \right) \right. \\ &\quad + b_1 \left[ \frac{1}{4} {}_0F_3 \left( \frac{3}{4}, 1, \frac{5}{4}; -\frac{(1-\nu^2)r^4}{256\ell^4} \right) - \frac{(1-\nu^2)r^4}{240\ell^4} {}_0F_3 \left( \frac{7}{4}, 2, \frac{9}{4}; -\frac{(1-\nu^2)r^4}{256\ell^4} \right) \right] \\ &\quad + b_2 \left[ \frac{r}{8\ell} {}_0F_3 \left( \frac{5}{4}, \frac{5}{4}, \frac{3}{2}; -\frac{(1-\nu^2)r^4}{256\ell^4} \right) - \frac{(1-\nu^2)r^5}{2400\ell^5} {}_0F_3 \left( \frac{9}{4}, \frac{9}{4}, \frac{5}{2}; -\frac{(1-\nu^2)r^4}{256\ell^4} \right) \right] \\ &\quad \left. - b_3 \frac{(1-\nu^2)r^3}{64\ell^3} G_{04}^{20} \left( \begin{matrix} 0 & 0 & 0 & 0 \\ -3/4 & -3/4 & -1/2 & 0 \end{matrix} \middle| -\frac{(1-\nu^2)r^4}{256\ell^4} \right) \right\}, \end{aligned} \quad (\text{A.2})$$

$$\begin{aligned} w_1''(r) &= \frac{m_0^+}{D} \left\{ b_0 \frac{(1-\nu^2)r^2}{6\ell^2} \left[ \frac{(1-\nu^2)r^4}{882\ell^4} {}_0F_3 \left( \frac{5}{2}, \frac{11}{4}, \frac{11}{4}; -\frac{(1-\nu^2)r^4}{256\ell^4} \right) - {}_0F_3 \left( \frac{3}{2}, \frac{7}{4}, \frac{7}{4}; -\frac{(1-\nu^2)r^4}{256\ell^4} \right) \right] \right. \\ &\quad + b_1 \frac{(1-\nu^2)r^3}{48\ell^3} \left[ \frac{(1-\nu^2)r^4}{2520\ell^4} {}_0F_3 \left( \frac{11}{4}, 3, \frac{13}{4}; -\frac{(1-\nu^2)r^4}{256\ell^4} \right) - {}_0F_3 \left( \frac{7}{2}, 2, \frac{9}{4}; -\frac{(1-\nu^2)r^4}{256\ell^4} \right) \right] \\ &\quad + \frac{b_2}{2400} \left[ 300 {}_0F_3 \left( \frac{5}{4}, \frac{5}{4}, \frac{3}{2}; -\frac{(1-\nu^2)r^4}{256\ell^4} \right) - 7 \frac{(1-\nu^2)r^4}{\ell^4} {}_0F_3 \left( \frac{9}{4}, \frac{9}{4}, \frac{5}{2}; -\frac{(1-\nu^2)r^4}{256\ell^4} \right) \right. \\ &\quad \left. + \frac{(1-\nu^2)^2 r^8}{810\ell^8} {}_0F_3 \left( \frac{13}{4}, \frac{13}{4}, \frac{7}{2}; -\frac{(1-\nu^2)r^4}{256\ell^4} \right) \right] \\ &\quad - b_3 \frac{(1-\nu^2)r^2}{64\ell^2} \left[ 3 G_{04}^{20} \left( \begin{matrix} 0 & 0 & 0 & 0 \\ -3/4 & -3/4 & -1/2 & 0 \end{matrix} \middle| -\frac{(1-\nu^2)r^4}{256\ell^4} \right) \right. \\ &\quad \left. - \frac{(1-\nu^2)r^4}{64\ell^4} G_{04}^{20} \left( \begin{matrix} 0 & 0 & 0 & 0 \\ -7/4 & -7/4 & -3/2 & 0 \end{matrix} \middle| -\frac{(1-\nu^2)r^4}{256\ell^4} \right) \right] \right\}, \end{aligned} \quad (\text{A.3})$$

$$\begin{aligned} w_1'''(r) &= \frac{m_0^+}{D\ell} \left\{ b_0 \frac{(1-\nu^2)r}{3\ell} \left[ -\frac{(1-\nu^2)^2 r^8}{2134440\ell^8} {}_0F_3 \left( \frac{7}{2}, \frac{15}{4}, \frac{15}{4}; -\frac{(1-\nu^2)r^4}{256\ell^4} \right) \right. \right. \\ &\quad \left. + \frac{(1-\nu^2)r^4}{196\ell^4} {}_0F_3 \left( \frac{5}{2}, \frac{11}{4}, \frac{11}{4}; -\frac{(1-\nu^2)r^4}{256\ell^4} \right) - {}_0F_3 \left( \frac{3}{2}, \frac{7}{4}, \frac{7}{4}; -\frac{(1-\nu^2)r^4}{256\ell^4} \right) \right] \\ &\quad + b_1 \frac{(1-\nu^2)r^2}{10080\ell^2} \left[ -\frac{(1-\nu^2)^2 r^8}{20592\ell^8} {}_0F_3 \left( \frac{15}{4}, 4, \frac{17}{4}; -\frac{(1-\nu^2)r^4}{256\ell^4} \right) \right. \\ &\quad \left. + \frac{(1-\nu^2)r^4}{\ell^4} {}_0F_3 \left( \frac{11}{4}, 3, \frac{13}{4}; -\frac{(1-\nu^2)r^4}{256\ell^4} \right) - 630 {}_0F_3 \left( \frac{7}{4}, 2, \frac{9}{4}; -\frac{(1-\nu^2)r^4}{256\ell^4} \right) \right] \\ &\quad + b_2 \frac{(1-\nu^2)r^3}{129600\ell^3} \left[ -\frac{(1-\nu^2)^2 r^8}{35490\ell^8} {}_0F_3 \left( \frac{17}{4}, \frac{17}{4}, \frac{9}{2}; -\frac{(1-\nu^2)r^4}{256\ell^4} \right) \right. \\ &\quad \left. + \frac{(1-\nu^2)r^4}{\ell^4} {}_0F_3 \left( \frac{13}{4}, \frac{13}{4}, \frac{7}{2}; -\frac{(1-\nu^2)r^4}{256\ell^4} \right) - 1620 {}_0F_3 \left( \frac{9}{4}, \frac{9}{4}, \frac{5}{2}; -\frac{(1-\nu^2)r^4}{256\ell^4} \right) \right] \end{aligned}$$

$$\begin{aligned}
 & -b_3 \frac{(1-\nu^2)r}{4096\ell} \left[ 384G_{04}^{20} \left( \begin{array}{cccc|c} 0 & 0 & 0 & 0 & -\frac{(1-\nu^2)r^4}{256\ell^4} \\ -3/4 & -3/4 & -1/2 & 0 & \end{array} \right) \right. \\
 & + 9 \frac{(1-\nu^2)r^4}{\ell^4} G_{04}^{20} \left( \begin{array}{cccc|c} 0 & 0 & 0 & 0 & -\frac{(1-\nu^2)r^4}{256\ell^4} \\ -7/4 & -7/4 & -3/2 & 0 & \end{array} \right) \\
 & \left. - \frac{(1-\nu^2)^2 r^8}{64\ell^8} G_{04}^{20} \left( \begin{array}{cccc|c} 0 & 0 & 0 & 0 & -\frac{(1-\nu^2)r^4}{256\ell^4} \\ -11/4 & -11/4 & -5/2 & 0 & \end{array} \right) \right], \tag{A.4}
 \end{aligned}$$

respectively. Similar expressions hold for the derivatives of  $w_2(r)$ , but the constants  $b_k$  are replaced by  $c_k$  ( $k = 0, 1, 2, 3$ ). The derivatives of  $w_3(r)$  with respect to  $r$  up to the third order are

$$w'_3(r) = \frac{m_0^+ \ell}{\sqrt{2}D} [d_1 \Sigma(r) + d_2 \Delta(r)], \tag{A.5}$$

$$w''_3(r) = \frac{m_0^+}{\sqrt{2}D} \left\{ -d_1 \left[ \sqrt{2} \operatorname{kei} \frac{r}{\ell} + \frac{\ell}{r} \Sigma(r) \right] + d_2 \left[ \sqrt{2} \operatorname{ker} \frac{r}{\ell} - \frac{\ell}{r} \Delta(r) \right] \right\}, \tag{A.6}$$

$$w'''_3(r) = \frac{m_0^+}{\sqrt{2}D\ell} \left\{ d_1 \left[ 2 \frac{\ell^2}{r^2} \Sigma(r) + \sqrt{2} \frac{\ell}{r} \operatorname{kei} \frac{r}{\ell} - \Delta(r) \right] + d_2 \left[ 2 \frac{\ell^2}{r^2} \Delta(r) - \sqrt{2} \frac{\ell}{r} \operatorname{ker} \frac{r}{\ell} + \Sigma(r) \right] \right\}, \tag{A.7}$$

respectively, where

$$\Sigma(r) = \operatorname{ker} \frac{r}{\ell} + \operatorname{kei} \frac{r}{\ell}, \quad \Delta(r) = \operatorname{ker} \frac{r}{\ell} - \operatorname{kei} \frac{r}{\ell}. \tag{A.8}$$

### Acknowledgements

Financial support from “Fondazione Cassa di Risparmio di Modena” within the framework of the International Research Project 2009–2010 “Modelling of crack propagation in complex materials” is gratefully acknowledged.

### References

[Abramowitz and Stegun 1964] M. Abramowitz and I. A. Stegun, *Handbook of mathematical functions with formulas, graphs, and mathematical tables*, National Bureau of Standards Applied Mathematics Series **55**, U.S. Government Printing Office, Washington, DC, 1964. Reprinted by Dover, New York, 1974.

[Barros and Figueiras 1998] J. A. O. Barros and J. A. Figueiras, “Experimental behaviour of fibre concrete slabs on soil”, *Mech. Cohes. Frict. Mater.* **3**:3 (1998), 277–290.

[Barros and Figueiras 1999] J. A. O. Barros and J. A. Figueiras, “Flexural behavior of SFRC: Testing and modeling”, *J. Mater. Civ. Eng. (ASCE)* **11**:4 (1999), 331–339.

[Barros and Figueiras 2001] J. A. O. Barros and J. A. Figueiras, “Model for the analysis of steel fibre reinforced concrete slabs on grade”, *Comput. Struct.* **79** (2001), 97–106.

[Baumann and Weisgerber 1983] R. Baumann and F. Weisgerber, “Yield-line analysis of slabs-on-grade”, *J. Struct. Eng. (ASCE)* **109**:7 (1983), 1553–1568.

[Belenkiy 2007] L. Belenkiy, “Upper-bound solutions for rigid-plastic plates and slabs on elastic foundation by the principle of stationary total energy”, *J. Struct. Eng. (ASCE)* **133**:2 (2007), 305–307.

[Bigoni and Piccolroaz 2004] D. Bigoni and A. Piccolroaz, “Yield criteria for quasibrittle and frictional materials”, *Int. J. Solids Struct.* **41**:11-12 (2004), 2855–2878.

[Bischoff et al. 2003] P. Bischoff, A. Valsangkar, and J. Irving, “Use of fibers and welded-wire reinforcement in construction of slabs on ground”, *Pract. Period. Struct. Des. Constr.* **8**:1 (2003), 41–46.

[Chen 2004] S. Chen, “Strength of steel fibre reinforced concrete ground slabs”, *Proc. Inst. Civ. Eng.* **157**:2 (2004), 157–163.

- [Concrete Society 2003] “Concrete industrial ground floors: A guide to design and construction”, Technical Report, Concrete Society, 2003, Available at <http://tinyurl.com/concrete-soc-TR34-2013>. Technical Report No. 34.
- [Falkner et al. 1995] H. Falkner, Z. Huang, and M. Teutsch, “Comparative study of plain and steel fiber reinforced concrete ground slabs”, *Concr. Int.* **17**:1 (1995), 45–51.
- [Gazetas 1981] G. C. Gazetas, “Ultimate behavior of continuous footings in tensionless contact with a three-parameter soil”, *J. Struct. Mech.* **9**:3 (1981), 339–362.
- [Gazetas and Tassios 1978] G. C. Gazetas and T. P. Tassios, “Elastic-plastic slabs on elastic foundation”, *J. Struct. Div. (ASCE)* **104**:4 (1978), 621–636.
- [Kocaturk 1997] T. Kocaturk, “Elastoplastic analysis of circular plates on elastoplastic foundation”, *J. Struct. Eng. (ASCE)* **123**:6 (1997), 808–815.
- [Lanzoni et al. 2014] L. Lanzoni, E. Radi, and A. Nobili, “Ultimate carrying capacity of elastic-plastic plates on Pasternak foundation”, *J. Appl. Mech. (ASME)* **81**:5 (2014), Article ID #051013.
- [Lardner 1969] T. J. Lardner, “Relations between  ${}_0F_3$  and Bessel functions”, *SIAM Rev.* **11** (1969), 69–72.
- [Losberg 1978] A. Losberg, “Pavements and slabs on grade with structurally active reinforcement”, *ACI J.* **75**:11 (1978), 647–657.
- [Luke 1969] Y. L. Luke, *The special functions and their approximations, I and II*, Academic Press, New York, 1969.
- [Meyerhof 1960] G. G. Meyerhof, “Bearing capacity of floating ice sheets”, *J. Eng. Mech. Div. (ASCE)* **86**:EM3 (1960), 113–145.
- [Meyerhof 1962] G. G. Meyerhof, “Load-carrying capacity of concrete pavements”, *J. Soil Mech. Found. Div.* **88**:SM3 (1962), 89–116.
- [Nobili et al. 2014] A. Nobili, E. Radi, and L. Lanzoni, “A cracked infinite Kirchhoff plate supported by a two-parameter elastic foundation”, *J. Eur. Ceram. Soc.* **34**:11 (2014), 2737–2744.
- [Piccolroaz and Bigoni 2009] A. Piccolroaz and D. Bigoni, “Yield criteria for quasibrittle and frictional materials: A generalization to surfaces with corners”, *Int. J. Solids Struct.* **46**:20 (2009), 3587–3596.
- [Poltronieri et al. 2014] F. Poltronieri, A. Piccolroaz, D. Bigoni, and S. Romero-Baivier, “A simple and robust elastoplastic constitutive model for concrete”, *Eng. Struct.* **60** (2014), 81–84.
- [Rao and Singh 1986] K. S. S. Rao and S. Singh, “Concentrated load-carrying capacity of concrete slabs on ground”, *J. Struct. Eng. (ASCE)* **112**:12 (1986), 2628–2645.
- [Roesler et al. 2004] J. R. Roesler, D. A. Lange, S. A. Altoubat, K. A. Rieder, and G. R. Ulreich, “Fracture of plain and fiber-reinforced concrete slabs under monotonic loading”, *J. Mater. Civ. Eng. (ASCE)* **16**:5 (2004), 452–460.
- [Roesler et al. 2006] J. R. Roesler, S. A. Altoubat, D. A. Lange, K. A. Rieder, and G. R. Ulreich, “Effect of synthetic fibers on structural behavior of concrete slabs-on-ground”, *ACI Mater. J.* **103**:1 (2006), 3–10.
- [Shentu et al. 1997] L. Shentu, D. Jiang, and C. T. T. Hsu, “Load-carrying capacity for concrete slabs on grade”, *J. Struct. Eng. (ASCE)* **123**:1 (1997), 95–103.
- [Silva et al. 2001] R. D. A. Silva, R. A. M. Silveira, and P. B. Gonçalves, “Numerical methods for analysis of plates on tensionless elastic foundations”, *Int. J. Solids Struct.* **38**:10–13 (2001), 2083–2100.
- [Sokól-Supel 1985] J. Sokól-Supel, “Elastoplastic bending of plates resting on elastic subgrade under rotational symmetry conditions”, *J. Struct. Mech.* **13**:3–4 (1985), 323–341.
- [Sokól-Supel 1988] J. Sokól-Supel, “Bending of metallic circular plates resting on elastic subgrade”, *Ing. Arch.* **58** (1988), 185–192.
- [Soutsos et al. 2012] M. N. Soutsos, T. T. Le, and A. P. Lampropoulos, “Flexural performance of fibre reinforced concrete made with steel and synthetic fibres”, *Construction and Building Materials* **36** (2012), 704–710.
- [Tekinalp 1957] B. Tekinalp, “Elastic-plastic bending of a built-in circular plate under a uniformly distributed load”, *J. Mech. Phys. Solids* **5**:2 (1957), 135–142.
- [Timoshenko and Woinowsky-Krieger 1959] S. Timoshenko and S. Woinowsky-Krieger, *Theory of plates and shells*, 2nd ed., McGraw-Hill, New York, 1959.

[Westergaard 1948] H. M. Westergaard, “New formulas for stresses in concrete pavements of airfields”, *Trans. ASCE* **113** (1948), 425–444.

Received 11 Dec 2013. Revised 21 Feb 2014. Accepted 10 Mar 2014.

ENRICO RADI: [eradi@unimore.it](mailto:eradi@unimore.it)

*Dipartimento di Scienze e Metodi dell’Ingegneria, Università di Modena e Reggio Emilia, Via Amendola 2, I-2 42122 Reggio Emilia, Italy*

PIETRO DI MAIDA: [pietro.dimaida@unimore.it](mailto:pietro.dimaida@unimore.it)

*Dipartimento di Scienze e Metodi dell’Ingegneria, Università di Modena e Reggio Emilia, Via Amendola 2, I-2 42122 Reggio Emilia, Italy*





## SOLUTION OF A RECEDING CONTACT PROBLEM USING AN ANALYTICAL METHOD AND A FINITE ELEMENT METHOD

ERDAL ÖNER, MURAT YAYLACI AND AHMET BİRİNCİ

In this study, a receding contact problem for two elastic layers supported by a Winkler foundation is handled using two different methods such as an analytical method and a finite element method. Firstly, the problem is solved analytically using linear elasticity theory. Then, in order to solve the same problem in a different way, a finite element model of the problem is created by ANSYS software, and finite element analysis of the problem is performed. The contact stresses and the contact areas at the interfaces between punch–Layer 2 and Layer 1–Layer 2 are obtained for both solutions, and it is shown that the finite element method indicates a good agreement with the analytical method.

### 1. Introduction

Although in the majority of cases the contact zone increases after the application of the load, there are others where the final contact zone is smaller than the original. This type of contact problem is termed as a receding contact problem [Garrido and Lorenzana 1998]. As a different point of view, a receding contact is one where the contact surface in the loaded configuration is contained within the initial contact surface [Johnson 1985]. The studies considering receding contact problems have been performed by various researchers in the literature [Stippes et al. 1962; Wilson and Goree 1967; Weitsman 1969; Margetson and Morland 1970; Chan and Tuba 1971; Keer et al. 1972; Ratwani and Erdogan 1973; Jing and Liao 1990; Porter and Hills 2002]. Furthermore, Zhu [1995] studied a finite element–mathematical programming method for elastoplastic contact problems with friction. Papadopoulos and Solberg [1998] investigated a novel Lagrange multiplier–based formulation for the finite element solution of the quasistatic two-body contact problem in the presence of finite motions and deformations. BEM solution of two-dimensional contact problems by weak application of contact conditions with nonconforming discretizations was carried out by Blázquez et al. [1998]. The mortar finite element method for contact problems was examined by Belgacem et al. [1998]. Guyot et al. [2000] presented coupling of finite elements and boundary elements methods for study of the frictional contact problem. Çömez et al. [2004] solved the plane symmetric double receding contact problem for a rigid stamp and two elastic layers having different elastic constants and heights. A residual type a posteriori error estimator for finite element approximations of a frictional contact problem for linearized elastic materials was analyzed by Bostan and Han [2006]. The plane problem of a frictionless receding contact between an elastic functionally graded layer and a homogeneous half-space when the two bodies were pressed together has been reported by El-Borgi et al. [2006]. Solberg et al. [2007] studied a family of simple two-pass dual formulations for the finite element solution of contact problems. Oysu [2007] investigated finite element and boundary element contact stress analysis with remeshing technique.

*Keywords:* finite element method, integral equation, receding contact, Winkler foundation.

A frictionless receding contact problem between an anisotropic elastic layer and an anisotropic elastic half-plane, when the two bodies were pressed together by means of a rigid circular stamp, was investigated by Kahya et al. [2007]. Rhimi et al. [2009] extended work of El-Borgi et al. [2006] in the sense that the receding contact problem was solved under axisymmetric conditions rather than plane stress or plane strain conditions. Kuss and Lebon [2009] carried out stress-based finite element methods for solving contact problems and comparisons between various solution methods. Finite element approximation to a contact problem for a nonlinear thermoviscoelastic beam was considered by Copetti and Fernández [2011]. A finite element method used in contact problems with dry friction was investigated by Pop et al. [2011]. Rhimi et al. [2011] focused on a double receding contact axisymmetric problem between a functionally graded layer and a homogeneous substrate. Zhang et al. [2012] reported a finite element model for 2-D elastic–plastic contact analysis of multiple Cosserat materials. Adıbelli et al. [2013] studied receding contact problem for a coated layer and a half-plane loaded by a rigid cylindrical stamp. A numerical approximation by the finite element method of a quasistatic, frictionless, unilateral contact problem between two thermoelastic bodies, in two dimensions, was examined by Copetti [2014]. An axisymmetric Hertzian contact problem of a rigid sphere pressing into an elastic half-space under cyclic loading was investigated by Kim and Jang [2014].

In this paper, a receding contact problem for two elastic layers supported by a Winkler foundation is solved using an analytical method and a finite element method. Thus, it is aimed to see whether FEM results are in an agreement with analytical results and how much the degree of approximation for the two methods is. For this purpose, the problem is firstly solved analytically using linear elasticity theory. Then, a finite element model of the problem is created by ANSYS software, and finite element analysis of the problem is performed. Finally, the contact stresses and the contact areas at the interfaces between punch–Layer 2 and Layer 1–Layer 2 are obtained for both solutions and the results obtained from two different methods are compared with each other.

## 2. Analytical solution of the problem

Consider the plane strain problem described by the insert in Figure 1, in which the  $x = 0$  plane is assumed to be a plane of symmetry. The problem consists of two infinitely long layers of thicknesses  $h_1$  and  $h_2$ . The layers are isotropic, homogeneous and linearly elastic. A concentrated load with magnitude  $P$  is subjected to the Layer 2 by means of a rigid circular punch. The Layer 1 is supported by a Winkler

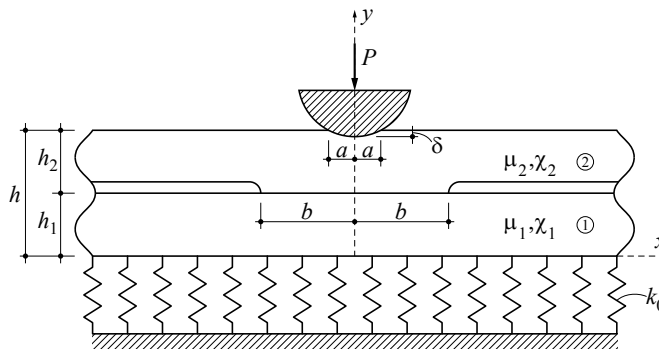


**Figure 1.** Geometry of the receding contact problem.

foundation. It is assumed that friction and gravity forces are neglected. Since the contact between the two bodies is assumed to be frictionless and layers are not adhered to each other, then only compressive normal tractions can be transmitted in the contact area. Where applicable, the germane quantities are reckoned per unit length in the  $z$  direction. Observing that  $x = 0$  is a plane symmetry, it is sufficient to consider the problem in the region  $0 \leq x < \infty$  only.

The stress and the displacement components needed for the application of the boundary conditions can be obtained using linear elasticity theory and integral transform technique as

$$u_i(x, y) = \frac{2}{\pi} \int_0^\infty \{ [A_i + B_i y] e^{-\alpha y} + [C_i + D_i y] e^{\alpha y} \} \sin(\alpha x) \, d\alpha, \tag{1}$$

$$v_i(x, y) = \frac{2}{\pi} \int_0^\infty \left\{ \left[ A_i + B_i \left( \frac{\chi_i}{\alpha} + y \right) \right] e^{-\alpha y} + \left[ -C_i + D_i \left( \frac{\chi_i}{\alpha} - y \right) \right] e^{\alpha y} \right\} \cos(\alpha x) \, d\alpha, \tag{2}$$

$$\frac{1}{2\mu_i} \sigma_{x_i}(x, y) = \frac{2}{\pi} \int_0^\infty \left\{ \left[ \alpha(A_i + B_i y) - \left( \frac{3 - \chi_i}{2} \right) B_i \right] e^{-\alpha y} + \left[ \alpha(C_i + D_i y) + \left( \frac{3 - \chi_i}{2} \right) D_i \right] e^{\alpha y} \right\} \times \cos(\alpha x) \, d\alpha, \tag{3}$$

$$\frac{1}{2\mu_i} \sigma_{y_i}(x, y) = \frac{2}{\pi} \int_0^\infty \left\{ - \left[ \alpha(A_i + B_i y) + \left( \frac{1 + \chi_i}{2} \right) B_i \right] e^{-\alpha y} + \left[ -\alpha(C_i + D_i y) + \left( \frac{1 + \chi_i}{2} \right) D_i \right] e^{\alpha y} \right\} \times \cos(\alpha x) \, d\alpha, \tag{4}$$

$$\frac{1}{2\mu_i} \tau_{xy_i}(x, y) = \frac{2}{\pi} \int_0^\infty \left\{ - \left[ \alpha(A_i + B_i y) + \left( \frac{\chi_i - 1}{2} \right) B_i \right] e^{-\alpha y} + \left[ \alpha(C_i + D_i y) - \left( \frac{\chi_i - 1}{2} \right) D_i \right] e^{\alpha y} \right\} \times \sin(\alpha x) \, d\alpha, \tag{5}$$

where  $\mathbf{u}$  and  $\mathbf{v}$  are the  $x$  and  $y$  components of the displacement vector, respectively;  $\sigma_x$ ,  $\sigma_y$  and  $\tau_{xy}$  are the stress components;  $\mu_i$  is shear modulus;  $\chi_i$  is an elastic constant and  $\chi_i = (3 - 4\nu_i)$  for plane strain; and  $\nu_i$  is Poisson's ratio ( $i = 1, 2$ ). The subscripts 1 and 2 refer to Layer 1 and Layer 2, respectively.  $A_i$ ,  $B_i$ ,  $C_i$  and  $D_i$  ( $i = 1, 2$ ) are the unknown coefficients that will be determined from continuity and boundary conditions prescribed on  $y = 0$ ,  $y = h_1$  and  $y = h$ .

The receding contact problem outlined above as shown in [Figure 1](#) must be solved under the following boundary conditions:

$$\sigma_{y_2}(x, h) = \begin{cases} -p_1(x) & (0 \leq x < a), \\ 0 & (a \leq x < \infty), \end{cases} \tag{6}$$

$$\tau_{xy_2}(x, h) = 0 \quad (0 \leq x < \infty), \tag{7}$$

$$\sigma_{y_2}(x, h_1) = \begin{cases} -p_2(x) & (0 \leq x < b), \\ 0 & (b \leq x < \infty), \end{cases} \tag{8}$$

$$\tau_{xy_2}(x, h_1) = 0 \quad (0 \leq x < \infty), \tag{9}$$

$$\sigma_{y_1}(x, h_1) = \sigma_{y_2}(x, h_1) \quad (0 \leq x < \infty), \tag{10}$$

$$\tau_{xy_1}(x, h_1) = 0 \quad (0 \leq x < \infty), \tag{11}$$

$$\tau_{xy_1}(x, 0) = 0 \quad (0 \leq x < \infty), \tag{12}$$

$$\sigma_{y_1}(x, 0) = k_0 v_1(x, 0) \quad (0 \leq x < \infty), \tag{13}$$

$$v_2(x, h) = F(x) \quad \text{or} \quad \frac{\partial}{\partial x} v_2(x, h) = f(x) \quad (0 \leq x < a), \tag{14}$$

$$\frac{\partial}{\partial x} [v_2(x, h_1) - v_1(x, h_1)] = 0 \quad (0 \leq x < b), \tag{15}$$

where  $a$  is the half-width of the contact area between rigid circular punch and Layer 2;  $b$  is the half-width of the contact area between Layer 1 and Layer 2;  $p_1(x)$  is the unknown contact stress under the rigid circular punch;  $p_2(x)$  is the unknown contact stress between Layer 1 and Layer 2;  $k_0$  is the stiffness of the Winkler foundation; and  $f(x)$  is the derivative of the function  $F(x)$  that characterizes surface profile of the rigid punch. In the case of circular punch,  $f(x)$  can be written as

$$F(x) = h - \delta - [(R^2 - x^2)^{1/2} - R], \tag{16}$$

$$f(x) = \frac{d}{dx} [F(x)] = -\frac{x}{(R^2 - x^2)^{1/2}}, \tag{17}$$

where  $\delta$  is the maximum displacement that occurs on the layer under the punch at the axis of symmetry ( $x = 0$ ) and  $R$  is the radius of the rigid circular punch. By making use of the boundary conditions (6)–(13), eight of the unknown coefficients  $A_i, B_i, C_i$  and  $D_i$  ( $i = 1, 2$ ) appearing in (1)–(5) may be obtained in terms of the unknown functions  $p_1(x)$  and  $p_2(x)$ .

By substituting these coefficients into (14) and (15), after some routine manipulations and using the symmetry conditions  $p_1(x) = p_1(-x)$  and  $p_2(x) = p_2(-x)$  and replacing  $\omega = \alpha h$  and  $r = h_1/h$ , the system of integral equations for  $p_1(x)$  and  $p_2(x)$  is obtained as

$$\frac{1}{\pi} \int_{-a}^a \left[ \frac{1}{t-x} + k_1(x, t) \right] p_1(t) dt + \frac{1}{\pi} \int_{-b}^b [k_2(x, t)] p_2(t) dt = -\frac{4\mu_2}{(1 + \chi_2)} f(x), \tag{18}$$

$$\frac{1}{\pi} \int_{-b}^b \left[ \frac{1}{t-x} + k_3(x, t) \right] p_2(t) dt + \frac{1}{\pi} \int_{-a}^a [k_4(x, t)] p_1(t) dt = 0, \tag{19}$$

where

$$k_1(x, t) = \int_0^\infty \left[ \frac{4}{\Delta} K_{11} K_{12} - 1 \right] \sin \frac{\omega(t-x)}{h} d\omega, \tag{20}$$

$$k_2(x, t) = -8 \int_0^\infty \frac{e^{-\omega} e^{-\omega r}}{\Delta} K_{11} K_{13} \sin \frac{\omega(t-x)}{h} d\omega, \tag{21}$$

$$k_3(x, t) = \int_0^\infty \left\{ -\frac{4}{(1+m)} \frac{1}{\Delta} \left\{ K_{12}(-K_{11}) + m K_{14} \left[ -4 \frac{\omega}{h} K_{11A} + K^{**} (1 + e^{4\omega r} - 2e^{2\omega r}) \right] \right\} - 1 \right\} \times \sin \frac{\omega(t-x)}{h} d\omega, \tag{22}$$

$$k_4(x, t) = -\frac{8}{(1+m)} \int_0^\infty \frac{e^{-\omega} e^{-\omega r}}{\Delta} K_{11} K_{13} \sin \frac{\omega(t-x)}{h} d\omega, \tag{23}$$

$$\Delta = 4K_{11}K_{14}, \tag{24}$$

$$K_{11} = K^{**}K_{11A} + 4(\omega/h)K_{11B}, \tag{25}$$

$$K_{12} = e^{-4\omega r} - e^{-4\omega} + e^{-2\omega}e^{-2\omega r}(4\omega - 4\omega r), \tag{26}$$

$$K_{13} = e^{-2\omega r}(1 + \omega - \omega r) + e^{-2\omega}(-1 + \omega - \omega r), \tag{27}$$

$$K_{14} = e^{-4\omega r} + e^{-4\omega} - 2e^{-2\omega}e^{-2\omega r}(1 + 2\omega^2 + 2\omega^2r^2 - 4\omega^2r), \tag{28}$$

$$K_{11A} = 1 - 4\omega r e^{2\omega r} - e^{4\omega r}, \tag{29}$$

$$K_{11B} = -1 + e^{2\omega r}(2 + 4\omega^2r^2 - e^{2\omega r}), \tag{30}$$

$$m = \frac{(1 + \chi_1)\mu_2}{(1 + \chi_2)\mu_1}, \tag{31}$$

$$K^{**} = k(1 + \chi_1), \tag{32}$$

$$k = \frac{k_0}{\mu_1}. \tag{33}$$

In the system of singular integral equations (18) and (19), in addition to the contact stresses  $p_1(x)$  and  $p_2(x)$ , the half-width of the contact areas  $a$  and  $b$  are also unknown. These two unknowns  $a$  and  $b$  are determined from the equilibrium conditions, which can be written as

$$\int_{-a}^a p_1(t) dt = P, \quad \int_{-b}^b p_2(t) dt = P. \tag{34}$$

We will use  $(x_1, t_1)$  to denote the variables  $(x, t)$  on the boundary  $y = h$ , and likewise  $(x_2, t_2)$  on the boundary  $y = h_1$ . We also define the following dimensionless quantities:

$$x_1 = ar_1, \quad t_1 = as_1, \quad dt_1 = a ds_1, \quad x_2 = br_2, \quad t_2 = bs_2, \quad dt_2 = b ds_2, \\ g_1(s_1) = \frac{p_1(t_1)}{P/h}, \quad g_2(s_2) = \frac{p_2(t_2)}{P/h}, \tag{35}$$

$$M_1(r_1, s_1) = k_1(x_1, t_1), \quad M_2(r_1, s_2) = k_2(x_1, t_2), \quad M_3(r_2, s_2) = k_3(x_2, t_2), \quad M_4(r_2, s_1) = k_4(x_2, t_1).$$

By substituting (35) into the system of integral equations (18) and (19) and equilibrium conditions (34), the system of integral equations and equilibrium conditions may be obtained as

$$\frac{1}{\pi} \int_{-1}^1 \left[ \frac{1}{s_1 - r_1} + \frac{a}{h} M_1(r_1, s_1) \right] g_1(s_1) ds_1 + \frac{1}{\pi} \frac{b}{h} \int_{-1}^1 M_2(r_1, s_2) g_2(s_2) ds_2 = -\frac{4\mu_2}{(1 + \chi_2)P/h} f(r_1), \tag{36}$$

$$\frac{1}{\pi} \int_{-1}^1 \left[ \frac{1}{s_2 - r_2} + \frac{b}{h} M_3(r_2, s_2) \right] g_2(s_2) ds_2 + \frac{1}{\pi} \frac{a}{h} \int_{-1}^1 M_4(r_2, s_1) g_1(s_1) ds_1 = 0, \tag{37}$$

$$\frac{a}{h} \int_{-1}^1 g_1(s_1) ds_1 = 1, \quad \frac{b}{h} \int_{-1}^1 g_2(s_2) ds_2 = 1. \tag{38}$$

Since (36)–(37) have no closed-form solution, an effective numerical solution may be obtained by using [Erdogan and Gupta 1972]. This method is a standard and necessary step in handling the integral

equation part of the solution. So one may notice that because of the smooth contact at the end points  $a$  and  $b$ , the contact stresses  $p_1(x)$  and  $p_2(x)$  are zero at the end points, and the index of the integral equations (36) and (37) is “ $-1$ ”. Let

$$g_1(s_1) = G_1(s_1)(1 - s_1^2)^{1/2} \quad (-1 < s_1 < 1), \tag{39}$$

$$g_2(s_2) = G_2(s_2)(1 - s_2^2)^{1/2} \quad (-1 < s_2 < 1). \tag{40}$$

Using the appropriate Gauss–Chebyshev integration formula, (36)–(38) become

$$\sum_{k=1}^N \frac{1 - s_k^2}{N + 1} \left\{ G_1(s_{k1}) \left[ \frac{1}{s_{k1} - r_{i1}} + \frac{a}{h} M_1(r_{i1}, s_{k1}) \right] + \frac{b}{h} M_2(r_{i1}, s_{k2}) G_2(s_{k2}) \right\} = -\frac{4\mu_2}{(1 + \chi_2)P/h} f(r_{i1}), \tag{41}$$

$$\sum_{k=1}^N \frac{1 - s_k^2}{N + 1} \left\{ G_2(s_{k2}) \left[ \frac{1}{s_{k2} - r_{i2}} + \frac{b}{h} M_3(r_{i2}, s_{k2}) \right] + \frac{a}{h} M_4(r_{i2}, s_{k1}) G_1(s_{k1}) \right\} = 0, \tag{42}$$

$$\frac{a}{h} \sum_{k=1}^N \frac{1 - s_k^2}{N + 1} G_1(s_{k1}) = \frac{1}{\pi}, \quad \frac{b}{h} \sum_{k=1}^N \frac{1 - s_k^2}{N + 1} G_2(s_{k2}) = \frac{1}{\pi}, \tag{43}$$

where

$$s_k = \cos\left(\frac{k\pi}{N + 1}\right) \quad (k = 1, \dots, N), \tag{44}$$

$$r_i = \cos\left(\frac{2i - 1}{N + 1} \frac{\pi}{2}\right) \quad (i = 1, \dots, N + 1). \tag{45}$$

As the value of  $N$  is increased, more accurate results can be obtained. Hence, the value of  $N$  is chosen as 60 in this study because, after a value of  $N = 60$ , change in the results is very small and insignificant. It can be seen that the extra equations in (41) and (42) correspond to the consistency condition of the original integral equations (36) and (37). It can also be shown that the  $(N/2 + 1)$ -th equations in (41) and (42) are automatically satisfied [Erdogan and Gupta 1972]. Thus, (41)–(43) give  $2N + 2$  algebraic equations to determine the  $2N + 2$  unknowns  $G_1(s_{k1})$ ,  $G_2(s_{k2})$  ( $k = 1, \dots, N$ ),  $a$  and  $b$ . The system of equations are linear in  $G_1(s_{k1})$  and  $G_2(s_{k2})$  but highly nonlinear in  $a$  and  $b$ . Therefore, an interpolation and iteration scheme had to be used to obtain these two unknowns. In this iterative procedure, firstly  $2N$  equations ( $i = 1, \dots, N/2, N/2 + 2, \dots, N + 1$ ) are chosen from (41)–(42). After predicting values for  $a$  and  $b$ ,  $G_1(s_{k1})$  and  $G_2(s_{k2})$  are calculated using previously determined ( $2N$ ) equations. If the chosen  $a$  and  $b$  and obtained  $G_1(s_{k1})$  and  $G_2(s_{k2})$  values ensure (43), the solution would have been found. Otherwise,  $G_1(s_{k1})$  and  $G_2(s_{k2})$  values are recalculated after predicting new  $a$  and  $b$  values.

### 3. The finite-element analysis of the problem

This section describes our FEM analysis of the receding contact problem using ANSYS Multiphysics. The problem is considered as a two-dimensional contact problem, and the material of the layers are assumed elastic and isotropic. The physical system under consideration exhibits symmetry in geometry, material properties and loading. It is computationally advantageous to model only a representative portion. The geometry and the applied load are shown schematically in Figure 2, and the deformed



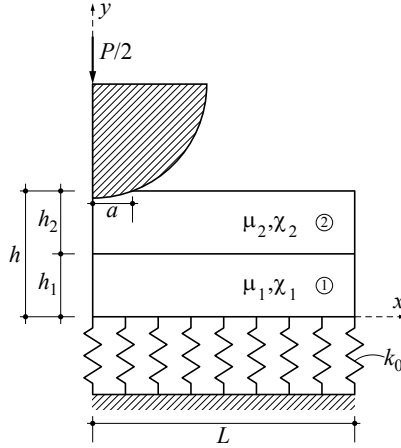


**Figure 2.** The geometry for the analysis.

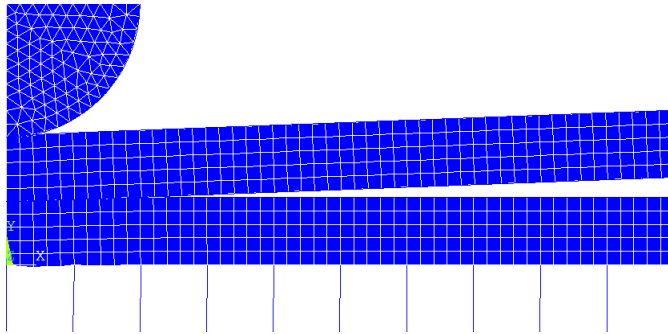


**Figure 3.** Deformed geometry for the preliminary analysis.

geometry for the preliminary analysis is shown in Figure 3. In the study, two-dimensional solid elements (PLANE183) are used to model the layers. The PLANE183 element is defined by six nodes having two degrees of freedom at each node: translations in the nodal  $x$  and  $y$  directions. The element may be used as a plane element (plane stress, plane strain and generalized plane strain). The Winkler foundation is modeled by a linear spring element (COMBIN14). The COMBIN14 element or the longitudinal element spring-damper option is an uniaxial tension–compression element with up to two degrees of freedom at each node: translations in the nodal  $x$  and  $y$  directions. No bending or torsion is considered [Al-Azzawi et al. 2010].

The contact region is meshed by surface-to-surface CONTA172 and TARGE169 contact elements. CONTA172 is used to represent that of the mechanical contact analysis. The target surface, defined by TARGE169, was therefore used to represent 2-D “target” surfaces for the associated contact elements CONTA172. Plane strain finite elements are used for the meshing of the entire geometry. Frictionless surface-to-surface contact elements are used to model the interaction between the contact surfaces, and the augmented Lagrangian method is used as the contact algorithm. The preliminary analysis is meshed with 4435 elements and 8444 nodes, and the contacting line is meshed with 75 elements.

### 4. Results and discussion

This section presents some of the calculated results obtained from analytical and FEM solution of the receding contact problem for various dimensionless quantities such as  $R/h$ ,  $\mu_2/(P/h)$ ,  $\mu_2/\mu_1$  and  $k = k_0/\mu_1$ . Also, in this section, the results obtained from the analytical method are compared with those of the finite element method.

Table 1 shows variation of half-widths of the contact areas with radius of punch ( $R/h$ ). It is seen from Table 1 that half-widths of the contact areas increase with increasing radius of punch. This is an expected result. Variation of half-widths of the contact areas with load ratio  $\mu_2/(P/h)$  is given in Table 2. Examination of Table 2 indicates that half-widths of the contact areas decrease with increasing of the load ratio  $\mu_2/(P/h)$ .

Table 3 illustrates the effect of  $\mu_2/\mu_1$  on the half-widths of the contact areas. As seen in Table 3, increasing the value of  $\mu_2/\mu_1$  results in an increase of half-widths of the contact areas. Variation of half-widths of the contact areas with  $k = k_0/\mu_1$  is presented in Table 4. This table demonstrates that, as the stiffness of the Winkler foundation increases, half-widths of the contact areas decrease. Additionally, when comparing the analytical and FEM results, it is seen from results that the finite element method

Parameter	$R/h = 50$		$R/h = 100$		$R/h = 250$		$R/h = 500$	
	$a/h$	$b/h$	$a/h$	$b/h$	$a/h$	$b/h$	$a/h$	$b/h$
Analytical	0.5057	0.7662	0.7079	0.9018	1.0614	1.1882	1.4034	1.4956
FEM	0.500	0.755	0.700	0.900	1.050	1.200	1.400	1.500
Error (%)	1.13	1.15	1.12	0.19	1.07	0.99	0.24	0.29

**Table 1.** Variation of half-widths of the contact areas with radius of punch ( $R/h$ ) ( $\chi_1 = \chi_2 = 2$ ,  $\mu_2/(P/h) = 100$ ,  $h_1/h = 0.5$ ,  $\mu_2/\mu_1 = 0.5$ ,  $k = k_0/\mu_1 = 2$ ).

Parameter	$\mu_2/(P/h) = 50$		$\mu_2/(P/h) = 100$		$\mu_2/(P/h) = 200$		$\mu_2/(P/h) = 500$	
	$a/h$	$b/h$	$a/h$	$b/h$	$a/h$	$b/h$	$a/h$	$b/h$
Analytical	1.199	1.3707	0.8477	1.0959	0.5735	0.9253	0.3365	0.8236
FEM	1.200	1.375	0.850	1.100	0.575	0.925	0.3375	0.825
Error (%)	0.08	0.31	0.27	0.37	0.25	0.03	0.3	0.17

**Table 2.** Variation of half-widths of the contact areas with load ratio  $\mu_2/(P/h)$  ( $\chi_1 = \chi_2 = 2$ ,  $R/h = 100$ ,  $h_1/h = 0.5$ ,  $\mu_2/\mu_1 = 0.5$ ,  $k = k_0/\mu_1 = 0.5$ ).

Parameter	$\mu_2/\mu_1 = 0.1$		$\mu_2/\mu_1 = 0.5$		$\mu_2/\mu_1 = 2$		$\mu_2/\mu_1 = 5$	
	$a/h$	$b/h$	$a/h$	$b/h$	$a/h$	$b/h$	$a/h$	$b/h$
Analytical	0.6013	0.7445	0.7079	0.9018	0.9868	1.2616	1.3112	1.6763
FEM	0.600	0.750	0.700	0.900	0.9875	1.2625	1.3125	1.675
Error (%)	0.22	0.74	1.12	0.19	0.07	0.07	0.1	0.08

**Table 3.** Variation of half-widths of the contact areas with  $\mu_2/\mu_1$  ( $\chi_1 = \chi_2 = 2$ ,  $\mu_2/(P/h) = 100$ ,  $R/h = 100$ ,  $h_1/h = 0.5$ ,  $k = k_0/\mu_1 = 2$ ).

Parameter	$k = 0.5$		$k = 1$		$k = 2$		$k = 4$	
	$a/h$	$b/h$	$a/h$	$b/h$	$a/h$	$b/h$	$a/h$	$b/h$
Analytical	0.8477	1.0959	0.7622	0.9791	0.7079	0.9018	0.6743	0.8528
FEM	0.850	1.100	0.7625	0.975	0.700	0.900	0.675	0.850
Error (%)	0.27	0.37	0.04	0.42	1.12	0.19	0.1	0.33

**Table 4.** Variation of half-widths of the contact areas with  $k = k_0/\mu_1$  ( $\chi_1 = \chi_2 = 2$ ,  $\mu_2/(P/h) = 100$ ,  $R/h = 100$ ,  $h_1/h = 0.5$ ,  $\mu_2/\mu_1 = 0.5$ ).

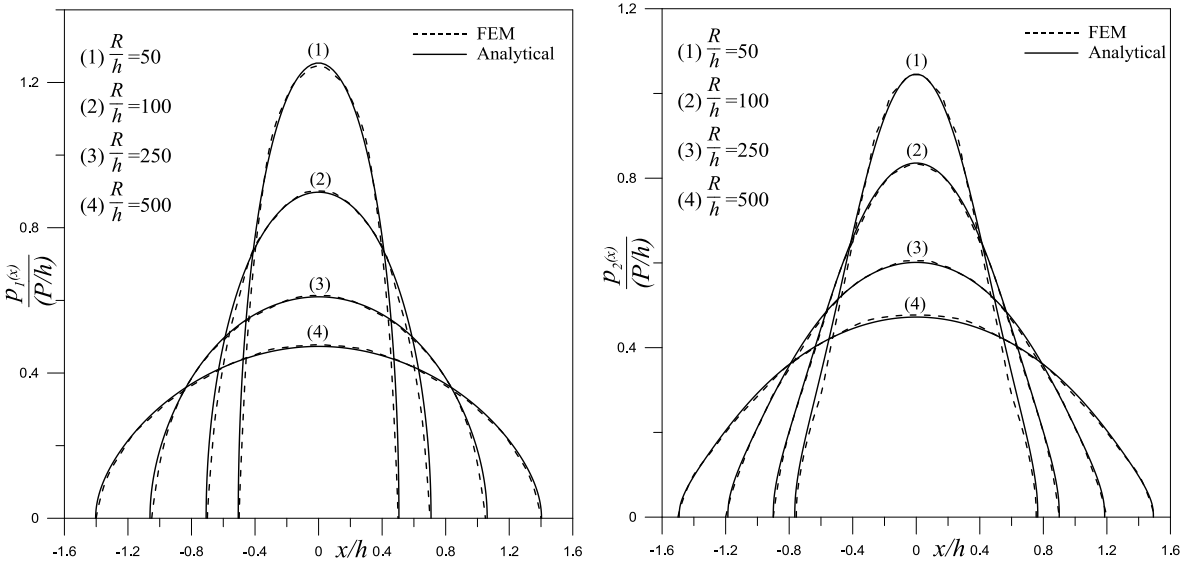


**Figure 4.** Normalized contact stress distribution at the punch–Layer 2 interface (left) and Layer 1–Layer 2 interface (right) for various values of  $R/h$  ( $\chi_1 = \chi_2 = 2$ ,  $\mu_2/(P/h) = 100$ ,  $h_1/h = 0.5$ ,  $\mu_2/\mu_1 = 0.5$ ,  $k = 2$ ).

indicates a good agreement with the analytical method disagree by 0.03%–1.15%. It can be stated that these values are at an acceptable level.

Figure 4 shows normalized contact stress distributions at the interfaces between the rigid punch–Layer 2 and between Layer 1–Layer 2 for various values of  $R/h$ . As seen in this figure, the normalized contact stress distributions decrease at both interfaces with increasing of  $R/h$ . The effect of the load ratio  $\mu_2/(P/h)$  on the normalized contact stress distributions at the interfaces between the rigid punch–Layer 2 and between Layer 1–Layer 2 is presented in Figure 5. It can be concluded from that figure that increasing the value of  $\mu_2/(P/h)$  results in an increase of normalized contact stress distributions at both interfaces. The normalized contact stress distributions at the interfaces between the rigid punch–Layer 2 and between Layer 1–Layer 2 for various values of  $\mu_2/\mu_1$  appear in Figure 6. It is seen there that, as  $\mu_2/\mu_1$  increases, the normalized contact stress distributions at both interfaces decrease. Figure 7 shows normalized contact stress distributions at the interfaces between the rigid punch–Layer 2 and between Layer 1–Layer 2 for various values of  $k = k_0/\mu_1$ . They demonstrate that the normalized contact stress distributions at the interfaces between the rigid punch–Layer 2 and between Layer 1–Layer 2 increase

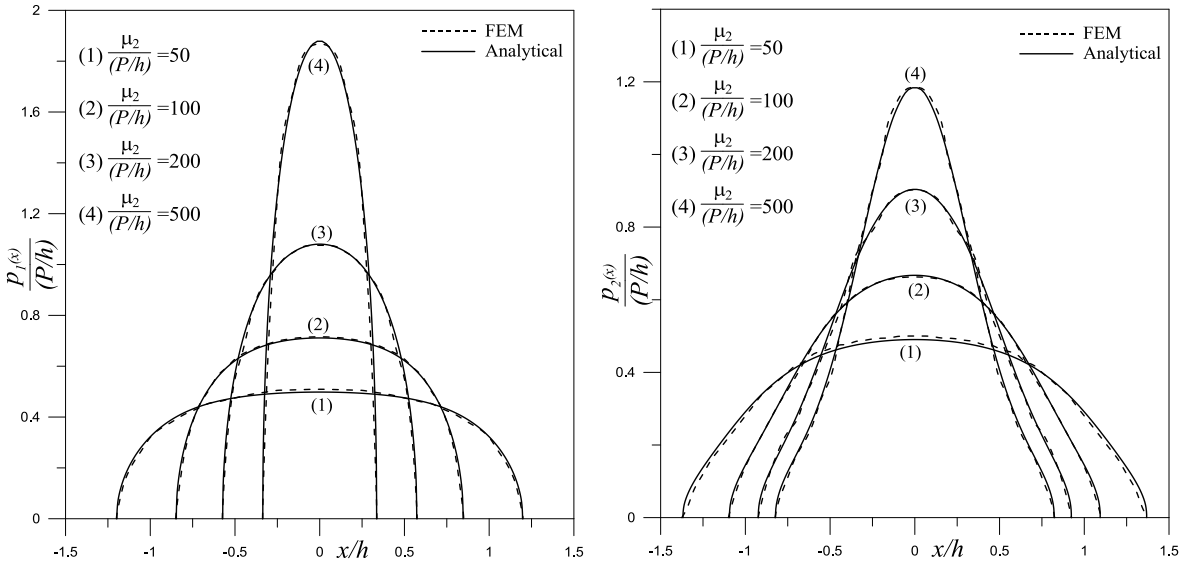


**Figure 5.** Normalized contact stress distribution at the punch–Layer 2 interface (left) and Layer 1–Layer 2 interface (right) for various values of  $\mu_2/(P/h)$  ( $\chi_1 = \chi_2 = 2$ ,  $R/h = 100$ ,  $h_1/h = 0.5$ ,  $\mu_2/\mu_1 = 0.5$ ,  $k = 2$ ).

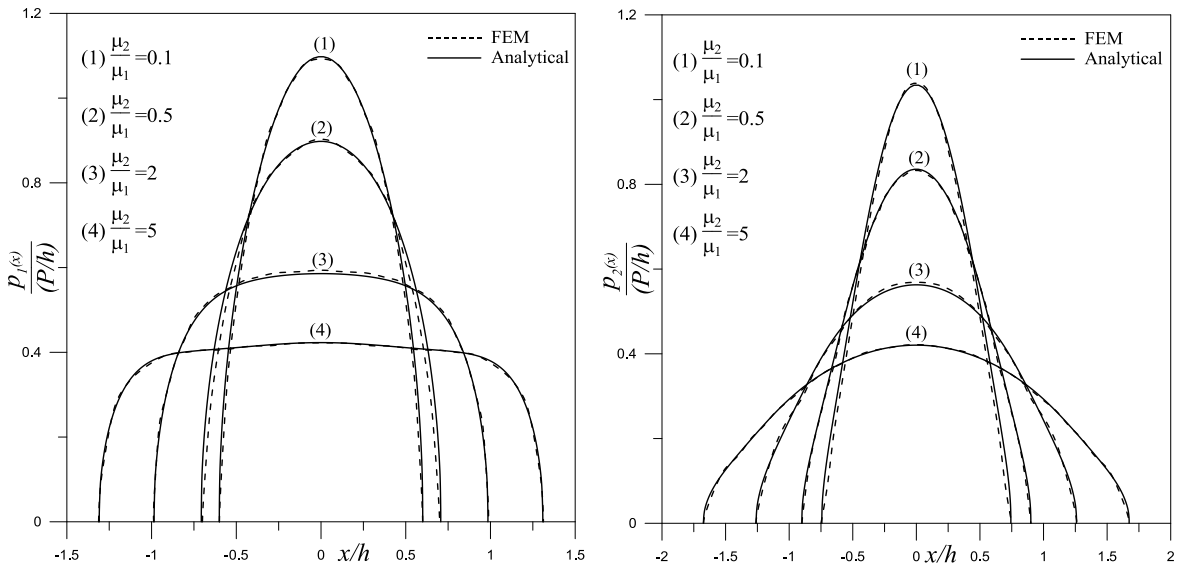


**Figure 6.** Normalized contact stress distribution at the punch–Layer 2 interface (left) and Layer 1–Layer 2 interface (right) for various values of  $\mu_2/\mu_1$  ( $\chi_1 = \chi_2 = 2$ ,  $R/h = 100$ ,  $\mu_2/(P/h) = 100$ ,  $h_1/h = 0.5$ ,  $k = 2$ ).

with increasing of the stiffness of the Winkler foundation. All figures show that the normalized contact stress distributions at the interfaces between the rigid punch–Layer 2 and between Layer 1–Layer 2 are symmetrical and their maximum values occur at the axis of symmetry. Also, the values of the

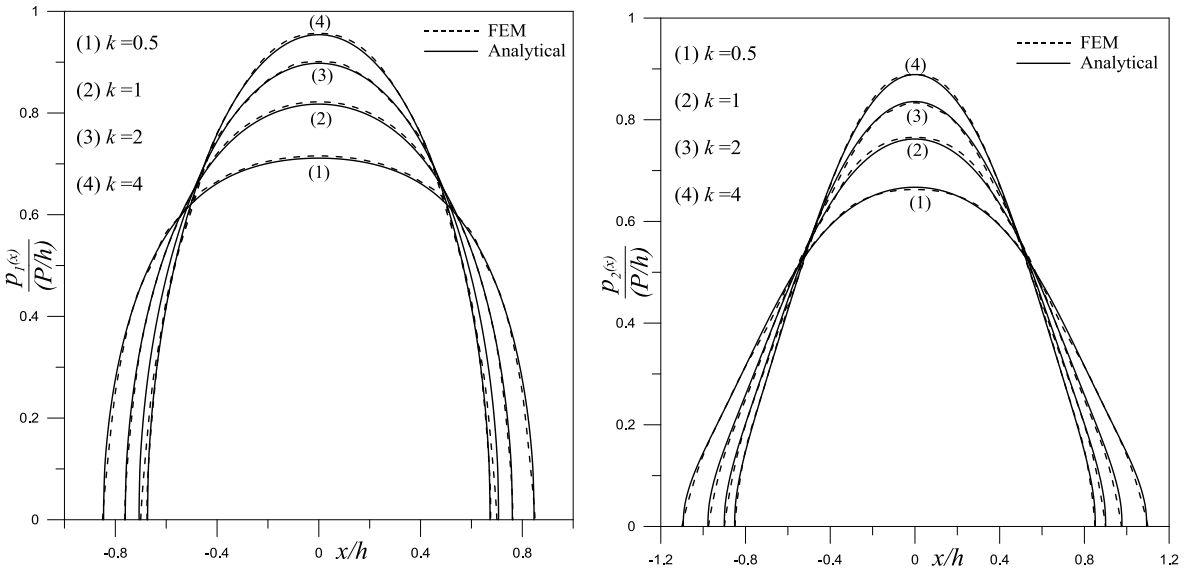


**Figure 7.** Normalized contact stress distribution at the punch–Layer 2 interface (left) and Layer 1–Layer 2 interface (right) for various values of  $k = k_0/\mu_1$  ( $\chi_1 = \chi_2 = 2$ ,  $R/h = 100$ ,  $\mu_2/(P/h) = 100$ ,  $h_1/h = 0.5$ ,  $\mu_2/\mu_1 = 0.5$ ).

normalized contact stresses are zero at the end contact points  $(-a, +a)$  and  $(-b, +b)$ . This result shows that boundary conditions given in the definition of the problem are provided. Finally, similar to results of contact areas, a good agreement is found between the analytical method and FEM.

### 5. Conclusions

The presented study aims to solve a receding contact problem for two elastic layers supported by a Winkler foundation using two different methods such as an analytical method and a FEM. For this purpose, first of all, the problem is solved analytically using linear elasticity theory. Then, an initial finite element model of the problem is developed by ANSYS software and finite element analysis is performed. Finally, the results obtained from finite element analysis are compared with analytical results. The results of the all analyses described in this paper allow the following conclusions to be drawn:

- Half-widths of the contact areas increase with increasing of  $R/h$  and  $\mu_2/\mu_1$ . On the contrary, they decrease with increasing of  $\mu_2/(P/h)$  and  $k = k_0/\mu_1$ .
- Normalized contact stress distributions at the interfaces between the rigid punch–Layer 2 and Layer 1–Layer 2 increase with increasing of  $\mu_2/(P/h)$  and  $k = k_0/\mu_1$ . But increasing the values of  $R/h$  and  $\mu_2/\mu_1$  result in a decrease of normalized contact stress distributions at both interfaces.
- Normalized contact stress distributions at the interfaces between the rigid punch–Layer 2 and between Layer 1–Layer 2 are symmetrical and their maximum values occur at the axis of symmetry. Also, the values of normalized contact stresses are zero at the end contact points  $(-a, +a)$  and  $(-b, +b)$ .

- It is seen from all numerical results that finite element solution indicates a good agreement with analytical solution.

## References

- [Adibelli et al. 2013] H. Adibelli, I. Çömez, and R. Erdöl, “Receding contact problem for a coated layer and a half-plane loaded by a rigid cylindrical stamp”, *Arch. Mech. (Arch. Mech. Stos.)* **65**:3 (2013), 219–236.
- [Al-Azzawi et al. 2010] A. A. Al-Azzawi, A. H. Mahdy, and O. S. Farhan, “Finite element analysis of deep beams on nonlinear elastic foundations”, *J. Serbian Soc. Comput. Mech.* **4**:2 (2010), 13–42.
- [Belgacem et al. 1998] F. B. Belgacem, P. Hild, and P. Laborde, “The mortar finite element method for contact problems”, *Math. Comput. Model.* **28**:4–8 (1998), 263–271.
- [Blázquez et al. 1998] A. Blázquez, F. París, and V. Mantič, “BEM solution of two-dimensional contact problems by weak application of contact conditions with non-conforming discretizations”, *Int. J. Solids Struct.* **35**:24 (1998), 3259–3278.
- [Bostan and Han 2006] V. Bostan and W. Han, “A posteriori error analysis for finite element solutions of a frictional contact problem”, *Comput. Methods Appl. Mech. Eng.* **195**:9-12 (2006), 1252–1274.
- [Chan and Tuba 1971] S. K. Chan and I. S. Tuba, “A finite element method for contact problems of solid bodies — part I: theory and validation”, *Int. J. Mech. Sci.* **13**:7 (1971), 615–625.
- [Çömez et al. 2004] I. Çömez, A. Birinci, and R. Erdöl, “Double receding contact problem for a rigid stamp and two elastic layers”, *Eur. J. Mech. A Solids* **23**:2 (2004), 301–309.
- [Copetti 2014] M. I. M. Copetti, “A penalty-finite element approximation to a Signorini two-body contact problem in thermoelasticity”, *Appl. Math. Comput.* **234** (2014), 293–308.
- [Copetti and Fernández 2011] M. I. M. Copetti and J. R. Fernández, “Finite element approximation to a contact problem for a nonlinear thermoviscoelastic beam”, *J. Math. Anal. Appl.* **383**:2 (2011), 506–521.
- [El-Borgi et al. 2006] S. El-Borgi, R. Abdelmoula, and L. Keer, “A receding contact plane problem between a functionally graded layer and a homogeneous substrate”, *Int. J. Solids Struct.* **43**:3–4 (2006), 658–674.
- [Erdogan and Gupta 1972] F. Erdogan and G. D. Gupta, “On the numerical solution of singular integral equations”, *Quart. Appl. Math.* **29** (1972), 525–534.
- [Garrido and Lorenzana 1998] J. A. Garrido and A. Lorenzana, “Receding contact problem involving large displacements using the BEM”, *Eng. Anal. Bound. Elem.* **21**:4 (1998), 295–303.
- [Guyot et al. 2000] N. Guyot, F. Kosior, and G. Maurice, “Coupling of finite elements and boundary elements methods for study of the frictional contact problem”, *Comput. Methods Appl. Mech. Eng.* **181**:1–3 (2000), 147–159.
- [Jing and Liao 1990] H.-S. Jing and M.-L. Liao, “An improved finite element scheme for elastic contact problems with friction”, *Comput. Struct.* **35**:5 (1990), 571–578.
- [Johnson 1985] K. L. Johnson (editor), *Contact mechanics*, Cambridge University Press, 1985.
- [Kahya et al. 2007] V. Kahya, T. S. Ozsahin, A. Birinci, and R. Erdöl, “A receding contact problem for an anisotropic elastic medium consisting of a layer and a half plane”, *Int. J. Solids Struct.* **44**:17 (2007), 5695–5710.
- [Keer et al. 1972] L. M. Keer, J. Dundurs, and K. C. Tsai, “Problems involving a receding contact between a layer and a half space”, *J. Appl. Mech. (ASME)* **39**:4 (12/01 1972), 1115–1120.
- [Kim and Jang 2014] J. H. Kim and Y. H. Jang, “Frictional Hertzian contact problems under cyclic loading using static reduction”, *Int. J. Solids Struct.* **51**:1 (2014), 252–258.
- [Kuss and Lebon 2009] F. Kuss and F. Lebon, “Stress based finite element methods for solving contact problems: comparisons between various solution methods”, *Adv. Eng. Software* **40**:8 (2009), 697–706.
- [Margetson and Morland 1970] J. Margetson and L. W. Morland, “Separation of smooth circular inclusions from elastic and viscoelastic plates subjected to uniaxial tension”, *J. Mech. Phys. Solids* **18**:4 (1970), 295–309.
- [Oysu 2007] C. Oysu, “Finite element and boundary element contact stress analysis with remeshing technique”, *Appl. Math. Model.* **31**:12 (2007), 2744–2753.

- [Papadopoulos and Solberg 1998] P. Papadopoulos and J. M. Solberg, “A Lagrange multiplier method for the finite element solution of frictionless contact problems”, *Math. Comput. Model.* **28**:4–8 (1998), 373–384. Recent Advances in Contact Mechanics.
- [Pop et al. 2011] N. Pop, H. Cioban, and A. Horvat-Marc, “Finite element method used in contact problems with dry friction”, *Comput. Mater. Sci.* **50**:4 (2011), 1283–1285.
- [Porter and Hills 2002] M. I. Porter and D. A. Hills, “Note on the complete contact between a flat rigid punch and an elastic layer attached to a dissimilar substrate”, *Int. J. Mech. Sci.* **44**:3 (2002), 509–520.
- [Ratwani and Erdogan 1973] M. Ratwani and F. Erdogan, “On the plane contact problem for a frictionless elastic layer”, *Int. J. Solids Struct.* **9**:8 (1973), 921–936.
- [Rhimmi et al. 2009] M. Rhimmi, S. El-Borgi, W. B. Saïd, and F. B. Jemaa, “A receding contact axisymmetric problem between a functionally graded layer and a homogeneous substrate”, *Int. J. Solids Struct.* **46**:20 (2009), 3633–3642.
- [Rhimmi et al. 2011] M. Rhimmi, S. El-Borgi, and N. Lajnef, “A double receding contact axisymmetric problem between a functionally graded layer and a homogeneous substrate”, *Mech. Mater.* **43**:12 (2011), 787–798.
- [Solberg et al. 2007] J. M. Solberg, R. E. Jones, and P. Papadopoulos, “A family of simple two-pass dual formulations for the finite element solution of contact problems”, *Comput. Methods Appl. Mech. Eng.* **196**:4–6 (2007), 782–802.
- [Stippes et al. 1962] M. Stippes, H. B. Wilson, Jr., and F. N. Krull, “A contact stress problem for a smooth disk in an infinite plate”, pp. 799–806 in *Proceedings of the Fourth U.S. National Congress of Applied Mechanics* (Berkeley, 1962), vol. 2, Amer. Soc. Mech. Engrs., New York, 1962.
- [Weitsman 1969] Y. Weitsman, “On the unbonded contact between plates and an elastic half space”, *J. Appl. Mech. (ASME)* **36**:2 (06/01 1969), 198–202.
- [Wilson and Goree 1967] H. B. Wilson, Jr. and J. G. Goree, “Axisymmetric contact stresses about a smooth elastic sphere in an infinite solid stressed uniformly at infinity”, *J. Appl. Mech. (ASME)* **34**:4 (12/01 1967), 960–966.
- [Zhang et al. 2012] H. W. Zhang, Z. Q. Xie, B. S. Chen, and H. L. Xing, “A finite element model for 2D elastic-plastic contact analysis of multiple Cosserat materials”, *Eur. J. Mech. A Solids* **31** (2012), 139–151.
- [Zhu 1995] C. Zhu, “A finite element-mathematical programming method for elastoplastic contact problems with friction”, *Finite Elem. Anal. Des.* **20**:4 (1995), 273–282.

Received 6 Mar 2014. Revised 21 Jul 2014. Accepted 3 Aug 2014.

ERDAL ÖNER: [eoner@bayburt.edu.tr](mailto:eoner@bayburt.edu.tr)

Department of Civil Engineering, Bayburt University, 69000 Bayburt, Turkey

MURAT YAYLACI: [murat.yaylaci@erdogan.edu.tr](mailto:murat.yaylaci@erdogan.edu.tr)

Department of Civil Engineering, Recep Tayyip Erdoğan University, 53100 Rize, Turkey

AHMET BİRİNCİ: [birinci@ktu.edu.tr](mailto:birinci@ktu.edu.tr)

Department of Civil Engineering, Karadeniz Technical University, 61080 Trabzon, Turkey





## SLIDING OF A CUP-SHAPED DIE ON A HALF-SPACE: INFLUENCE OF THERMAL RELAXATION, CONVECTION AND DIE TEMPERATURE

LOUIS MILTON BROCK

A rigid, cup-shaped die translates at constant subcritical speed on a thermoelastic half-space that exhibits thermal relaxation and convection. The die surface is held at a temperature different from ambient temperature, and sliding friction exists in a contact zone that is not simply connected. A three-dimensional dynamic steady state model is assumed and, based on an approximation for inversion of integral transforms, a solution in analytic form is obtained. Auxiliary conditions for sliding contact are satisfied; in particular, contact zone traction is stationary with respect to compression force. Among other results, it is found that a dynamic steady state is precluded if die-ambient temperature difference is too large. Similar results are known, but only for die temperatures that exceed the ambient value.

### Introduction

Sliding of a rigid die on the surface of elastic half-spaces is a basic model in isothermal [Craggs and Roberts 1967; Churilov 1978; Ahmadi et al. 1983; Rahman 1996] and dynamic thermoelastic contact [Jang 2000; 2005]. In [Brock 2012a] the 3D problem of an ellipsoid moving at constant sub critical speed is considered. An exact solution for the dynamic steady state shows that the projection of the die profiles onto the half-space is not necessarily replicated in contact zone shape. In particular, friction and sliding speed play a role in contact zone shape. An asymptotic solution [Brock 2012b] is obtained for the corresponding 3D case of a half-space governed by the Fourier model of thermoelasticity [Boley and Weiner 1985]. Expressions in analytic form lead to conclusions about the contact zone that mirror those in [Brock 2012a].

A more recent 3D study [Brock 2014b] treats various die shapes. Friction is neglected, but the half-space exhibits both thermal relaxation and convection, and the dies are maintained at a fixed temperature. Again expressions in analytic form are obtained by using an asymptotic transform inversion. It is found that a dynamic steady state cannot in fact occur when die temperature exceeds ambient temperature by a critical value. This result is consistent with transient work [Jang 2000; 2005].

In the aforementioned references, however, the die shapes considered give simply connected contact zones. Such a situation is not always assured [Bayer 1994; Blau 1996]. Die surfaces may exhibit curvature reversals that preclude simple connectivity and, as an example, this paper considers a cup-shaped rigid die. The half-space exhibits thermal relaxation and convection, and the die surface is maintained at a fixed temperature that differs from the ambient. A dynamic steady state is assumed, and sliding friction exists. A contact zone traction distribution is not assumed and contact zone geometry parameters are obtained by imposing standard [Barber 1992; Brock and Georgiadis 2000] auxiliary conditions. Here,

*Keywords:* thermoelasticity, 3D, relaxation, multiple connectivity, critical temperature, convection, 3D dynamic, sliding, transverse isotropy, contact zone geometry.

these conditions lead to algebraic equations of fifth- and sixth-order, but valid approximate solutions are possible. Among other results, this analysis indicates that, in contrast to [Jang 2000; 2005; Brock 2014b] restrictions apply for die temperature values both above and below ambient temperature.

The 3D analysis begins by considering the unmixed boundary value problem for surface loads applied to an area that translates on the half-space surface. The area is ring-like, but axial symmetry is not assumed. An exact solution for the integral transform is obtained in terms of (somewhat arbitrary) loads. An approximate transform inversion technique that is especially valid when thermal relaxation effects are of interest is applied. The resulting expressions are analytic, and their use reduces the mixed boundary value problem for sliding contact to the solution of classical singular integral equations [Erdogan 1978]. Imposition of auxiliary conditions, and study of the results, follows.

### Translating surface load: governing equations

In terms of Cartesian basis  $\mathbf{x} = \mathbf{x}(x_k)$  a solid occupies region  $x_3 > 0$ . The solid is isotropic, homogeneous and linear thermoelastic. It is at rest at uniform (absolute) temperature  $T_0$ , when a finite, ring-like area  $C$  on surface  $x_3 = 0$  is subjected to traction and a temperature field  $T_C \neq T_0$ . Curves  $f(x_1, x_2) = 0$  and  $\mathfrak{S}(x_1, x_2) = 0$  define, respectively, the inner and outer boundaries of  $C$ . Neither curve is necessarily circular, but is closed, with a tangent and normal that vary continuously. Each radius of curvature also varies continuously, without inflection. Surface point  $(x_1, x_2) = 0$  lies within contour  $f$ , and any straight line through this point lies within contour  $\mathfrak{S}$ .

Area  $C$  then translates in the positive  $x_1$ -direction with constant subcritical speed  $V$ . The geometry of  $C$  does not change, and imposed temperature  $T_C$  and the traction distribution remain invariant with respect to  $C$ . It is assumed that a dynamic steady state ensues for which solid response is invariant in the frame of translating  $C$ . Thus, by translating the Cartesian basis with  $C$ , displacement  $\mathbf{u}(u_k)$ , traction  $\mathbf{T}(\sigma_{ik})$  and change  $\theta$  in temperature vary only with  $\mathbf{x}(x_k)$ , and time differentiation becomes  $-V\partial_1$ , where  $\partial_k$  signifies  $x_k$ -differentiation. For  $x_3 > 0$  governing equations for  $(\mathbf{u}, \theta)$  can be written as [Brock 2009; Ignaczak and Ostoja-Starzewski 2010]

$$\mathbf{u} = \mathbf{u}_D + \mathbf{u}_S, \quad (1a)$$

$$(\nabla^2 - c^2\partial_1^2)\mathbf{u}_S = 0, \quad \nabla \cdot \mathbf{u}_S = 0, \quad (1b)$$

$$(c_D^2\nabla^2 - c^2\partial_1^2)\mathbf{u}_D - \alpha_V\nabla\theta = 0, \quad \nabla \times \mathbf{u}_D = 0, \quad (1c)$$

$$[h_0(c_+^2\nabla^2 - c^2\partial_1^2)(c_-^2\nabla^2 - c^2\partial_1^2) - c\partial_1(c_F^2\nabla^2 - c^2\partial_1^2)](\mathbf{u}_D, \theta) = 0. \quad (1d)$$

Here  $(\nabla, \nabla^2)$  are the gradient and Laplacian. Traction  $\mathbf{T}$  is defined by

$$\frac{1}{\mu}\mathbf{T} = [(c_D^2 - 2)\nabla \cdot \mathbf{u}_D - \alpha_V\theta]\mathbf{1} + 2(\nabla\mathbf{u} + \mathbf{u}\nabla). \quad (2)$$

Term  $\mathbf{1}$  is the identity tensor, and  $(c, c_D, c_F, c_{\pm})$  are dimensionless ratios

$$c = \frac{V}{V_S}, \quad c_D = \frac{V_D}{V_S}, \quad c_F = \frac{V_F}{V_S}, \quad c_{\pm} = \frac{V_{\pm}}{V_S}. \quad (3)$$

Here  $(V, V_S, V_D, V_F, V_{\pm})$  are, respectively, translation speed, isothermal shear wave speed, isothermal and Fourier dilatational wave speed and thermal relaxation speeds, where

$$c_D = \sqrt{2 \frac{1-\nu}{1-2\nu}}, \quad c_F = \sqrt{c_D^2 + \epsilon}, \quad c_{\pm} = \frac{1}{2}(\Gamma_{+} \pm \Gamma_{-}), \quad (4a)$$

$$\Gamma_{\pm} = \sqrt{(c_D \pm \sqrt{h/h_0})^2 + \epsilon}, \quad (4b)$$

$$h = \frac{k}{C_V \sqrt{\mu\rho}}, \quad h_0 = V_S t_0, \quad \epsilon = \frac{T_0}{C_V} (\alpha_V V_S), \quad (4c)$$

$$\alpha_V = (3c_D^2 - 4)\alpha, \quad V_S = \sqrt{\mu/\rho}. \quad (4d)$$

In (2)–(4) ( $\nu$ ,  $\mu$ ,  $\rho$ ) are Poisson's ratio, shear modulus and mass density, respectively. Terms ( $k$ ,  $C_V$ ,  $\alpha$ ,  $\alpha_V$ ) are thermal conductivity, specific heat at constant strain, and linear and volumetric thermal expansion coefficients, respectively. Terms ( $\epsilon$ ,  $h$ ) are dimensionless thermal coupling constant and thermoelastic characteristic length. Terms ( $t_0$ ,  $h_0$ ) are thermal relaxation time and corresponding characteristic length [Brock 2009]. They are features of the Lord and Shulman [1967] model for thermal relaxation that is incorporated in (1)–(4). Calculations [Achenbach 1973; Brock and Georgiadis 2000; Brock 2009; Ignaczak and Ostoja-Starzewski 2010] indicate that, in general,  $1 < c_D < c_F < c_{\pm}$ .

On surface  $x_3 = 0$  heat flux and surface traction for  $(x_1, x_2) \notin C$  are

$$h_B \partial_3 \theta + \theta = 0, \quad \sigma_{31} = \sigma_{32} = \sigma_{33} = 0. \quad (5a)$$

For  $(x_1, x_2) \in C$ , however:

$$h_B \partial_3 \theta + \theta = T_C - T_0 = \theta_C, \quad (5b)$$

$$\sigma_{31} = \tau_1, \quad \sigma_{32} = \tau_2, \quad \sigma_{33} = \sigma. \quad (5c)$$

Field  $T_C$  is bounded and continuous, and  $h_B$  is a characteristic convection length that incorporates conductivity and Biot number [Boley and Weiner 1985]. Traction ( $\tau_1$ ,  $\tau_2$ ,  $\sigma$ ) can be singular but integrable on contours  $f(x_1, x_2) = 0$  and  $\mathfrak{S}(x_1, x_2) = 0$ . In addition  $(\mathbf{u}, \mathbf{T}, \theta)$  should remain finite for  $|\mathbf{x}| \rightarrow \infty$ ,  $x_3 > 0$ .

### General transform solution

A double bilateral transform [Sneddon 1972] can be defined as

$$\hat{F} = \iint F(x_1, x_2) \exp(-p_1 x_1 - p_2 x_2) dx_1 dx_2. \quad (6)$$

Integration is along the entire  $\text{Re}(x_1)$  and  $\text{Re}(x_2)$ -axes. Application of (6) to (1) gives

$$\hat{\mathbf{u}}_S = \mathbf{V} \exp(-Bx_3), \quad (7a)$$

$$\hat{\mathbf{u}}_D = \mathbf{U}_+ \exp(-A_+ x_3) + \mathbf{U}_- \exp(-A_- x_3), \quad (7b)$$

$$\hat{\theta} = D_+ U_+ \exp(-A_+ x_3) + D_- U_- \exp(-A_- x_3). \quad (7c)$$

Coefficients  $D_{\pm}$  and the components of vectors  $(\mathbf{V}, \mathbf{U}_{\pm})$  are governed by

$$D_{\pm} = c_D^2 (p_2^2 + A_{\pm}^2) + (c_D^2 - c^2) p_1^2, \quad (8a)$$

$$p_1 V_1 + p_2 V_2 - B V_3 = 0, \quad \mathbf{U}_{\pm} = (p_1, p_2, -A_{\pm}) \alpha_V \mathbf{U}_{\pm}. \quad (8b)$$

Terms  $(B, A_{\pm})$  are roots of the transforms of, respectively, (1b) and (1d):

$$B = \sqrt{-p_1^2 - p_2^2 + c^2 p_1^2}, \tag{9a}$$

$$A_{\pm} = \sqrt{-p_1^2 - p_2^2 - \frac{cp_1}{2hc_D^2}(D_F \pm D)}, \tag{9b}$$

$$D_F = c_F^2(1 - h_0cp_1) - hcp_1, \quad D = \sqrt{D_F^2 + 4hc_D^2(1 - h_0cp_1)cp_1}. \tag{9c}$$

Equation (7) is bounded for  $x_3 > 0$  if branch cuts are introduced so that  $\text{Re}(B, A_{\pm}) \geq 0$  in the cut complex  $(p_1, p_2)$ -planes. Application of (6) to (2) and substitution of (8) and (9) gives for  $x_3 = 0$  quantities relevant to the transform of (5). In particular,

$$\frac{1}{\mu} \hat{\sigma}_{31} = -2\alpha_V p_1(A_+U_+ + A_-U_-) + \frac{1}{B}[p_1p_2V_2 + (p_1^2 - B^2)V_1], \tag{10a}$$

$$\frac{1}{\mu} \hat{\sigma}_{32} = -2\alpha_V p_2(A_+U_+ + A_-U_-) + \frac{1}{B}[p_2p_1V_1 + (p_2^2 - B^2)V_2], \tag{10b}$$

$$\frac{1}{\mu} \hat{\sigma}_{33} = -\alpha_V(2B^2 + c^2p_1^2)(U_+ + U_-) - 2(p_1V_1 + p_2V_2). \tag{10c}$$

In view of (7c) and (9), the transform of (5) gives the four equations required to obtain  $(U_{\pm}, V_1, V_2)$ . The transforms  $(\hat{u}, \hat{T}, \hat{\theta})$  then follow as linear combinations of  $(\hat{\tau}_1, \hat{\tau}_2, \hat{\sigma}, \hat{\theta}_C)$ . Displacement  $u$  for  $x_3 = 0$  is required to address the mixed boundary value problem of the sliding die.

**Transform inversion: general formulas**

Inhomogeneous terms  $(\tau_1, \tau_2, \sigma, \theta_C)$  arise only for  $(x_1, x_2) \in C$ . Thus, when  $x_3 = 0$  the inversion operation corresponding to (6) gives  $u$ , and also  $(T, \theta)$ , as linear combinations of expressions

$$\iint_C \Sigma d\xi_1 d\xi_2 \frac{1}{2\pi i} \int dp_1 \frac{1}{2\pi i} \int K_{\Sigma} dp_2 \exp[p_1(x_1 - \xi_1) + p_2(x_2 - \xi_2)]. \tag{11}$$

Here  $\Sigma = \Sigma(\xi_1, \xi_2)$  represents  $(\tau_1, \tau_2, \sigma, \theta_C)$  and  $K_{\Sigma} = K_{\Sigma}(p_1, p_2)$  is the corresponding coefficient. Subscript  $C$  signifies integration over area  $C$ , and single integration is over the entire  $\text{Im}(p_1)$  and  $\text{Im}(p_2)$ -axes. The form of (11) suggests definitions and transformations [Brock 2012a; 2012b].

$$p_1 = p \cos \psi, \quad p_2 = p \sin \psi, \tag{12a}$$

$$\begin{bmatrix} x, \xi \\ y, \eta \end{bmatrix} = \begin{bmatrix} \cos \psi & \sin \psi \\ -\sin \psi & \cos \psi \end{bmatrix} \begin{bmatrix} x_1, \xi_1 \\ x_2, \xi_2 \end{bmatrix}. \tag{12b}$$

In (12),  $\text{Re}(p) = 0+$ ,  $|\text{Im}(p), x, y, \xi, \eta| < \infty$  and  $|\psi| < \pi/2$ . Parameters  $(p, \psi), (x, \psi; y = 0)$  and  $(\xi, \psi; \eta = 0)$  resemble quasipolar coordinate systems, i.e.,

$$d\xi_1 d\xi_2 = |\xi| d\xi d\psi, \quad dp_1 dp_2 = |p| dp d\psi. \tag{13}$$

In light of (12), (13) and conditions for contour functions  $(f, \mathfrak{S})$ , (11) can be written as

$$\frac{1}{i\pi} \int_{\Psi} d\psi \iint_C d\eta d\xi \Sigma(\xi, \eta) \int \frac{|p| dp}{2\pi i} K_{\Sigma}(p, \psi) \exp(p(x - \xi)). \tag{14a}$$

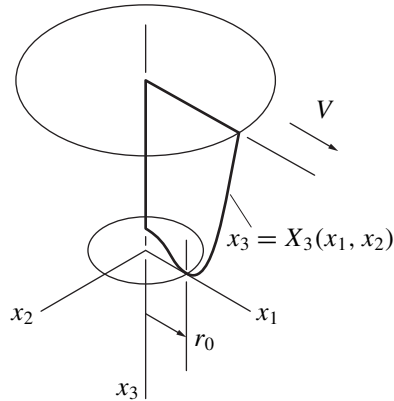


**Figure 1.** Schematic of area of revolution for sliding cup.

Here subscript  $\Psi$  signifies integration over range  $|\psi| < \pi/2$ ,  $p$ -integration is along the positive side of the entire imaginary axis, and

$$\iint_{\pm} d\eta d\xi = \left[ \int_{N^-}^{\eta^-} + \int_{\eta^+}^{N^+} \right] d\eta \int_{X_-}^{X_+} d\xi + \int_{\eta^-}^{\eta^+} d\eta \left[ \int_- + \int_+ \right] d\xi. \quad (14b)$$

Here affixed symbol  $\pm$  signifies integration over range  $x_+ < \xi < X_+$  and  $X_- < \xi < x_-$ , respectively. Limits  $N^{\pm}(\psi)$  and  $\eta^{\pm}(\psi)$  in (14b) are defined by

$$\mathfrak{S}(\xi_1(\xi, N^{\pm}), \xi_2(\xi, N^{\pm})) = 0, \quad \frac{dN^{\pm}}{d\xi} = 0, \quad (15a)$$

$$f(\xi_1(\xi, \eta^{\pm}), \xi_2(\xi, \eta^{\pm})) = 0, \quad \frac{d\eta^{\pm}}{d\xi} = 0. \quad (15b)$$

That is, for given  $\psi$  limits  $(N^{\pm}, \eta^{\pm})$  are the maximum and minimum values of  $\eta$  on, respectively, the outer and inner contours of  $C$ . For given  $\eta$ , therefore, limits  $X_{\pm}(\psi, \eta)$  and  $x_{\pm}(\psi, \eta)$  locate the ends of lines that run parallel to the  $\xi$ -axis and span the interiors of, respectively, the outer and inner contours of  $C$ . Conditions on  $C$  imply that these limits exist, are single-valued, and vary continuously in  $\psi$ .

### Transform inversion: asymptotic results

Equations (9b), (9c) and (12a) suggest that, in general, a numerical procedure is required for  $p$ -integration in (14a). This is a common situation in coupled thermoelasticity and often, for example, [Wang and Dhaliwal 1993; Brock 2009], an asymptotic inversion is used to produce an analytic result. Calculations [Brock and Georgiadis 2000; Ignaczak and Ostoja-Starzewski 2010] indicate that, typically,

$$h \approx O(10^{-9}) \text{ m}, \quad t_0 \approx O(10^{-13}) \text{ s}, \quad V_S \approx O(10^3) \text{ m/s}, \quad 0.1 < h_0/h < 1.0.$$

Therefore, use of expansions for (8) and (9) in (14a) that are valid for  $|hp| \gg 1$  give results that are especially relevant [Brock 2009] to the study of thermal relaxation effects. In light of (12), (9) gives,

respectively, the exact result and first-order expansion

$$B \rightarrow B\sqrt{p}\sqrt{-p}, \quad B = \sqrt{1 - c^2 \cos^2 \psi}, \tag{16a}$$

$$A_{\pm} \rightarrow A_{\pm}\sqrt{p}\sqrt{-p} + O(1/hp), \quad A_{\pm} = \sqrt{1 - \frac{c^2}{c_{\pm}^2} \cos^2 \psi}. \tag{16b}$$

Boundedness for  $x_3 > 0$  now requires that  $(c, \psi)$  give nonnegative arguments for radical  $(B, A_{\pm})$ , branch cuts  $\text{Re}(p) < 0, \text{Im}(p) = 0$  and  $\text{Re}(p) > 0, \text{Im}(p) = 0$  be introduced for  $\sqrt{\pm p}$ , respectively, and  $\text{Re}(\sqrt{\pm p}) \geq 0$  in the corresponding cut  $p$ -plane. In view of (12) and (16), the linear combination of products  $K_{\Sigma}(p, \psi)\Sigma(\xi, \eta)$  in (14a) for displacement  $u_k$  when  $x_3 = 0$  is

$$u_1: \frac{B}{pR_A} \cos \psi \left[ \frac{2\alpha_V}{h_B p \omega} (A_- - A_+) \theta_C - N \frac{\sigma}{\mu} \right] + \frac{1}{p \omega R_A} \left( N_1 \frac{\tau_1}{\mu} + N_{12} \frac{\tau_2}{\mu} \right), \tag{17a}$$

$$u_2: \frac{B}{pR_A} \sin \psi \left[ \frac{2\alpha_V}{h_B p \omega} (A_- - A_+) \theta_C - N \frac{\sigma}{\mu} \right] + \frac{1}{p \omega R_A} \left( N_2 \frac{\tau_2}{\mu} + N_{12} \frac{\tau_1}{\mu} \right), \tag{17b}$$

$$u_3: \frac{K\alpha_V}{h_B p^2 R_A} (A_- - A_+) \theta_C + \frac{N_3}{p \omega R_A} \frac{\sigma}{\mu} + \frac{N}{p R_A} \left( \cos \psi \frac{\tau_1}{\mu} + \sin \psi \frac{\tau_2}{\mu} \right). \tag{17c}$$

In (17)  $\tau_k = \tau_k(\xi, \eta)$ ,  $\sigma = \sigma(\xi, \eta)$ ,  $\theta_C = \theta_C(\xi, \eta)$  and

$$\omega = \frac{\sqrt{-p}}{\sqrt{p}}. \tag{18}$$

Other terms in (17) are independent of  $p$ :

$$R_A = K_+ A_+ R_- - K_- A_- R_+, \tag{19a}$$

$$N = K_+ A_+ N_- - K_- A_- N_+, \tag{19b}$$

$$N_1 = -R_A + M \cos^2 \psi, \quad N_2 = -R_A + M \sin^2 \psi, \quad N_{12} = M \sin \psi \cos \psi, \tag{19c}$$

$$M = K_+ A_+ M_- - K_- A_- M_+, \quad N_3 = (K_+ - K_-) A_+ A_- c^2 \cos^2 \psi. \tag{19d}$$

Terms in (19) with  $\pm$  subscript are given by

$$R_{\pm} = 4A_{\pm}B - K^2, \quad N_{\pm} = 2A_{\pm}B + K, \quad M_{\pm} = 4A_{\pm}B + K - B^2, \tag{20a}$$

$$K = c^2 \cos^2 \psi - 2, \quad K_{\pm} = 1 - \frac{c_D^2}{c_{\pm}^2}. \tag{20b}$$

Equation (17) shows that  $K_{\Sigma}$ -terms in (14a) have the forms  $(1/p, 1/p^2, 1/p\omega)$ . The respective  $p$ -integration in (14a) gives [Brock 2012a; 2012b]

$$-i\delta(x - \xi), \quad -iH(x - \xi), \quad \frac{1}{i\pi(x - \xi)}. \tag{21}$$

Here  $(\delta, H)$  is the Dirac and step function. Displacement  $u_3$  for  $x_3 = 0$  is of particular interest, and an expression is given in an explicit form in Appendix A.

Component  $R_{\pm}$  of  $R_A$  in (20a) resembles in form the isothermal Rayleigh function [Achenbach 1973]. Indeed, for  $\psi = 0$   $R_A$  exhibits roots  $c = 0$  and  $c = \pm c_A$ , where  $0 < c_A < 1$ , and is positive for  $0 < |c| < c_A$ ,

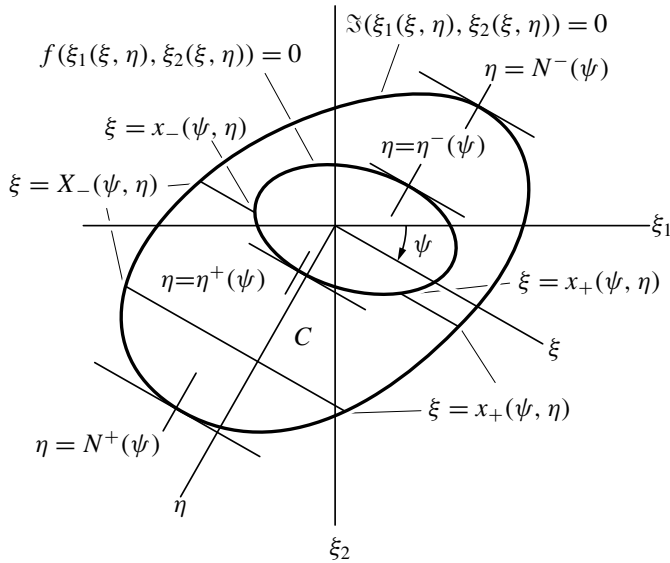


**Figure 2.** Schematic of translating area on surface.

and thus is also a Rayleigh function. Radicals ( $A_{\pm}, B$ ) have nonnegative arguments for  $0 < c \cos \psi < 1$ ,  $|\psi| \leq \pi/2$  and, as noted in connection to (4),  $1 < c_D < c_- < c_+$ . Therefore  $V = c_A V_S < V_S < c_{\pm} V_S$  is the critical speed for translation of area  $C$ . The results of this section are now applied to a study of sliding contact with friction.

### Sliding contact

Consider the half-space treated above, and a rigid die that is a body of revolution with a W-like profile, i.e., it is cup-shaped. Surface temperature of the die is maintained at  $T_C = T_0 + \Theta_C \cos \psi$ , where  $\Theta_C$  is constant. Constant compressive force  $F_3$  is applied to the die and, resisted by sliding friction, the die translates at constant subcritical speed  $V$  in the positive  $x_1$ -direction. A dynamic steady state is assumed, and the process also satisfies (5a) and (5b). However (5c) is modified: For  $x_3 = 0$ ,  $(x_1, x_2) \in C$ ,  $(\tau_1, \tau_2)$  now represent frictional resistance and so are defined by

$$\tau_1 = \gamma \sigma, \quad \tau_2 = 0. \tag{22}$$

Here  $\gamma$  is the coefficient of sliding friction, and normal traction  $\sigma$  is now an unknown, the last condition in (5c) being replaced by

$$u_3 = u_3^0 = U_0 - X_3(x_1, x_2), \tag{23a}$$

$$X_3(x_1, x_2) = \frac{1}{2r_0}(x_1^2 + x_2^2) \left[ 1 - \frac{1}{2r_0^2}(x_1^2 + x_2^2) \right] - \frac{r_0}{4}. \tag{23b}$$

Here  $u_3^0$  is the indentation imposed by the die, with  $U_0$  being the rigid body displacement of the die. Polynomial  $X_3(x_1, x_2)$  gives the die its W-like cross-section, where  $r_0$  is the radial distance between the die axis of symmetry and the “feet” of the W. Results obtained above apply under several conditions: First, area  $C$  includes the initial ( $U_0 = 0$ ) contact contour  $\sqrt{x_1^2 + x_2^2} = r_0$ . Then  $C$  has a ring thickness

that, in light of the fourth-order nature of  $X_3(x_1, x_2)$ , is much smaller than  $r_0$ . Finally,  $\sigma$  must be such that (A1) and (22) give the displacement in (23a). In view of [Brock 2012a; 2012b]

$$u_3^0 = -\frac{1}{\pi} \int_{\Psi} d\psi \iint_C d\eta d\xi \frac{d\delta}{dx} (x - \xi) u_3^0(x_1(\xi, \eta), x_2(\xi, \eta)). \tag{24}$$

So,  $\sigma$  is obtained by matching the integrands of  $(\psi, \eta)$ -integration. In  $\sigma(\xi, \eta)$   $\xi$  is an integration variable representing parameter  $x$  that itself depends on  $(x_1, x_2)$  and integration variable  $\psi$ . As noted in view of (13) for  $y = 0$  however, coordinates  $(x_1, x_2)$  can be replaced by  $(x, \psi)$ . Thus, every point  $(x_1, x_2) \in C$  lies on an integration path  $\eta = 0$  that passes through all four limit points of the  $\xi$ -integral. Thus (A1) and (22)–(25) give for  $x_+ < x < X_+$  and  $X_- < x < x_-$ , respectively, singular integral equation

$$-\frac{N_3}{\mu R_A \pi} \left[ \int_{-}^{+} + (vp) \int_{+} \right] \frac{\sigma(\xi, \psi)}{\xi - x} d\xi + \frac{\gamma N}{R_A} \sigma(x, \psi) \cos \psi = \frac{x}{r_0} \left( 1 - \frac{x^2}{r_0^2} \right) - \frac{T}{r_0} (X_+ - x), \tag{25a}$$

$$-\frac{N_3}{\mu R_A \pi} \left[ (vp) \int_{-} + \int_{+} \right] \frac{\sigma(\sigma, \psi)}{\xi - x} d\xi + \frac{\gamma N}{R_A} \sigma(x, \psi) \cos \psi = \frac{x}{r_0} \left( 1 - \frac{x^2}{r_0^2} \right) - \frac{T}{r_0} (x_- - x), \tag{25b}$$

$$T = -\frac{r_0 K \alpha_V}{h_B R_A} (A_+ - A_-) \Theta_C \cos \psi. \tag{25c}$$

In (25) affixed symbol  $\pm$  signifies integration over, respectively,  $x_+ < \xi < X_+$  and  $X_- < \xi < x_-$ , where  $x_{\pm} = x_{\pm}(\psi)$  and  $X_{\pm} = X_{\pm}(\psi)$ , and  $(vp)$  signifies Cauchy principal value integration. Equation (25) is a classic type [Erdogan 1978], with inhomogeneous terms of polynomial form. The solution is a linear combination of terms

$$x^N \cos \pi \Omega + \frac{\sin \pi \Omega}{\pi} \left( \frac{x - x_-}{x - X_-} \right)^{\Omega} \left( \frac{X_+ - x}{x - x_+} \right)^{\Omega} I_+(x^N) \quad (x_+ < x < X_+), \tag{26a}$$

$$x^N \cos \pi \Omega + \frac{\sin \pi \Omega}{\pi} \left( \frac{X_+ - x}{x_+ - x} \right)^{\Omega} \left( \frac{x_- - x}{x - X_-} \right)^{\Omega} I_-(x^N) \quad (X_- < x < x_-). \tag{26b}$$

In (26)  $N = 0, 1, 3$  and

$$I_+(x^N) = \int_{-} \frac{t^N dt}{t - x} \left( \frac{x_+ - t}{X_+ - t} \right)^{\Omega} \left( \frac{t - X_-}{x_- - t} \right)^{\Omega} + (vp) \int_{+} \frac{t^N dt}{t - x} \left( \frac{t - X_-}{t - x_-} \right)^{\Omega} \left( \frac{t - x_+}{X_+ - t} \right)^{\Omega}, \tag{27a}$$

$$I_-(x^N) = (vp) \int_{-} \frac{t^N dt}{t - x} \left( \frac{x_+ - t}{X_+ - t} \right)^{\Omega} \left( \frac{t - X_-}{x_- - t} \right)^{\Omega} + \int_{+} \frac{t^N dt}{t - x} \left( \frac{t - X_-}{t - x_-} \right)^{\Omega} \left( \frac{t - x_+}{X_+ - t} \right)^{\Omega}, \tag{27b}$$

$$\Omega = -\frac{1}{2} + \frac{1}{\pi} \tan^{-1} \left( -\frac{\gamma N}{N_3} \cos \psi \right). \tag{27c}$$

For sliding contact at subcritical speed (see discussion above) it can be shown that  $N \leq 0$  and  $N_3 \geq 0$ , so that dimensionless exponent satisfies  $-\frac{1}{2} < \Omega < 0$ . Integration formulas (B1)–(B3) in Appendix B lead to, for  $x_+ < x < X_+$  and  $X_- < x < x_-$ , respectively, contact zone normal traction in analytic



form:

$$\frac{\sigma_+}{\mu} = -\frac{R_A}{r_0 S} \left( \frac{x - x_-}{x - X_-} \right)^\Omega \left( \frac{X_+ - x}{x - x_+} \right)^\Omega \left[ (1 + T)G_1(x) - TX_+ - \frac{G_3(x)}{r_0^2} \right], \tag{28a}$$

$$\frac{\sigma_-}{\mu} = -\frac{R_A}{r_0 S} \left( \frac{X_+ - x}{x_+ - x} \right)^\Omega \left( \frac{x_- - x}{x - X_-} \right)^\Omega \left[ (1 + T)G_1(x) - Tx_- - \frac{G_3(x)}{r_0^2} \right], \tag{28b}$$

$$S = \sqrt{(\gamma N \cos \psi)^2 + N_3^2}. \tag{28c}$$

Equation (28) involves contact zone parameters  $(X_\pm, x_\pm)$ . These can be determined by satisfying auxiliary conditions that must be imposed on the solution.

**Auxiliary conditions**

Because the die is not flat-bottomed, contact zone traction should be continuous at the zone boundaries:

$$\sigma_\pm(X_\pm, \psi) = \sigma_\pm(x_\pm, \psi) = 0. \tag{29a}$$

Continuity of the contact zone contour functions  $(\mathfrak{S}, f)$  requires that

$$X_+(\pi/2) + X_-(\pi/2) = 0, \quad x_+(\pi/2) + x_-(\pi/2) = 0. \tag{29b}$$

In light of (C1), (C2), (C3a) and (C4) in Appendix C, imposing (29) on (28) gives

$$\frac{\sigma_+}{\mu} = \frac{R_A}{S} \left( \frac{z - z_-}{z - Z_-} \right)^\Omega \left( \frac{Z_+ - z}{z - z_+} \right)^\Omega (Z_+ - z)[T - (Z_+ + z_- + \Omega l)(z - z_-)], \tag{30a}$$

$$\frac{\sigma_-}{\mu} = \frac{R_A}{S} \left( \frac{Z_+ - z}{z_+ - z} \right)^\Omega \left( \frac{z - z_-}{z - Z_-} \right)^\Omega (z - z_-)[T - (Z_+ + z_- + \Omega l)(Z_+ - z)]. \tag{30b}$$

In (30) Equations (B3), (C2) and (C5) are used to introduce dimensionless parameters

$$z = \frac{x}{r_0}, \quad Z_\pm = \frac{X_\pm}{r_0}, \quad z_\pm = \frac{x_\pm}{r_0}, \tag{31a}$$

$$l_\pm = L_\pm/r_0 = \frac{1}{2}(l + \bar{l}), \quad l_- = L_-/r_0 = \frac{1}{2}(l - \bar{l}), \tag{31b}$$

$$\bar{l} = 0 \quad (|\psi| = \pi/2). \tag{31c}$$

Here  $L_\pm$  is the thickness of the two contact zone ring segments measured along a line that passes through  $\mathbf{x} = 0$  at angle  $|\psi| \leq \pi/2$ . Under the reasonable assumption that the contact zone ring is “thin” ( $l_\pm \ll 1$ ), imposition of (29a) is shown in Appendix C to give the valid approximations

$$Z_+ = 1 + \frac{1}{2}\Omega(Tl - l - \bar{l}), \quad z_+ = 1 + \frac{1}{2}[\Omega Tl - (1 + \Omega)(l + \bar{l})], \tag{32a}$$

$$z_- = -1 + \frac{1}{2}\Omega(Tl - l + \bar{l}), \quad Z_- = -1 + \frac{1}{2}[\Omega Tl - (1 + \Omega)(l - \bar{l})], \tag{32b}$$

$$Z_+ + z_- + \Omega l = \Omega Tl. \tag{32c}$$

The resultant of contact zone traction must be the compressive force  $F_3$  on the die:

$$\iint_C \sigma(x_1, x_2) dx_1 dx_2 = r_0^2 \int_{\psi} d\psi \left[ \int_{-} |z| \sigma_{-}(z, \psi) dz + \int_{+} |z| \sigma_{+}(z, \psi) dz \right] = -F_3. \tag{33}$$

Affixed symbol  $\pm$  now signifies integration over range  $z_+ < z < Z_+$  and  $Z_- < z < z_-$ . Traction  $\sigma_{\pm}(z, \psi)$  should be stationary with respect to  $F_3$  [Brock 2012a; 2012b; 2014b]:

$$\delta\sigma_{\pm} = \frac{\partial\sigma_{\pm}}{\partial z} \delta z + \frac{\partial\sigma_{\pm}}{\partial\psi} \delta\psi = 0. \tag{34}$$

Because  $(\delta z, \delta\psi)$  are arbitrary, (34) requires for  $|\psi| < \pi/2$  that

$$\frac{\partial\sigma_{\pm}}{\partial z}(z, \psi) = 0(z = z_{\pm}^*), \quad \frac{\partial\sigma_{\pm}}{\partial\psi}(z_{\pm}^*, \psi) = 0. \tag{35}$$

The process for obtaining  $z_{\pm}^*$  is outlined in Appendix D. In keeping with (32), valid approximations are sufficient:

$$z_+^* = 1 + \frac{\Omega}{2}(Tl - l - \bar{l}) - \frac{2(1 + \Omega) - T}{2 + (1 - \Omega)T} \frac{l + \bar{l}}{2}, \tag{36a}$$

$$z_-^* = -1 + \frac{\Omega}{2}(Tl - l + \bar{l}) - \frac{2(1 + \Omega) - T}{2 + (1 - \Omega)T} \frac{l - \bar{l}}{2}. \tag{36b}$$

Use of (32) and (36) in (30) give

$$\frac{\sigma_{\pm}^*}{\mu} = \frac{R_A}{2S} \frac{\Omega - 2}{2 + (1 - \Omega)T} \frac{[2(1 + \Omega) - T]^{1 + \Omega}}{[-2\Omega + (2 - \Omega)T]^{\Omega}} (l \pm \bar{l}). \tag{37}$$

For sliding without surface bonding, the contact zone cannot be in tension. Moreover, the radicals in (37) must have positive arguments. Thus unilateral constraints are required. Because  $(R_A, S)$  defined in (19a) and (28c) are positive for subcritical sliding, these are

$$-\frac{2}{1 - \Omega} < \frac{2\Omega}{2 - \Omega} < T < 2(1 + \Omega) < 2. \tag{38}$$

In view of (25c), therefore, sliding contact by the die has a dynamic steady state only if the difference in ambient ( $T_0$ ) and die ( $T_C$ ) temperature satisfies (38). Similar phenomena are noted for a flat contact surface [Jang 2000; 2005] and sliding dies of various profiles in the absence of friction [Brock 2014b]. However, contact zones are simply connected, and restrictions apply only if die temperature exceeds the ambient value.

The second condition in (35) requires that  $\sigma_{\pm}^*$  be invariant with respect to  $\psi$ . In view of (19), (20), (25c), (27c), (28c) and (31c), when  $|\psi| = \pi/2$ , we have

$$\Omega = -\frac{1}{2}, \quad T = 0, \quad \bar{l} = 0, \quad \frac{R_A}{S} = \frac{2(c_D^2 - 1)}{\sqrt{c_D^4 + \gamma^2}}. \tag{39}$$

Thus (37) gives two equations for  $(l, \bar{l})$  at any  $|\psi| < \pi/2$  in terms of the unknown  $l$  at  $|\psi| = \pi/2$ . We identify it as  $l_2$ , i.e., a measurement taken along the  $x_2$ -axis, and find that

$$l = \frac{2(c_D^2 - 1)S}{R_A \sqrt{c_D^2 + \gamma^2}} Q l_2, \quad \bar{l} = 0, \quad (40a)$$

$$Q = \frac{2 + (1 - \Omega)T}{2 - T} \frac{[-2\Omega + (2 - \Omega)T]^\Omega}{[2(1 + \Omega) - T]^{1+\Omega}}. \quad (40b)$$

A valid approximation to the  $z$ -integration in (33) involving (30) can, under (again) the expectation that  $(l, \bar{l}) \ll 1$ , be obtained. In view of (40a) this leads to an equation for the unknown  $l_2$ . Introduction of the integration variable  $t = c \cos \psi$  renders this as

$$\frac{F_3}{\mu r_0^2} = \frac{\pi(c_D^2 - 1)^2}{c_D^4 + \gamma^2} l_2^2 \int_0^c \frac{R_A dt}{S \sqrt{c^2 - t^2}} \frac{\Omega(1 + \Omega)}{\sin \pi \Omega} Q^2. \quad (41)$$

With  $l_2$  in hand, the solution process is complete.

### Sample calculations

For insight into restriction (38), die-ambient temperature difference is examined along the translating  $x_1$ -axis, that is,  $\psi = 0$ ,  $T_C - T_0 = \Theta_C$ . Values of parameter  $\Omega$  and the relevant maximum and minimum  $\Theta_C^\pm$  defined by (25c) and (38), for subcritical (dimensionless) translation speed  $c$  and friction coefficient  $\gamma$ , appear in Table 1. The half-space is modeled as a generic thermoelastic solid with properties

$$\begin{aligned} V_S &= 3094 \text{ m/s}, & \mu &= 75 \text{ GPa}, & \alpha_V &= 89.6(10^{-6})\text{K}^{-1}, \\ h &= 2.1862(10^{-10}) \text{ m}, & h_0 &= 2.3206(10^{-9}) \text{ m}, & \epsilon &= 0.05794, \\ c_D &= 2.0, & c_F &= 2.0144, & c_+ &= 3.0856, & c_- &= 2.3151, & c_A &= 0.933. \end{aligned}$$

The effect of die geometry and surface convection is represented by ratio

$$\frac{h_B}{r_0} = 4(10^{-4}).$$

Generic properties used in [Brock 2009; 2012b; 2014b] represent solids with more pronounced thermal relaxation. Thus, the dimensionless speeds  $c_\pm$  are somewhat larger than the values given above. Table 1 shows that die temperatures that lie below the ambient value are the more restricted. For given friction level ( $\gamma$ ), the range of allowable  $\Theta_C$  decreases as die translation speed ( $c$ ) increases. For given translation speed, the range decreases as friction level increases. Equations (25c) and (38) show, however, that the range will increase when convection ratio  $h_B/r_0$  is increased. The ranges indicated by Table 1 entries seems narrow, but the governing equations (1)–(4) themselves are based on the assumption that temperature change in the solid renders a small ratio  $|\theta/T_0|$ .

For insight into contact zone geometry, calculations for ratio  $l/l_2$  are given in Table 2 for the same generic solid. Parameters  $(l, l_2)$  are the widths of the ring formed by the contact zone as measured along lines  $|\psi| \neq 90^\circ$  and  $|\psi| = 90^\circ$ . In view of (40a), the ring of initial contact  $\sqrt{x_1^2 + x_2^2} = r_0$  (approximately) bisects these widths. Formulas such as (38) are based on the assumption that  $(l, l_2)/r_0 \ll 1$ . Thus, Table 2 entries show that the contact zone ring generated by compression and die translation is only approximately

	$c = 0.1$	$c = 0.2$	$c = 0.3$	$c = 0.4$	$c = 0.5$
	$\gamma = 0.1$				
$\Omega$	-0.4920	-0.4918	-0.4915	-0.4911	-0.4905
$\Theta_C^+(\text{°C})$	27.255	26.244	25.715	24.751	23.391
$\Theta_C^-(\text{°C})$	-10.594	-10.193	-9.978	-9.588	-9.041
	$\gamma = 0.2$				
$\Omega$	-0.4841	-0.4837	-0.4831	-0.4822	-0.481
$\Theta_C^+(\text{°C})$	27.682	26.665	26.142	25.184	23.828
$\Theta_C^-(\text{°C})$	-10.456	-10.057	-9.839	-9.449	-8.899
	$\gamma = 0.5$				
$\Omega$	-0.4604	-0.4594	-0.4579	-0.4558	-0.4527
$\Theta_C^+(\text{°C})$	28.954	27.921	27.415	26.468	25.126
$\Theta_C^-(\text{°C})$	-10.04	-9.646	-9.422	-9.027	-8.473

**Table 1.** Parameter  $\Omega$ , maximum (+) and minimum (-)  $\Theta_C$  for  $\chi(c)(\psi = 0)$ .

$l/l_2$	$c = 0.1$	$c = 0.2$	$c = 0.3$	$c = 0.4$	$c = 0.5$
	$\gamma = 0.1$				
$\psi = 0^\circ$	1.4247	1.4882	1.5654	1.6984	1.9199
$\psi = 45^\circ$	1.4366	1.4578	1.4936	1.5490	1.6289
$\psi = 90^\circ$	1.0	1.0	1.0	1.0	1.0
	$\gamma = 0.2$				
$\psi = 0^\circ$	1.4243	1.4885	1.565	1.698	1.9194
$\psi = 45^\circ$	1.4356	1.4567	1.4928	1.5481	1.6278
$\psi = 90^\circ$	1.0	1.0	1.0	1.0	1.0
	$\gamma = 0.5$				
$\psi = 0^\circ$	1.4213	1.4850	1.5625	1.6957	1.9179
$\psi = 45^\circ$	1.4295	1.4506	1.4865	1.5417	1.6275
$\psi = 90^\circ$	1.0	1.0	1.0	1.0	1.0

**Table 2.** Ratio  $l/l_2$  for  $\chi, \psi, c$  when  $\Theta_C = 10^\circ\text{C}$  ( $\Theta_C^- < \Theta_C < \Theta_C^+$ ).

circular. Parameter  $l_2$  is the minimum width, but  $l$  along the travel direction ( $\psi = 0$ ) is not the maximum width. This behavior is consistent with that for the simply connected contact zones considered in [Rahman 1996] and [Brock 2012a; 2012b; 2014b]. That is, the contact zone does not replicate the projection of the die profile onto the surface, and friction and direction and speed of translation are factors. Table 2 data indicate that here the friction effect is not as noticeable as that for translation speed and direction.

### Summary comments

This 3D, thermoelastic study indicates that a simply connected and a ring-like contact zone created by a sliding die share some characteristics: Die sliding speed and temperature, thermal relaxation and convection, and friction influence zone shape. The projection of die profile onto the surface may not adequately describe zone shape. In two respects, they may differ: For the simply connected zone, a dynamic steady state will not occur if die temperature exceeds ambient temperature by a critical value. For the ring-like zone, a critical value also exists for a die temperature that lies below ambient temperature. The influence of friction is less pronounced for the ring-like zone.

A cup-shaped die implies the ring-like contact zone, and an asymptotic transform inversion process renders solutions in analytic form. The assumption that contact zone size is “small” is manifest here in terms of ring width, and is used to justify robust, but approximate, expressions for contact zone geometry parameters. In [Brock 2012b] the asymptotic inversion process highlights solution behavior associated with the Fourier model [Boley and Weiner 1985]. Here and in [Brock 2014b], the process highlights behavior associated with the Lord and Shulman [1967] thermal relaxation model. In general, (see [Boley and Weiner 1985; Wang and Dhaliwal 1993], for example), and corresponds to the inversion process for the long-time transient solution. The latter is less so, and inversion corresponds to that for the short-time transient solution.

This work is part of a dynamic steady state study of 3D contact problems on isothermal and thermoelastic half-spaces. Anisotropy is also included, for example, [Brock 2014a]. The dynamic steady state is simpler to analyze than the transient, and is often sufficient to model sliding contact processes [Bayer 1994; Blau 1996].

The study makes use of exact expressions for multiple integral transforms associated with a related unmixed boundary value problem. The basis is Cartesian, but the inversion process — whether exact or asymptotic — introduces quasipolar coordinates. This hybridization produces expressions that lead readily to the formulation of the mixed 3D contact problem in terms of classical singular integral equations [Erdogan 1978]. Axial symmetry is not required.

The study — including this work — does involve contact zones for which the singular integral equations hold over the span of the zone, in whatever direction that span is taken. Inflections in contact zone contour, or multiple “holes” in the zone, create equation forms that are span-dependent. However, this complication need not preclude use of the basic approach.

### Appendix A

An expression for displacement  $u_3$  when  $x_3 = 0$  can be obtained from (12b), (14a), (17c) and (21) in an explicit form:

$$\begin{aligned}
 u_3 = & -\frac{1}{\pi} \int_{\Psi} \frac{N_3}{\mu\pi R_A} d\psi \times \left[ \int_{N^-}^{\eta^-} + \int_{\eta^+}^{N^+} \right] d\eta \int_{X_-}^{X_+} \frac{\sigma(\xi, \eta)}{\xi - x} d\xi + \int_{\eta^-}^{\eta^+} d\eta \left[ \int_{-} + \int_{+} \right] \frac{\sigma(\xi, \eta)}{\xi - x} d\xi \\
 & + \frac{\alpha_V}{h_B} \int_{\Psi} \frac{K}{\pi R_A} (A_- - A_+) d\psi \times \left[ \int_{\eta^-} + \int_{\eta^+} \right] d\eta \int_{X_-}^x \theta_C(\xi, \eta) d\xi H(X_+ - x) \\
 & + \int_{\eta^-}^{\eta^+} d\eta \left[ \int_{-} H(x_- - x) + \int_{+} H(X_+ - x) \right] \theta_C(\xi, \eta) d\xi + (continued)
 \end{aligned}$$

$$\begin{aligned}
 & + \int_{\Psi} \frac{N \cos \psi}{\mu \pi R_A} d\psi \times \left[ \int_{N^-}^{\eta^-} + \int_{\eta^+}^{N^+} \right] d\eta \int_{-} \tau_1(\xi, \eta) \delta(\xi - x) d\xi \\
 & + \int_{\eta^-}^{\eta^+} d\eta \left[ \int_{-} + \int_{+} \right] \tau_1(\xi, \eta) \delta(\xi - x) d\xi \\
 & + \int_{\Psi} \frac{N \sin \psi}{\mu \pi R_A} d\psi \times \left[ \int_{N^-}^{\eta^-} + \int_{\eta^+}^{N^+} \right] d\eta \int_{-} \tau_2(\xi, \eta) \delta(\xi - x) d\xi \\
 & + \int_{\eta^-}^{\eta^+} d\eta \left[ \int_{-} + \int_{+} \right] \tau_2(\xi, \eta) \delta(\xi - x) d\xi.
 \end{aligned} \tag{A1}$$

Here affixed symbol  $\pm$  indicates that integration is over the range  $x_+ < \xi < X_+$  and  $X_- < \xi < x_-$ . For  $(x_1, x_2) \in C$  Cauchy principal value integration (*vp*) is necessary when  $x$  lies the range of  $\xi$ -integration for  $\sigma$ . In corresponding fashion  $\xi$ -integration of  $(\tau_1, \tau_2)$  is replaced with  $\tau_1(x, \eta)$  and  $\tau_2(x, \eta)$ , respectively.

### Appendix B

Application of Cauchy theory to integrals (26a) and (26b) leads to the result

$$\begin{aligned}
 G_N(x) &= x^N \left( \frac{x - X_-}{x - x_-} \right)^\Omega \left( \frac{x - x_+}{X_+ - x} \right)^\Omega \cos \pi \Omega + \frac{\sin \pi \Omega}{\pi} I_+(x^N) \\
 G_N(x) &= x^N \left( \frac{x_+ - x}{X_+ - x} \right)^\Omega \left( \frac{x - X_-}{x_- - x} \right)^\Omega \cos \pi \Omega + \frac{\sin \pi \Omega}{\pi} I_-(x^N).
 \end{aligned} \tag{B1}$$

In (B1) we have

$$G_0(x) = 1, \tag{B2a}$$

$$G_1(x) = xG_0(x) + \Omega L, \tag{B2b}$$

$$G_2(x) = xG_1(x) + \frac{1}{2}\Omega(\Omega L^2 - L_+^2 - L_-^2) + \Omega(X_+L_+ + x_-L_-), \tag{B2c}$$

$$G_3(x) = xG_2(x) + \Omega[X_+L_+(X_+ + \Omega L - L_+) + x_-L_-(x_- + \Omega L - L_-)] + \frac{1}{6}\Omega(1 - \Omega)(2 - \Omega)L^3. \tag{B2d}$$

In (B2) the lengths are

$$L = L_+ + L_-, \quad L_+ = X_+ - x_+, \quad L_- = x_- - X_-. \tag{B3}$$

Terms  $L_{\pm}$  give the thickness of the two sides of the contact zone ring measured along the line passing through  $x = 0$  at a given angle  $-\pi/2 < \psi < \pi/2$ .

### Appendix C

Because  $\Omega < 0$ , (28) shows that (29a) is satisfied only if

$$X_+ + (1 + T)L - \frac{G_3(X_+)}{r_0^2} = 0, \quad x_- + (1 + T)L - \frac{G_3(x_-)}{r_0^2} = 0. \tag{C1}$$

At this point it is convenient to introduce dimensionless parameters

$$z = \frac{x}{r_0}, \quad Z_{\pm} = \frac{X_{\pm}}{r_0}, \quad z_{\pm} = \frac{x_{\pm}}{r_0}, \quad l = \frac{L}{r_0}, \quad l_{\pm} = \frac{L_{\pm}}{r_0}. \quad (\text{C2})$$

In light of (B2) and (B3), (C1) can be written as

$$Z_+ + (1 + T)l - \bar{G}_3(Z_+) = 0, \quad z_- + (1 + T)l - \bar{G}_3(z_-) = 0, \quad (\text{C3a})$$

$$\bar{G}_1(z) = z + \Omega l, \quad (\text{C3b})$$

$$\bar{G}_2(z) = z\bar{G}_1(z) + \frac{1}{2}\Omega(\Omega l^2 - l_+^2 - l_-^2) + \Omega(Z_+l_+ + z_-l_-), \quad (\text{C3c})$$

$$\bar{G}_3(z) = z\bar{G}_2(z) + \Omega[Z_+l_+(Z_+ + \Omega l - l_+) + z_-l_-(z_- + \Omega l - l_-)] + \frac{1}{6}\Omega(1 - \Omega)(2 - \Omega)l^3. \quad (\text{C3d})$$

Either of the equations in (C3a) can be replaced by the difference in the two:

$$Z_+^2 + z_-^2 + Z_+z_- + \Omega l \left( Z_+ + z_- + \frac{\Omega l}{2} \right) + \Omega \left[ l_+ \left( Z_+ - \frac{l_+}{2} \right) + l_- \left( z_- - \frac{l_-}{2} \right) \right] - 1 = 0. \quad (\text{C4})$$

Equation (C3a) are coupled equations for  $(Z_+, z_-)$  in terms of (dimensionless) contact zone ring thickness  $(l, l_{\pm})$ . Parameters  $(z_+, Z_-)$  then follow as

$$z_+ = Z_+ - l_+, \quad Z_- = z_- - l_-. \quad (\text{C5})$$

Because (C4) is quadratic, it is not difficult to rewrite (C3a) as uncoupled sixth-order equations for  $Z_+$  and  $z_-$ . For small deformation, however, (23b) implies that the ring is “thin”, with mean radius  $r_0$ . That is,  $l_{\pm} \ll 1$  and we assume that  $Z_+ \approx 1 + P_+(l_{\pm}) + O(l_{\pm}^2, l_+l_-)$  and  $z_- \approx -1 + P_-(l_{\pm}) + O(l_{\pm}^2, l_+l_-)$ . It can then be shown that (C3a) and (C5) give

$$Z_+ \approx 1 + \Omega \left( \frac{T}{2}l - l_+ \right), \quad z_- \approx -1 + \Omega \left( \frac{T}{2}l - l_- \right). \quad (\text{C6})$$

Parameters  $(l, l_{\pm})$  are not independent, so it is convenient to use  $(l, \bar{l})$ , where

$$l = l_+ + l_-, \quad \bar{l} = l_+ - l_-. \quad (\text{C7})$$

Then (C5) and (C6) give

$$l_{\pm} = \frac{1}{2}(l \pm \bar{l}), \quad (\text{C8a})$$

$$Z_+ \approx 1 + \frac{1}{2}\Omega(Tl - l - \bar{l}), \quad z_+ \approx 1 + \frac{1}{2}[\Omega Tl - (1 + \Omega)(l + \bar{l})], \quad (\text{C8b})$$

$$z_- \approx -1 + \frac{1}{2}\Omega(Tl - l + \bar{l}), \quad Z_- \approx -1 + \frac{1}{2}[\Omega Tl - (1 + \Omega)(l - \bar{l})]. \quad (\text{C8c})$$

In view of (25c) and (27c), Equation (C8) indicates that condition (29b) is satisfied when

$$\bar{l} = 0 \quad (|\psi| = \pi/2). \quad (\text{C9})$$

## Appendix D

Use of (28a) in the first equation in (35) gives the fifth-order equation for  $z_{\pm}^*$ :

$$\begin{aligned}
& (z_+^* - z_+)(Z_+ - z_+^*)(z_+^* - Z_-)(z_+^* - z_-)^2 \\
& + (z_+^* + \Omega T l)(z_+^* - z_-)(Z_+ - z_+^*)(z_+^* - z_+)[z_+^* + \Omega z_- - (1 + \Omega)Z_-] \\
& - (z_+^* - z_-)(z_+^* - Z_-)[z_+^* + \Omega Z_+ - (1 + \Omega)z_+] \\
& + T[\Omega(z_+ - Z_+)(z_+^* - z_-)(z_+^* - Z_-) + \Omega(Z_+ - z_-)(z_+^* - z_+)(z_+^* - Z_-)] \\
& + T[\Omega(z_- - Z_-)(z_+^* - z_+)(z_+^* - z_-) - (z_+^* - z_+)(z_+^* - z_-)(z_+^* - Z_-)] = 0. \quad (D1)
\end{aligned}$$

In the expectation that  $(l, \bar{l}) \ll 1$ , approximations (C8) and  $z_+^* \approx 1 + P^*(l, \bar{l})$  are employed in (D1), with result

$$z_+^* \approx 1 + \frac{\Omega}{2}(Tl - l - \bar{l}) - \frac{2(1 + \Omega) - T}{2 + (1 - \Omega)T} \frac{l + \bar{l}}{2}. \quad (D2a)$$

In similar fashion use of (28b) in (35) gives

$$z_-^* \approx -1 + \frac{\Omega}{2}(Tl - l + \bar{l}) - \frac{2(1 + \Omega) - T}{2 + (1 - \Omega)T} \frac{l - \bar{l}}{2}. \quad (D2b)$$

## References

- [Achenbach 1973] J. D. Achenbach, *Wave propagation in elastic solids*, North-Holland Series in Applied Mathematics and Mechanics **16**, Elsevier, Amsterdam, 1973.
- [Ahmadi et al. 1983] N. Ahmadi, L. M. Keer, and T. Mura, “Non-Hertzian contact stress analysis for an elastic half space: normal and sliding contact”, *Int. J. Solids Struct.* **19**:4 (1983), 357–373.
- [Barber 1992] J. R. Barber, *Elasticity*, Solid Mechanics and its Applications **12**, Kluwer, Dordrecht, 1992.
- [Bayer 1994] R. G. Bayer, *Mechanical wear prediction and prevention*, Mechanical Engineering **91**, Dekker, New York, 1994.
- [Blau 1996] P. J. Blau, *Friction science and technology*, Dekker, New York, 1996.
- [Boley and Weiner 1985] B. A. Boley and J. H. Weiner, *Theory of thermal stresses*, Krieger, Malabar, FL, 1985.
- [Brock 2009] L. M. Brock, “Basic problems of coupled thermoelasticity with thermal relaxation and pre-stress: aspects observed in exact and asymptotic solutions”, *J. Therm. Stresses* **32**:6-7 (2009), 593–622.
- [Brock 2012a] L. M. Brock, “Two cases of rapid contact on an elastic half-space: sliding ellipsoidal die, rolling sphere”, *J. Mech. Mater. Struct.* **7**:5 (2012), 469–483.
- [Brock 2012b] L. M. Brock, “Two cases of rapid contact on a coupled thermoelastic half-space: sliding ellipsoidal die, rolling sphere”, *J. Therm. Stresses* **35**:11 (2012), 1018–1036.
- [Brock 2014a] L. M. Brock, “Rapid sliding contact in three dimensional (*sic*) by an ellipsoidal die on transversely isotropic half-spaces with surfaces on different principal planes”, *J. Appl. Mech. (ASME)* **81**:3 (2014), Art. ID #031005.
- [Brock 2014b] L. M. Brock, “The rigid die on a half-space with thermal relaxation and convection: influence of sliding speed, die temperature, and geometry”, *J. Therm. Stresses* **37**:7 (2014), 832–851.
- [Brock and Georgiadis 2000] L. M. Brock and H. G. Georgiadis, “Sliding contact with friction of a thermoelastic solid at subsonic, transonic, and supersonic speeds”, *J. Therm. Stresses* **23**:7 (2000), 629–656.
- [Churilov 1978] V. A. Churilov, “Action of an elliptic stamp moving at a constant speed on an elastic half-space”, *Prikl. Mat. Mekh.* **42**:6 (1978), 1074–1079. In Russian; translated in *J. Appl. Math. Mech.* **42**:6 (1978), 1176–1182.
- [Craggs and Roberts 1967] J. W. Craggs and A. M. Roberts, “On the motion of a heavy cylinder over the surface of an elastic solid”, *J. Appl. Mech. (ASME)* **34**:1 (1967), 207–209.
- [Erdogan 1978] F. Erdogan, “Mixed boundary value problems in mechanics”, pp. 1–86 in *Mechanics today*, vol. 4, edited by S. Nemat-Nasser, Pergamon, New York, 1978.



- [Ignaczak and Ostoja-Starzewski 2010] J. Ignaczak and M. Ostoja-Starzewski, *Thermoelasticity with finite wave speeds*, Oxford University Press, 2010.
- [Jang 2000] Y.-H. Jang, “Transient thermoelastic contact problems for an elastic foundation”, *Int. J. Solids Struct.* **37**:14 (2000), 1997–2004.
- [Jang 2005] Y.-H. Jang, “Effects of thermal contact resistance on transient thermoelastic contacts for an elastic foundation”, *J. Appl. Mech. (ASME)* **72**:6 (2005), 972–977.
- [Lord and Shulman 1967] H. W. Lord and Y. Shulman, “A generalized dynamical theory of thermoelasticity”, *J. Mech. Phys. Solids* **15**:5 (1967), 299–309.
- [Rahman 1996] M. Rahman, “Hertz problem for a rigid punch moving across the surface of a semi-infinite elastic solid”, *Z. Angew. Math. Phys.* **47**:4 (1996), 601–615.
- [Sneddon 1972] I. N. Sneddon, *The use of integral transforms*, McGraw-Hill, New York, 1972.
- [Wang and Dhaliwal 1993] J. Wang and R. S. Dhaliwal, “Fundamental solutions of the generalized thermoelastic equations”, *J. Therm. Stresses* **16**:2 (1993), 135–161.

Received 15 Apr 2014. Accepted 7 Jul 2014.

LOUIS MILTON BROCK: [louis.brock@uky.edu](mailto:louis.brock@uky.edu)

Department of Mechanical Engineering, University of Kentucky, 265 RGAN, Lexington, KY 40506-0503, United States



# SUBMISSION GUIDELINES

## ORIGINALITY

Authors may submit manuscripts in PDF format online at the Submissions page. Submission of a manuscript acknowledges that the manuscript is original and has neither previously, nor simultaneously, in whole or in part, been submitted elsewhere. Information regarding the preparation of manuscripts is provided below. Correspondence by email is requested for convenience and speed. For further information, write to [contact@msp.org](mailto:contact@msp.org).

## LANGUAGE

Manuscripts must be in English. A brief abstract of about 150 words or less must be included. The abstract should be self-contained and not make any reference to the bibliography. Also required are keywords and subject classification for the article, and, for each author, postal address, affiliation (if appropriate), and email address if available. A home-page URL is optional.

## FORMAT

Authors can use their preferred manuscript-preparation software, including for example Microsoft Word or any variant of  $\text{T}_{\text{E}}\text{X}$ . The journal itself is produced in  $\text{L}^{\text{A}}\text{T}_{\text{E}}\text{X}$ , so accepted articles prepared using other software will be converted to  $\text{L}^{\text{A}}\text{T}_{\text{E}}\text{X}$  at production time. Authors wishing to prepare their document in  $\text{L}^{\text{A}}\text{T}_{\text{E}}\text{X}$  can follow the example file at [www.jomms.net](http://www.jomms.net) (but the use of other class files is acceptable). At submission time only a PDF file is required. After acceptance, authors must submit all source material (see especially Figures below).

## REFERENCES

Bibliographical references should be complete, including article titles and page ranges. All references in the bibliography should be cited in the text. The use of  $\text{BibT}_{\text{E}}\text{X}$  is preferred but not required. Tags will be converted to the house format (see a current issue for examples); however, for submission you may use the format of your choice. Links will be provided to all literature with known web locations; authors can supply their own links in addition to those provided by the editorial process.

## FIGURES

Figures must be of publication quality. After acceptance, you will need to submit the original source files in vector format for all diagrams and graphs in your manuscript: vector EPS or vector PDF files are the most useful. (EPS stands for Encapsulated PostScript.)

Most drawing and graphing packages—Mathematica, Adobe Illustrator, Corel Draw, MATLAB, etc.—allow the user to save files in one of these formats. Make sure that what you’re saving is vector graphics and not a bitmap. If you need help, please write to [graphics@msp.org](mailto:graphics@msp.org) with as many details as you can about how your graphics were generated.

Please also include the original data for any plots. This is particularly important if you are unable to save Excel-generated plots in vector format. Saving them as bitmaps is not useful; please send the Excel (.xls) spreadsheets instead. Bundle your figure files into a single archive (using zip, tar, rar or other format of your choice) and upload on the link you been given at acceptance time.

Each figure should be captioned and numbered so that it can float. Small figures occupying no more than three lines of vertical space can be kept in the text (“the curve looks like this:”). It is acceptable to submit a manuscript with all figures at the end, if their placement is specified in the text by means of comments such as “Place Figure 1 here”. The same considerations apply to tables.

## WHITE SPACE

Forced line breaks or page breaks should not be inserted in the document. There is no point in your trying to optimize line and page breaks in the original manuscript. The manuscript will be reformatted to use the journal’s preferred fonts and layout.

## PROOFS

Page proofs will be made available to authors (or to the designated corresponding author) at a Web site in PDF format. Failure to acknowledge the receipt of proofs or to return corrections within the requested deadline may cause publication to be postponed.

<b>B-splines collocation eigenanalysis of 2D acoustic problems</b> CHRISTOPHER G. PROVATIDIS	259
<b>Multi-region Trefftz collocation grains (MTCGs) for modeling piezoelectric composite and porous materials in direct and inverse problems</b> PETER L. BISHAY, ABDULLAH ALOTAIBI and SATYA N. ATLURI	287
<b>Analytical solution for ductile and FRC plates on elastic ground loaded on a small circular area</b> ENRICO RADI and PIETRO DI MAIDA	313
<b>Solution of a receding contact problem using an analytical method and a finite element method</b> ERDAL ÖNER, MURAT YAYLACI and AHMET BIRINCI	333
<b>Sliding of a cup-shaped die on a half-space: influence of thermal relaxation, convection and die temperature</b> LOUIS MILTON BROCK	347